

RAUL RAMMULA

Atomic layer deposition of HfO_2 –
nucleation, growth and structure
development of thin films



TARTU UNIVERSITY PRESS

The study was carried out at the Institute of Physics, University of Tartu.

The dissertation was admitted on May 20, 2011 in partial fulfillment of the requirements for the degree of Doctor of Philosophy in Physics (Applied Physics), and allowed for defense by the Council of the Institute of Physics, University of Tartu.

Supervisors: Prof. Jaan Aarik, Institute of Physics, University of Tartu, Tartu, Estonia.

Prof. Väino Sammelselg, Institute of Chemistry and Institute of Physics, University of Tartu, Tartu, Estonia.

Opponents: Prof. Juris Purans, Dr. hab., Institute of Solid State Physics, University of Latvia, Riga, Latvia.

Prof. Marek Godlewski, Dr. hab., Institute of Physics, Polish Academy of Sciences, Warsaw, Poland.

Defence: August 25, 2011, University of Tartu, Estonia.

ISSN 1406–0647

ISBN 978–9949–19–779–8 (trükis)

ISBN 978–9949–19–780–4 (PDF)

Autoriõigus Raul Rammula, 2011

Tartu Ülikooli Kirjastus

www.tyk.ee

Tellimus nr 373

TABLE OF CONTENTS

LIST OF ORIGINAL PUBLICATIONS	7
LIST OF ABBREVIATIONS AND SYMBOLS	9
1. INTRODUCTION.....	11
2. BACKGROUND AND OBJECTIVES	13
2.1. Technological use of HfO ₂	13
2.1.1. Integrated circuits and CMOS scaling.....	13
2.1.2. DRAM and nonvolatile memory capacitor structures	16
2.1.3. Challenges for high-k preparation and integration	18
2.1.4. HfO ₂ as a high-n material	21
2.1.5. Other applications of HfO ₂	22
2.2. Atomic layer deposition.....	22
2.2.1. Principles of atomic layer deposition.....	22
2.2.2. Growth per cycle in ALD.....	24
2.3. ALD of HfO ₂	29
2.3.1. Nucleation and interfacial layers.....	31
2.3.2. Structure of HfO ₂	33
2.3.3. Topography	34
2.4. Research objectives	35
3. EXPERIMENTAL METHODS	36
3.1. Film growth	36
3.2. Quartz crystal microbalance studies	36
3.3. Film characterization	38
3.3.1. Structure studies.....	38
3.3.2. Film thickness and composition measurements.....	42
3.3.3. X-ray photoelectron spectroscopy	44
3.3.4. Atomic force microscopy.....	46
4. RESULTS AND DISCUSSION.....	47
4.1. Nucleation.....	47
4.2. Growth rate	51
4.2.1. Influence of substrate temperature and carrier gas flow on growth rate.....	51
4.2.2. Influence of film thickness on growth rate	54
4.3. Phase composition and structure development	55
4.3.1. Influence of substrate material on structure of films	55
4.3.2. Influence of film thickness and growth temperature on phase composition and texture development	57
4.4. Topography	61
4.4.1. Nucleation uniformity and surface roughness of HfO ₂ thin films	61

4.4.2. Influence of crystallization processes on surface roughness ..	64
4.4.3. Influence of growth temperature and carrier gas flow rate on surface roughness	66
4.5. Optical properties of HfO ₂	69
5. SUMMARY AND CONCLUSIONS	73
SUMMARY IN ESTONIAN	
Hafniumdioksiidi aatomkihtsadestamine – nukleatsioon, kasv ja struktuuri muutused kiledes	75
ACKNOWLEDGEMENTS	76
REFERENCES	77
PUBLICATIONS	89
CURRICULUM VITAE	143

LIST OF ORIGINAL PUBLICATIONS

- I. J. Aarik, A. Aidla, A. Kikas, T. Käämbre, **R. Rammula**, P. Ritslaid, T. Uustare, V. Sammelseg, Effect of precursors on nucleation in atomic layer deposition of HfO₂, Appl. Surf. Sci., 230 (2004) 292–300.
- II. V. Sammelseg, **R. Rammula**, J. Aarik, A. Kikas, K. Kooser, T. Käämbre, XPS and AFM investigation of hafnium dioxide thin films prepared by atomic layer deposition on silicon, J. Electron Spec. Rel. Phen., 156–158 (2007) 150–154.
- III. **R. Rammula**, J. Aarik, H. Mändar, V. Sammelseg, Atomic layer deposition of HfO₂: Effect of structure development on growth rate, morphology and optical properties of thin films, Appl. Surf. Sci., 257 (2010) 1043–1052.
- IV. J. Aarik, A. Aidla, A. Kasikov, H. Mändar, **R. Rammula**, V. Sammelseg, Influence of carrier gas pressure and flow rate on atomic layer deposition of HfO₂ and ZrO₂ thin films, Appl. Surf. Sci., 252 (2006) 5723–5734.
- V. V. M. Lulla, J. Asari, J. Aarik, K. Kukli, **R. Rammula**, U. Tapper, E. Kauppinen, V. Sammelseg. Electron Probe Microanalysis of HfO₂ Thin Films on Conductive and Insulating Substrates, Microchim. Acta, 155 (2006) 195–198

AUTHOR'S CONTRIBUTION

Publication I The author has done part of the experimental work (spectrophotometry, QCM, XPS and AFM) and participated in analysis of results and writing the paper.

Publication II The author has done the most significant part of the experimental work (XPS and AFM) and participated in analysis of results and writing the paper.

Publication III The author has done most of the experiments (XRR, GIXRD, spectrophotometry and AFM), taken part in analysis of results and written the article.

Publication IV The author has done significant part of the experimental work (QCM, spectrophotometry and AFM) and participated in analysis of results and writing the paper.

Publication V The author has participated in preparation of samples, ex-situ thickness measurements, data analysis and discussions.

ARTICLES NOT INCLUDED IN THESIS:

- I. Kikas, J. Aarik, V. Kisand, K. Kooser, T. Käämbre, H. Mändar, T. Uustare, **R. Rammula**, V. Sammelselg, I. Martinson. Effect of phase composition on X-ray absorption spectra of ZrO₂ thin films, *J. Electron Spec. Rel. Phen.*, 156–158 (2007) 303–306.
- II. Tarre, J. Aarik, H. Mändar, A. Niilisk, R. Pärna, **R. Rammula**, T. Uustare, A. Rosental, V. Sammelselg. Atomic layer deposition of Cr₂O₃ thin films: Effect of crystallization on growth and properties, *Appl. Surf. Sci.*, 254 (2008) 5149–5156.
- III. Sammelselg, A. Tarre, J. Lu, J. Aarik, A. Niilisk, T. Uustare, I. Netšipailo, **R. Rammula**, R. Pärna, A. Rosental. Structural characterization of TiO₂–Cr₂O₃ nanolaminates grown by atomic layer deposition, *Surf. Coat. Technol.*, 204 (2010) 2015–2018.
- IV. Hudec, K. Hušeková, E. Dobročka, J. Aarik, **R. Rammula**, A. Kasikov, A. Tarre, A. Vincze, K. Fröhlich, Atomic layer deposition grown metal-insulator-metal capacitors with RuO₂ electrodes and Al-doped rutile TiO₂ dielectric layer, *J. Vac. Sci. Technol.*, B29 (2011) 01AC09 (1–5).

LIST OF ABBREVIATIONS AND SYMBOLS

AFM	Atomic Force Microscopy
ALCVD	Atomic Layer Chemical Vapor Deposition
ALD	Atomic Layer Deposition
ALE	Atomic Layer Epitaxy
AR	Antireflective
CB	Conduction Band
CET	Capacitance Equivalent Oxide Film Thickness
CMOS	Complementary Metal Oxide Semiconductor
Cp	Cyclopentadienyl, -C ₅ H ₅
CVD	Chemical Vapor Deposition
D_{fi}	Fixed interface charge density
D_{it}	Interface trap density
D_{ox}	Oxide trap density
D_m	Mobile ionic charge density
DRAM	Dynamic Random Access Memory
E_g	Band gap energy
EOT	Equivalent Oxide Film Thickness
EPMA	Electron Probe Microanalysis
Et	Ethyl, -C ₂ H ₅
FG	Floating Gate
FGMOSFET	Floating Gate Metal Oxide Semiconductor Field Effect Transistor
GB	Grain Boundary
GIXRD	Grazing Incidence X-ray Diffraction
GPC	Growth Per Cycle
HF	Hydrofluoric acid
HRTEM	High-Resolution Transmission Electron Microscopy
IC	Integrated Circuits
IC-AFM	Intermittent-Contact Atomic Force Microscopy
IL	Interface Layer
IMFP	Inelastic Mean Free Path
IR	Infrared
k	Relative dielectric constant, relative permittivity
LDT	Laser Damage Threshold
Me	Methyl, -CH ₃
MIM	Metal-Insulator-Metal
ML	Monolayer
MOSFET	Metal Oxide Semiconductor Field Effect Transistor
MuGFET	Multigate Field Effect Transistor
n	Refractive index
NVM	Nonvolatile Memory
p	Pressure

PE-ALD	Plasma-enhanced ALD
PDA	Post-Deposition Annealing
PE	Photoelectron
p_w	Partial pressure of water vapor
QCM	Quartz Crystal Microbalance
RHEED	Reflection High Energy Electron Diffraction
RMS	Root Mean Square
RTO	Rapid Thermal Oxidation
SCE	Short Channel Effect
SE	Substrate Enhanced
SI	Substrate Inhibited
SOI	Silicon On Insulator
TFEL	Thin Film Electroluminescence
T_G	Growth temperature
t_{ox}	Oxide film thickness
T_S	Source temperature
UV	Ultraviolet
v	Linear flow rate of carrier gas
XPS	X-ray Photoelectron Spectroscopy
XRD	X-ray Diffraction
XRF	X-ray Fluorescence
XRR	X-ray Reflection
Δm_0	Mass increment per ALD cycle

I. INTRODUCTION

Thin oxide films as well as their complex layered structures can be used in numerous applications – e.g. in micro- and nanoelectronics as conductive, semi-conductive or insulating media, in optics and optoelectronics as reflective and antireflective (AR) coatings or light emitting layers, in (micro-) mechanical devices as wear or corrosive resistant coatings, in resistive gas sensors as gas-sensing layers and in catalysts as functional surface coatings.

Due to the wide application range of thin films, different materials and their deposition methods are consistently studied to optimize film properties for certain applications. In some cases, fabrication method or process optimization has a minor effect on the final performance of a thin film. However, exact control of material deposition has crucial impact in the field of micro- and nanoelectronics where in many cases the effective medium is only few nanometers thick. Up till now planar substrates have mainly been used in integrated circuits (IC) but due to the high packing density of modern microelectronic elements, three-dimensional architectures and substrates are under extensive investigation [1–6]. Hence, besides precise thickness control and uniform composition of thin films, deposition methods must fulfill tight requirements for conformal coating of non-planar substrates. From the latter prospective, high-vacuum methods are somewhat disadvantageous as precursor transport to the substrate proceeds linear route, allowing only planar substrates to be covered uniformly. Contrarily, flow-type chemical vapor deposition (CVD) processes performed at markedly higher pressures are more favored as, under these conditions, precursors are able to travel into deep trenches and behind the edges. This results in formation of conformal layers, especially in the case of layer-by-layer growth mode, i.e. in the case of atomic layer deposition (ALD) formerly also known as atomic layer epitaxy (ALE) [7,8]. Atomic layer deposition is a special modification of thin-film deposition using distinctive advantages of sequential cyclic supply of the precursors to a substrate surface. At first the method was applied to prepare polycrystalline and amorphous films for large scale thin film electroluminescence (TFEL) displays [9]. The present interest in the method is mainly focused on the deposition of high permittivity (high- k) dielectrics for complementary metal–oxide–semiconductor (CMOS) logic devices and memory capacitors.

High permittivity dielectrics are extensively studied because conventional SiO_2 , which is used in metal–oxide–semiconductor field effect transistors (MOSFET) as a gate dielectric, has reached its application limits determined by tunneling current that increase to unacceptably high levels with the further reduction of the dielectric thickness required for development of new generations of IC [10,11]. Obviously, using of a high- k material instead of low- k SiO_2 ($k = 3.9$) enables application of physically thicker oxide layers with lower leakage current to obtain given capacitance of a memory capacitor or gate stack of MOSFET. Furthermore, performance of these devices could be improved

through enhanced capacitance, which is directly proportional to the dielectric constant. The best candidates for high- k materials are III or IV group metal oxides, silicates or oxynitrides in the form of single layers or laminated structures [10,11]. Still the biggest leap towards integration of high- k dielectrics into modern CMOS logic has been made by taking into use Hf-based materials [12,13].

As a thin film is formed through self-limited surface reactions in ALD, film quality and properties may largely depend on precursors used [8]. For instance, in ALD of oxide films, not only the metal precursor but also the oxygen precursor has great importance [14–16]. Besides that, surface activation and regeneration after each ALD cycle must be sufficient to achieve steady state, stable and well-controlled layer-by-layer film growth [8]. This requirement might, however, not be fulfilled due to the insufficient energy (temperature) or incorrect surface activation (low density of reactive sites) [8]. Therefore understanding the mechanisms of surface reactions, initial stage of growth, structure and morphology development, etc. has a great importance since many technologically important film properties, e.g. permittivity, bandgap (E_g), refractive index (n), etc., are influenced by the mentioned parameters.

In this thesis, ALD processes were studied in connection of highly important HfO₂ high- k material. Initial stage of growth and film structure evolution together with morphology formation was under investigation.

2. BACKGROUND AND OBJECTIVES

Robertson [10], Wilk [11], Iwai [17], Wong [18] and Thompson [19] have written thorough reviews of different aspects connected with IC downscaling and future challenges of IC-s. Therefore in this chapter, only a short review on application of high- k dielectrics, particularly HfO_2 , will be given. Nevertheless, all major factors needed to understand the importance and difficulties related to high- k dielectrics will be outlined. Although HfO_2 has gained much interest as a high- k material, it can also be exploited in various other applications that will be shortly described as well.

Similarly, Ritala and Leskelä [8], Puurunen [20], George [21] and Kim [22] have written extensive reviews on different aspects of ALD. Puurunen [20] has concentrated on different ALD growth modes as well as on precursors, while George [21] and Kim [22] have provided a more general description of the actual state of the ALD research and the future prospects. In this chapter, ALD processes are described concentrating on explanation of most important parameters. As inorganic precursor combinations like $\text{HfCl}_4\text{-H}_2\text{O}$, $\text{HfI}_4\text{-H}_2\text{O}$ and $\text{HfI}_4\text{-O}_2$ are used to deposit HfO_2 films in this work, the alternative metalorganic precursor combinations are only mentioned. The latter precursor family covers tens of compounds. Thus, detailed description of corresponding processes is a demanding task [20,23,24] that exceeds the limits of this thesis.

2.1 Technological use of HfO_2

2.1.1 Integrated circuits and CMOS scaling

Since invention of integrated circuits [25], enormous progress in terms of the device performance and functionality has been made. Nevertheless, so far the dominating architecture of the metal-oxide field effect transistor (MOSFET), a key component in IC-s, has not been changed substantially although geometrical dimensions have been continually reduced [26] to improve the performance of electronic devices. Within the last 40 years this process can be well described by the notorious Moore's law [27]. However, as soon as the node size was reduced below 100 nm and, correspondingly, SiO_2 gate oxide thicknesses $t_{ox} < 2\text{nm}$ were used in the gate stacks, major issues related to the ultrathin gate oxide were identified. The problems realized included direct tunneling [28,29], oxide reliability [28], polysilicon depletion [30–32], short channel effects (SCE) [33], etc. At 90 nm node size, technology of alternative Si/Ge source/drain was introduced to achieve uniaxial strain in the channel through lattice mismatch. This improvement was mainly connected with carrier mobility while the leakage current issue remained still unsolved. The subsequent decrease of the oxide thickness exponentially increased tunneling current ($\sim 10\text{ A/cm}^2$ at 1V bias with $t_{ox} = 1.5\text{ nm}$) [17], affecting severely performance and power consumption of devices [10,11]. As silicon dioxide

provides a high-quality i.e. low defect density (interface trap density $D_{it} \sim 10^{10} \text{ cm}^{-2} \text{ eV}^{-1}$, oxide trap density $D_{ox} \sim 10^{11} \text{ cm}^{-2}$) electrical contact with silicon [18], further attempts to reduce tunneling leakage were based on modification of SiO_2 . Solutions like heavily nitrided SiO_2 (SiO_xN_y with $k = 3.9$ – 7.9 , $E_g = 5.9$ – 9) or pure Si_3N_4 ($k = 7.9$, $E_g = 5.3$) provided higher dielectric constant than conventional dielectric (Table 1) and, thus, allowed certain reduction of the gate leakage ($\sim 1 \text{ A/cm}^2$ at 1 V bias with $t_{ox} = 1.5 \text{ nm}$) [17].

The benefit of high- k materials comes from higher permittivity that allows application of physically thicker films and, thus, achievement of lower leakage currents at the same value of the gate stack capacity:

$$C_{ox} = \frac{k\epsilon_0 A}{t_{ox}}. \quad (1)$$

In Eq.1, k is the relative permittivity of the gate oxide, ϵ_0 is the absolute permittivity of the free space (vacuum), A is the area of gate electrode and t_{ox} is the gate oxide thickness. This equation is also used to determine of equivalent oxide thickness (EOT):

$$EOT = \frac{k_{\text{SiO}_2}}{k_{\text{high-k}}} * t_{\text{high-k}} \Rightarrow EOT = \frac{3.9}{k_{\text{high-k}}} * t_{\text{high-k}}. \quad (2)$$

Equation 2 represents the theoretical thickness of SiO_2 film that must be used to achieve the same capacitance that is obtainable with the high- k dielectric material. Another parameter, a capacitance equivalent oxide thickness (CET), is used when oxide thickness is determined only from the accumulation capacitance.

Through the efforts described above, the usage of nitrided silicon (-oxide) based dielectrics extended to the 65 nm generation node size electronics. Downside, however, was lower quality of Si/dielectric interface ($D_{it} \sim 10^{11}$ – $10^{12} \text{ cm}^{-2} \text{ eV}^{-1}$) [83] and more complicated manufacturability as both, the dielectric film thickness and nitrogen incorporation into the dielectric film, had to be very precisely controlled. In addition, nitrogen penetration through oxide and accumulation at Si/dielectric interface during the post-deposition annealing [84] was a reason for the recession of device performance. Moreover, the oxide thickness had strong influence on the interface quality and, as a result, severe degradation of the interfacial layer occurred at EOT values below 1 nm [85]. Accordingly, scaling limit of Si_3N_4 has been reported to be at EOT of 0.65–1.13 nm [86]. Therefore materials with dielectric constant higher than 10 were needed for further reduction of EOT.

Table 1. Properties of SiO₂ and possible binary *high-k* dielectrics. All data have been taken from experimental studies. Scattering of the results comes from the different preparation and characterization methods used in reported studies.

Material	Dielectric constant, k	Band gap, E_g (eV)	References	Crystal structure
SiO ₂	3.9	9.0	[34]	Amorphous
Al ₂ O ₃	10	–	[35]	Amorphous
	–	6.6	[36]	
	–	7.2	[36,37]	α -phase
	9	8.7	[37]	γ -phase
Y ₂ O ₃	13–17	–	[38]	Amorphous
	–	4.99	[39]	
	20	–	[40]	Monoclinic
	–	5.28	[39]	
	15	–	[41]	Cubic
	–	5.38–5.75	[39,41]	
Ta ₂ O ₅	25	–	[42,43]	Amorphous
	–	5.28	[44]	
	55–65	–	[42,43]	Hexagonal δ -phase
	26–52	–	[41,43]	Orthorombic β -phase
	–	4.2–4.5	[41,45]	
TiO ₂	21–28	–	[46,47]	Amorphous
	–	3.4	[48]	
	75–160	–	[46,49–55]	Rutile
	–	3.0–3.16	[48,56,57]	
	33–37	–	[47,51,52]	Anatase
	–	3.2–3.35	[48,57]	
HfO ₂	16–26	–	[58–60]	Amorphous
	–	5.7–5.9	[61–65]	
	29–30	–	[66]	Tetragonal
	–	5.7	[67]	
	22–25	–	[68]	Monoclinic
	–	5.3–5.86	[62,64,69–71]	
	26–50	–	[72,73]	Cubic
	–	6.0	[73,74]	
ZrO ₂	18	–	[75]	Amorphous
	–	4.7–5.5	[61,63,65,76,77]	
	32–38	–	[78,79]	Tetragonal
	–	5.2–5.5	[76,80]	
	17–18	–	[81]	Monoclinic
	–	5.16–5.28	[80,81]	
	32	–	[82]	Cubic
–	5.8	[74]		

In the 45 nm node technology, the leakage current ($\sim 10^{-3}$ A/cm² at 1V bias) issue was solved with the insertion of Hf-based high- k materials as gate dielectrics [12]. Another important innovation in this node generation was connected with replacement of doped poly-Si gate electrode with a metal electrode. Gate depletion and other possible instability concerns were main driving forces to find electrodes such as TiN, TiAlN, TaN and NiSi, etc. having appropriate work function in contact with high- k dielectrics [87,88,89]. For the node generations of 32 nm and beyond, the reduction of EOT in conjunction with enhanced carrier transport as well as new device architectures are key points for the down-scaling. For mobility enhancement, silicon-on-insulator (SOI) technology [33,90,91], that displaces channel region compared to the conventional device structure, has been studied. In SOI systems, easier insulation can be provided while diminished drain and source junction areas reduce the parasitic capacitance. Via decreased doping concentration in channel region, improved mobility can be achieved [92]. SOI technology also allowed developing new device concepts like double gate [33,93], surrounding gate [33,94] as well as 3D schemes like FinFET [33,87], multigate field effect transistor (MuGFET) [87,95]. For the further advancement of FET-based devices, several high-mobility materials in the channel region, such as Ge, III–V compounds, carbon nanotubes [96,97], nanowires [98–101] and graphene [102,103] have been considered. At present time, Ge seems to be most feasible as it is already used and can be easily integrated into existing CMOS processing flow [104]. Certainly, strain control along with substrate orientation effects in terms of mobility enhancement is considered [32,33,105].

2.1.2. DRAM and nonvolatile memory capacitor structures

Another area of HfO₂ usage, which is closely related to IC, covers the development of dynamic random access memories (DRAM). A dynamic random access memory cell consists of a capacitor and access transistor to charge the capacitor (Figure 1). The same kind of scaling trends and capacitance improvement as in IC-s concern the development of DRAM-s [3]. Similarly the memory cell charge storage can be improved either by decreasing the dielectric thickness, increasing the dielectric permittivity and/or application of three-dimensional structures. Therefore, similar or even more crucial EOT demands are considered as in CMOS.

In modern DRAM-s, two basic three dimensional concepts are used to increase the capacitance of a memory cell – a trench (Figure 1 (a)) and stacked (Figure 1 (b)) capacitors. In the case of stacked capacitors (Figure 1 (b)), lower thermal budget of annealing processes ($\sim 650^\circ\text{C}$) allows easier implementation for existing CMOS technologies as well as accepting dielectrics with somewhat lower thermal stability because capacitor structures can be prepared after the transistors are formed.

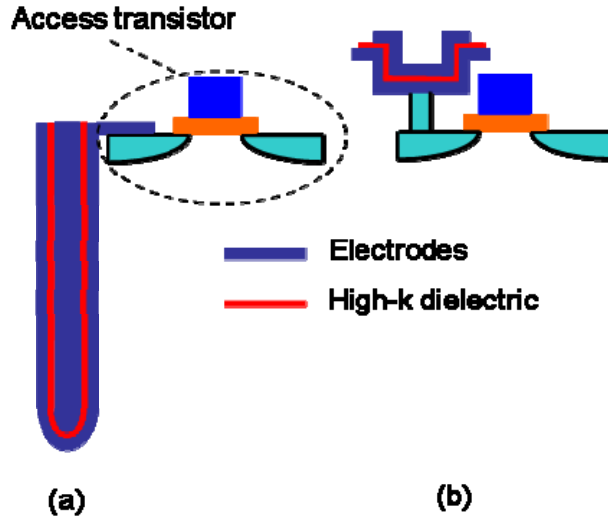


Figure 1. Three-dimensional (a) trench and (b) stacked capacitor schemes for DRAM.

In the trench version (Figure 1 (a)), higher density of cells can be achieved, although higher thermal budget ($>1000^{\circ}\text{C}$) and overall complexity of the fabrication process sets restricted demands for dielectric precipitability and thermal stability. Likely, every next generation uses trenches with higher aspect ratio setting additional requirements for the dielectric preparation. This is highly demanding task to provide necessary structural and thickness conformality in those 3D structures. By now, a properly chosen ALD process seems to be the acceptable solution for further progress in the case of this device architecture [106–110].

In a metal-insulator-metal (MIM) structure of a modern DRAM capacitor, band gap and work function requirements for the dielectric are not as strict as for gate oxides because sufficient barrier against electron injection can be still obtained when high work function metal electrodes are used [111]. Therefore electrodes like Ru, RuO_2 , SrRuO_3 , Pt, Ir etc. have been studied [112–120]. Simultaneously, ultrahigh- k perovskites like SrTiO_3 ($k \sim 300$) are also studied as being ultimate long term solution [121–123].

Possible applications of HfO_2 thin films cover also nonvolatile memory (NVM) applications in which each memory cell resembles a gate stack of a standard MOSFET (Figure 2). The basic operating principle behind the NVM devices is the ability to charge/discharge the gate insulator of the MOSFET while the charge is retained in these devices when the external power is removed. Storage can be realized in two ways. The first one is based on the storage of charge on a floating gate (FG) that is a conducting or semi conducting layer completely surrounded by a dielectric layer (Figure 2 (a)). As FG is electrically isolated, electrons can be trapped and, under normal

conditions, will stay there for a long time (retention time ~ 10 years with discharge of $\sim 0.2\text{--}0.5\text{V/decade}$) therefore floating gate MOSFET (FGMOSFET) is considered also as the basic building block of the flash memory [123–125]. In the second case the charge is stored in discrete trapping centers of an appropriate dielectric layer (Figure 2 (b)). In this concept memory effect can be achieved because of trapping of charge either by the defects of a dielectric layer (Figure 3) or by segregated (metallic)nanocrystals [127–129]. Nevertheless, in both cases the polarizability should retain several voltages wide hysteresis (memory window) to provide necessary write, erase and read steps of the device.

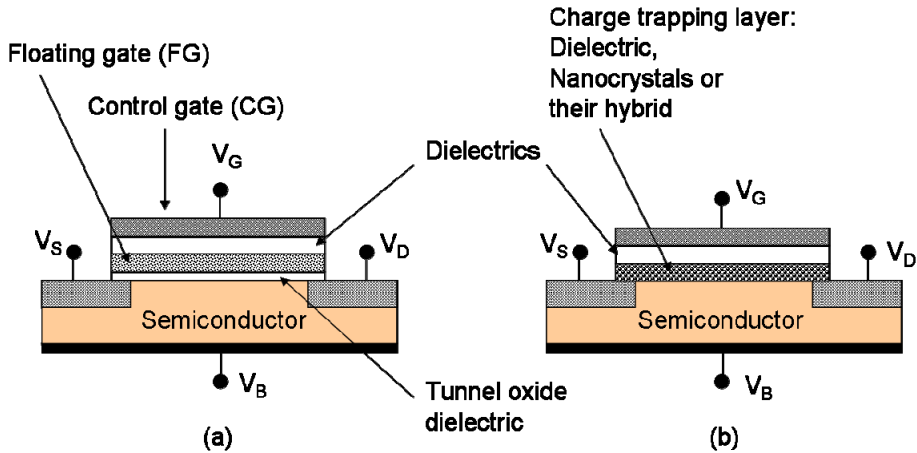


Figure 2. Schematics of (a) floating gate and (b) charge trapping nonvolatile memory device.

2.1.3. Challenges for high- k preparation and integration

Although first high- k studies reach back to the early 1980s [11] successful implementation of Hf-based dielectrics into devices has been done about 20 years later [12,13]. Notably, high- k integration into a CMOS manufacturing process flow has not been a straightforward task. While SiO_2 could be grown by thermal oxidation of silicon substrate, high- k materials needed different approach. With strict EOT demands, the deposition techniques suitable for this application should allow thickness and uniformity control at the nanometer-level on complex 3D structures. Therefore layer-by-layer growth like ALD has major advantage. Besides, proper dielectric material choice to provide necessary electrical properties is demanding task as many oxides noted in Table 1 have their pros and cons. In general, the key guidelines for selecting high- k dielectrics can be listed as follows;

- permittivity and band gap,
- thermodynamic stability,
- film structure and morphology,
- interface quality,
- process compatibility.

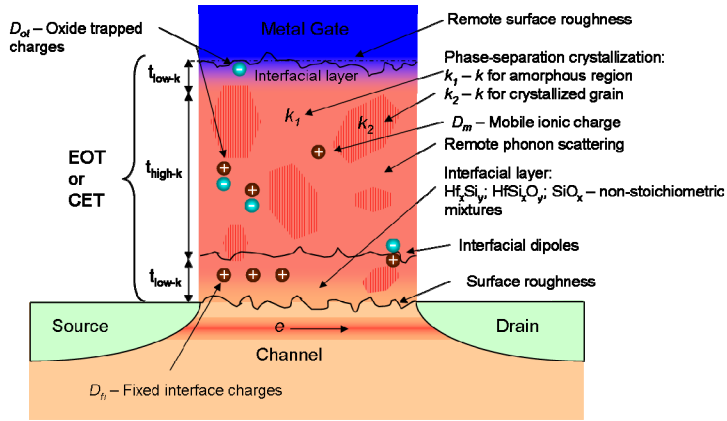


Figure 3. Possible defects, charge traps and interfaces associated with high- k MOS stack.

Permittivity and band gap: For long-term solutions, considerably higher permittivity compared with that of SiO_2 in conjunction with sufficient band gap is needed. It has been observed, however, that the dielectric constant decreases with the increase of the band gap [10,126,130]. In addition, k and E_g values can be largely varied by changing the crystal structure of the thin film (Table 1). Therefore all these characteristics should be optimized jointly. To reduce the leakage current, the conduction band (CB) offset should be preferably more than 1.0 eV [10]. Even though Al_2O_3 offered acceptable CB offset value, it was soon detached from the list of long-term solutions because of only minor improvement in permittivity (Table 1). HfO_2 and ZrO_2 provide well-balanced permittivity, E_g (Table 1) and CB offset properties in contact with silicon, especially if cubic or tetragonal crystal phase can be achieved.

Thermodynamic stability: According to the CMOS processing recipes, the high- k material should be stable at temperatures up to 1000°C. In that sense Al_2O_3 proved to be thermally stable [131–133] and a good diffusion barrier [134,135] forming abrupt interface with silicon [137]. Oppositely, TiO_2 and Ta_2O_5 are unstable in direct contact with silicon forming defective interfacial layers [138–140]. Similarly, under high-temperature thermal treatment, HfO_2 and ZrO_2 form interfacial layers on silicon surface. Although the former oxide

shows relatively high thermal stability [141,142], high temperature processing of HfO₂-based MOS structures may result in inter-diffusion that leads to the formation of low-*k* region near the metal gate (Figure 3) as well [153,154]. As these low-*k* regions reduce the effective dielectric permittivity of the system (see Figure 3 and Eq. 3), it is essential to choose a material that is stable enough to allow at least proper control of the IL formation during the growth process or post-deposition annealing. Another option is to deposit a barrier layer on silicon and/or a cap layer on the dielectric to suppress the interface layer formation. In both cases, the total EOT is increased and effective permittivity values reduced because of these additional (usually low-*k*) regions (Figure 3):

$$EOT = EOT_{high-k} + \sum EOT_{low-k} . \quad (3)$$

Nevertheless, Al₂O₃ is actively used as an additional component of high-*k* mixtures [143,144] or laminate structures [145,146] together with HfO₂. Other additives such as Si and N are also used to increase temperature stability and control IL properties to meet acceptable leakage current and carrier mobility demands [147].

Film structure and morphology: It is desirable to select a material that predominantly occurs in an amorphous phase because polycrystalline dielectrics contain grain boundaries (GB) that are possible charge leakage paths. However, most of the metal oxides of choice form polycrystalline films. For instance HfO₂ deposited at low temperatures can initially be amorphous but crystallizes during post-deposition annealing at temperatures exceeding ~500°C [148–152]. It is possible to increase crystallization temperature by choosing appropriate composition and annealing time parameters. Optimal Al (HfAl_xO_y), Si (HfSi_xO_y) and N (HfSiO_xN_y or HfO_xN_y) incorporation can stabilize (semi)amorphous phase for temperatures close to 1000°C. However, permittivity in the mixtures containing Si and Al is lower than the permittivity of pure HfO₂. Besides, depending on the doping method, added atoms may induce oxide charge traps as well (Figure 3). The traps formed can cause occurrence of fixed interface charge, oxide mobile charge and oxide/dielectric trapped charge.

Interface quality: Proper optimization of the interface states is one of the most significant tasks as this would preserve the capacitance gain obtained by using a high-*k* material. Interface state density at Si/metal oxide interface is usually higher than that at Si/SiO₂ interface and hence considerable losses in the charge carrier mobility in silicon occur. However, with properly chosen processing parameters, mobility in structures with high-*k* films can be enhanced up to ≥90% of that in structures with SiO₂ dielectric [98]. The trapped charges change also the occupancy with gate bias. This is, in turn, detrimental for the device power consumption. For mobility enhancement, a well-known solution is to increase the interface oxide thickness, but this comes at the expense of

increasing EOT. In order to meet device performance requirements, it is essential to have sufficiently low EOT values, however. Therefore, a compromise between achieving low EOT and maintaining high mobility has to be made. In addition, the interface roughness has a certain influence to the mobility of the carriers as the rough interface causes an additional mobility loss due to carrier scattering. Thus, the interfaces must be as smooth as possible.

Process compatibility: It is necessary that any new materials and preparation methods could be incorporated into the existing process flow. In micro- and nanoelectronics where the film uniformity and thickness control are essential, techniques like ALD are more favored as reaction kinetics, precursor chemistry, surface damage, impurities etc. can be more easily optimized by properly chosen setup than in the case of other deposition methods.

According to Eq. 2 and Table 1, HfO₂ physical thickness (t_{ox}) required in the CMOS process flow and in memories obviously depends on the appropriate permittivity and EOT values. For instance, if EOT of 0.5 nm is needed, t_{ox} should not exceed 6.4 nm for cubic and 3 nm for monoclinic film. Within such thickness range, all the above mentioned criterias for the dielectric must be fulfilled.

2.1.4. HfO₂ as a high- n material

Besides being an efficient high- k material, HfO₂ can be used as a high- n material in optical and optoelectronic devices. For HfO₂ films, refractive index values of 2.02–2.17 at $\lambda = 550$ nm have been reported dependently on the growth methods and deposition process parameters used and material structure obtained [155,156]. Furthermore, a wide transparency range (of about 0.22–12 μ m) extending from ultraviolet (UV) to far infrared (IR) and high laser damage threshold (LDT) have increased the interest to adapt HfO₂ as a low-loss material [156–159]. Typical applications include antireflective coatings of UV laser components and/or dielectric mirror designs where hafnia is the high-index component combined with low-index SiO₂ layers [160–162]. HfO₂ has been used also in AR multilayer coatings for night vision devices [163]. In addition, application of HfO₂ as a host material of Er-activated waveguides has been considered [164].

Either in AR coating or mirror design, exact film thickness and proper refractive index value is needed to provide conditions for destructive or constructive interference. This is achieved by choosing optimized refractive index profile for the whole stack. For instance, when light reflects from a higher- n medium ($n_1 > n_0$) reflected waves experience a 180° phase shift (half a wavelength), whereas no phase shift occur when reflecting from a medium with lower refractive index ($n_2 < n_1$). The simplest AR structure consists of single layer of material with the thickness of $t_{ox} = \lambda/(4n_1)$ and refractive index profile

$n_0 < n_1 < n_2$, where λ is the center wavelength, n_0 is the refractive index of the propagation medium, n_1 is the refractive index of the coating, and n_2 is the substrate refractive index. Ideally, the reflection can be completely eliminated when the thin film is a quarter wave thick and the refractive index is equal to the square root of the indices of the material on either side i.e. $n_1 = \sqrt{n_0 n_2}$. Such single layer AR coatings can reduce surface reflectivity for a particular wavelength range. Thus, more sophisticated multilayer structures are often applied for broadband solutions. In this case, high-index (n_H) and low-index (n_L) layers are alternately stacked to minimize the index change at the first and last boundary. Opositely, in dielectric mirror design, n_H and n_L periodic structure is used to maintain in phase reflection cumulative at every second interface of the layer structure. In this way, light transmission through the periodic structure gets smaller, whereas the high reflective region can be increased via refractive index contrast ($\Delta n = n_H - n_L$) of the layers. Although these mirrors can provide very high reflectance, preparation of high-reflective HfO₂/SiO₂ coatings with a reflectance of only 97–99% has been reported for the 250–350 nm spectral range. This is mainly because of optical losses that cause major issues [160,162]. The optical losses are related to the absorption and/or light scattering due to the structural inhomogeneity, density fluctuation, surface roughness, impurities, etc [165]. Therefore besides precise thickness and refractive index profile control, more complex optimization of film parameters is needed to prepare high-quality dielectric mirrors.

2.1.5. Other applications of HfO₂

Due to hardness and thermal stability of HfO₂, this material can be used in wear resistant coatings of micromechanical devices [166]. In this connection, it is worth mentioning that tetragonal HfO₂ formed at high pressure has been described as a material that is potentially harder than diamond [167,168]. HfO₂ has also been applied as a gas sensor material with reasonable sensitivity to CO [169] and C₃H₈ (propane) [170]. A possible solution for solar cell systems with selective HfO_x/Mo/HfO₂ multilayer coatings has been reported too [171].

2.2. Atomic layer deposition

2.2.1. Principles of atomic layer deposition

ALD is a deposition technique that was patented in Finland in 1970s by Suntola and Antson [172]. The method relies on alternating saturative surface reactions where each precursor is pulsed into the reaction chamber sequentially and the pulses are separated by purging periods (Figure 4). Due to saturation of surface reactions at properly chosen growth conditions, the film growth is thereby self-limiting. This offers accurate and simple thickness control at nanometer level,

and excellent conformality over large areas, complex shapes of surfaces and on 3D nanostructures [8,20,173,174].

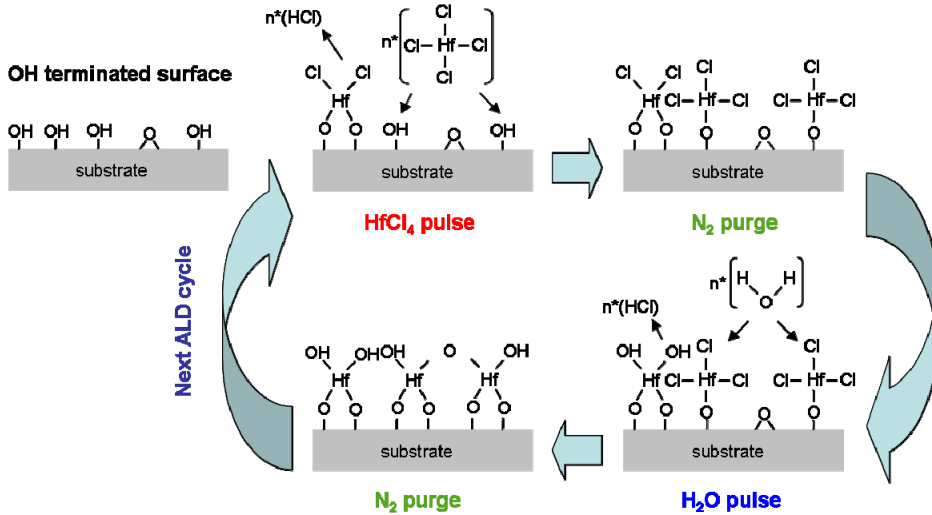


Figure 4. Simplified mechanisms for one ALD cycle of HfO₂ in HfCl₄-H₂O process.

In the simplest version of ALD, the growth process consists of four steps forming one complete ALD cycle. For instance, HfO₂ can be grown from HfCl₄ and H₂O using cycles that start by introducing volatile HfCl₄ precursor into the heated reaction chamber where the precursor molecules can react preferably with OH-terminated surface [8,20,175,176]. During the exchange reaction chemical bond between precursor and substrate is established while HCl as a by-product is simultaneously released. This reaction continues until the surface gets saturated with chemisorbed HfCl_x ($x < 4$) species. Due to the HfCl₄ immunity towards the formed Cl-terminated surface, the reaction stops when the surface is covered by chlorine. After the metal precursor pulse the excess of precursor and by-products are purged with an inert carrier gas. The purge period has a great importance to avoid gas-phase reactions (CVD-like growth) with the upcoming second precursor. After purging, H₂O injected into the reaction chamber reacts with chemisorbed HfCl_x. HCl is again released and the Cl-terminated surface is transformed into OH- and O-terminated one. In this way, part of HfO₂ monolayer is deposited and the surface sites susceptible for HfCl₄ chemisorption in the next ALD cycle are recovered. Within the second purge, the reaction byproducts and excess water vapor are removed with inert carrier gas. After the complete cycle the surface is covered by the same functional groups as in the beginning of the ALD cycle and, thus, is ready for the cycle repetition.

The nature of the exchange reaction mechanism in ALD process is highly determined by the substrate and film surface, precursor combination and growth

temperature (T_G). For instance, it has been proven that silicon surface may be hydrogen terminated (Si-H) or covered by terminal (Si-OH), bridged (Si-OH-Si) and/or geminal (Si-2(OH)) OH-sites and/or bridged oxygen (Si-O-Si) sites whereas their concentrations depend on the reactor temperature (Figure 5) and time elapsed from the set-up of a certain temperature level [177–179].

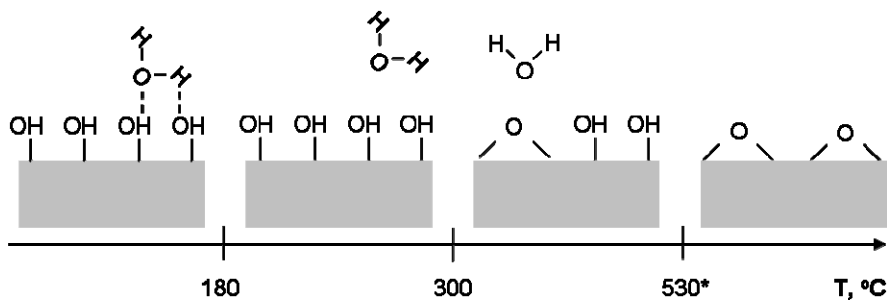
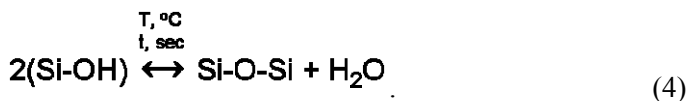


Figure 5. Possible water desorption and hydroxyl group transformation upon the increase of T_G . Dehydroxylation at elevated temperatures is influenced by T_G as well as substrate orientation.

Reactions through ligand exchange occur most likely through OH-terminated surface when at least one of the precursor ligands combines with the H-atom and the formed by-product desorbs from the surface. Dissociation may occur while oxygen bridges are available, i.e. at elevated temperatures. In that case, an oxygen bridge is splitted into two surface sites that are terminated with the precursor ligands after adsorption. Likewise, these bridges can vice versa initiate formation of terminal OH-sites during H_2O pulse [176] (Eq. 4):



However, due to the insufficient energy, precursor molecule may adsorb through association. In that case, no ligand release occurs. Instead, a coordinative bond is formed. For $\text{HfCl}_4\text{-H}_2\text{O}$ process, the ligand exchange has been accepted to be the main reaction mechanism [175,180–182,185].

2.2.2 Growth per cycle in ALD

In order to characterize the growth rate in an ALD process, the film growth per cycle (GPC) is usually determined. This parameter shows how thick layer is formed in every cycle. In a self-saturative ALD process, all available surface

sites must be occupied, i.e. pulses must be long enough to provide steady-state saturation of the GPC versus pulse length dependence (Figure 6). Depending on the precursor reactivity and transport efficiency, the pulse duration needed to achieve saturation can strongly vary. Slow saturation (Figure 6 dotted line), if this is due to low partial pressure of a precursor, improves precursor utilization as longer dosing allows all reactant species to be chemisorbed. However, longer pulses needed to obtain saturation extend overall deposition time. Fast saturation (Figure 6 dashed line) on the other hand reduces deposition time but may lead to the precursor waste, when massive overdosing is applied. Therefore characterization of the self-saturation mode is needed not only for understanding the behavior of different precursor combinations, but for increasing the precursor utilization and reactor efficiency as well.

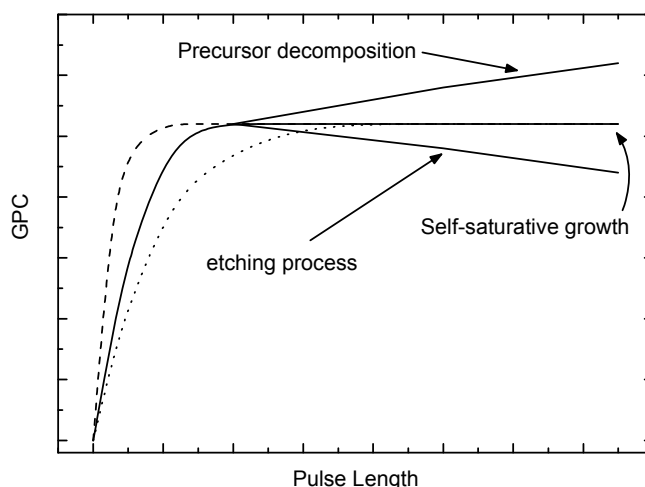


Figure 6. Growth per cycle as a function of precursor pulse time in different ALD processes.

Theoretically, ALD may proceed by one atomic layer per cycle. In practice, however, only a fraction of a monolayer (ML) is deposited due to the limited number of the surface sites and steric hindrance. In the latter case, the ligands of a chemisorbed molecule cover more adsorption sites than needed for adsorption of one molecule. Thus, other incoming reactant molecules are unable to link to the surface and are flushed away. This would suggest that small ligand size can result in higher GPC. However, it has been shown that monolayer deposition is impossible even for precursors as HfCl_4 [176,186–188]. Therefore low GPC is obtained, although the concentration of adsorption sites available on the surface would allow obtaining of markedly higher value. Besides latter effect, GPC is greatly affected by the precursor self-decomposition and gas-phase reactions

that lead to CVD-like process (Figure 6). On the other hand, at the continuous precursor flow etching processes (Figure 6) can cause GPC decrease [8,189]. In general, GPC of any ALD process is a function of the growth temperature, substrate and film material and precursor combination.

Effect of growth temperature

Growth temperature affects GPC through the temperature-dependent concentration of active surface sites and sizes of surface species adsorbed on these sites. In addition, modification of the reaction mechanisms might also be temperature-dependent (Figure 7). At too low temperatures, increased GPC is obtained, when reactants or formed by-products condense on the growing film. Opposite effect is observed, when insufficient activation energy limits the rate of the surface reactions. Introduction of additional energy can enhance reactivity at low-temperatures. For instance, more reactive oxidant like O_3 instead of H_2O [15,16] or supplementary plasma source have been employed to improve deposition and properties of material at lower T_G values [190]. Besides, plasma-enhanced ALD (PE-ALD) can effectively be used to reduce the surface roughness of metal films [191].

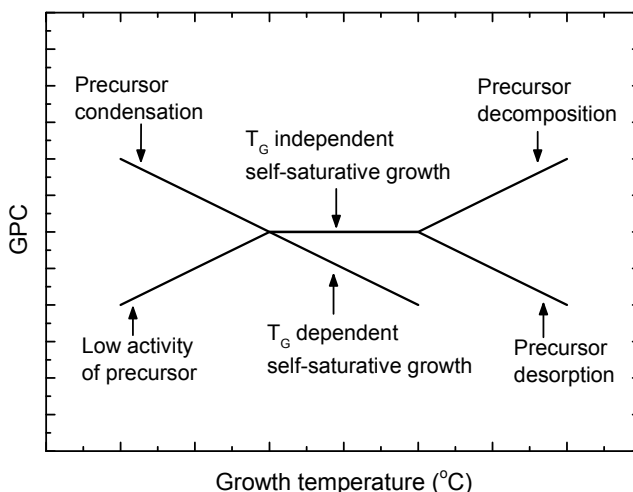


Figure 7. Possible dependencies of GPC on growth temperature.

Relatively strong dependence of GPC on T_G can be observed also at too high temperatures. Enhanced GPC can be obtained because of decomposition of precursors and/or chemisorbed complexes (Figure 6), while inhibited GPC is induced by desorption of chemisorbed species. In between these two temperature regions, the ALD process should proceed in the self-limiting mode. In this

temperature range, GPC is controlled by the steric hindrance of adsorption or by density of the reactive surface sites. In both cases, dependence of GPC on T_G can be observed (Figure 7).

Effect of substrate

In the ideal case, constant amount of a film material is deposited in every ALD cycle, allowing film growth with a rate that is independent of the number of cycles applied (Figure 8). In this case, the same number of reactive sites should contribute to the deposition process in the initial deposition stage and during the following growth while the reaction mechanism should also remain unchanged. In real processes, however, different reactivity of the substrate surface compared to that of the film surface may cause deviations from linear growth (Figure 8).

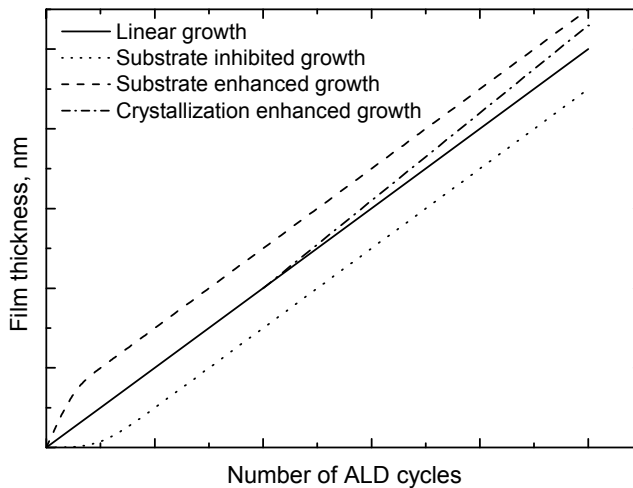


Figure 8. Dependence of film thickness on the number of ALD cycles: linear growth, substrate-inhibited, substrate-enhanced and crystallization-enhanced growth.

There are two basic phenomena that account these fluctuations: substrate enhanced (SE) and substrate inhibited (SI) growth [20]. In the case of SE growth, the starting surface exhibits more reactive sites than the growing film. Therefore GPC is higher in the beginning of the ALD process. More common situation is SI growth, where the GPC is gradually increased with the number of cycles until the steady-state growth rate is obtained. The substrate-inhibited growth is most likely connected with the nucleation problems on the substrate. After complete covering of the substrate with the film material the further growth continues with a constant rate. In addition to the above mentioned

phenomena, enhanced GPC can occur during the film growth, when crystallization related processes contribute to the growth (Figure 8 dash-dot line). For example, the growth rate can increase with the film thickness, when initial growth of the amorphous phase is turned into crystal growth, whereas the growth of the crystalline phase proceeds with a higher rate than the growth of the amorphous phase does.

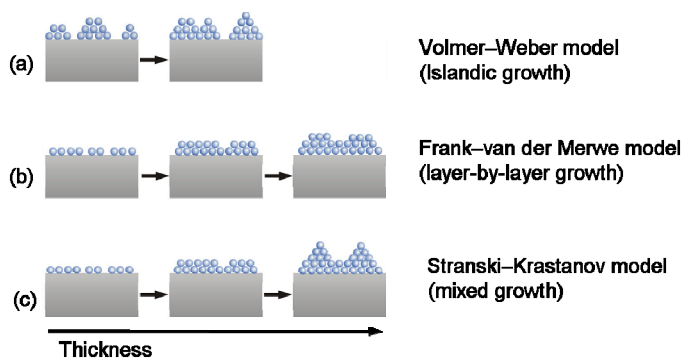


Figure 9. Simplified schemes of the different growth modes in ALD: (a) island growth, (b) two-dimensional layer-by-layer growth and (c) mixed growth.

SE and SI growth can be related to the growth mode that defines how the deposited material is arranged during the ALD process (Figure 9). The growth mode may influence the film properties like surface roughness, density, defectiveness etc. In principle, three general growth modes can be distinguished [192,193]. Island-like growth (Figure 9 (a)) is obtained when one of the precursors chemisorbs preferentially on the already grown material instead of starting surface i.e. reactivity towards substrate is lower than that towards the surface of growing film. In such growth mode, the initial growth stage is a highly non-uniform until the islands coalesce [195]. Two-dimensional growth (Figure 9 (b)) can be achieved when the precursors preferentially chemisorb on the lowest unfilled states covering all available sites. The last growth mode is a mix of the first two (Figure 9 (c)). In the initial growth stage, the material deposits with equal probability on both onto the starting surface and onto the already grown layer. Afterwards the initial 2D growth is switched to 3D growth due to the crystallization processes (or strain) in the growing film. Consequently, the dependence of the film thickness on the number of ALD cycles applied in the initial growth stage (Figure 8) implies how efficiently the substrate is covered, and is the first indication of possible growth mode.

Choice of precursors

Proper choice of precursors is the most important factor in terms of successful and optimized ALD process. Accordingly, suitable ALD reactants must fulfill certain requirements [8]. ALD precursors should be sufficiently volatile to ensure convenient and efficient transportation of those to the substrates in the gas phase. Besides gaseous precursors, liquid and solid precursors with reasonably high vapor pressure can be considered for application in ALD as well. The precursors should be highly reactive towards the chemisorbed species to achieve fast and complete saturation. Fast reaction completion contributes not only to the possible reduction of the ALD cycle duration but also to the purity of the film. Both the precursor and reactive surface species formed by this precursor have to be thermally stable to maintain the self-limiting growth mechanism. Otherwise, the precursor decomposition might lead to the CVD-type growth (Figure 6) and/or non-stoichiometry of the film material. Besides mentioned requirements, the chosen precursor combination and by-products should not etch the substrate and/or the growing film. In addition, the by-products formed should be inert and sufficiently volatile for easy removal. Metal precursor suitable for ALD can be divided into two basic classes, inorganic and metalorganic precursors [8]. The former class covers halide precursors such as HfCl_4 , HfI_4 , while the latter includes alkoxides like $(\text{Hf}[\text{OC}(\text{CH}_3)_2\text{CH}_2\text{OCH}_3]_4)$, alkylamides like ($\text{CH}_3 = \text{Me}$; $\text{C}_2\text{H}_5 = \text{Et}$; $\text{Hf}(\text{NEtMe})_4$, $\text{Hf}(\text{NEt})_4$, $\text{Hf}(\text{NMe})_4$), cyclopentadienyl like ($\text{Cp} = \text{C}_5\text{H}_5$; Cp_2HfMe_2) etc. [20,106,196,197] that all have widely been used for ALD of HfO_2 . Both precursor classes have their advantages and disadvantages. For instance, halides possess good thermal stability and high reactivity together with their small ligand size. Unfortunately, many halides have low vapor pressure i.e. reactor must allow heated precursor delivery system. There have also been concerns with residual chlorine impurities when HfCl_4 is used as a metal precursor. However, application of proper deposition techniques can reduce chlorine concentration in the dielectric to levels that are much more tolerable [180,198]. Liquid metalorganic precursors on the other hand exhibit higher vapor pressures. In some cases, reasonably high vapor pressure can be obtained already at room temperature. Unfortunately, metalorganic precursors are often applicable for ALD in a narrower T_G window compared with halide precursors [197,199].

2.3. ALD of HfO_2

Wide range of precursor combinations can be applied to deposit HfO_2 via ALD [20,197]. The first and most widely studied HfCl_4 - H_2O process [200,201] exhibits extremely wide ALD-window. The reported self-limiting growth can be obtained in the range of 150–940°C [175,202,203], whilst the growth rate first continuously decreases upon T_G increase and then remains constant in a T_G range of 600–940°C. For this process, however, different growth rate values

ranging from 0.05 to 0.17 nm at the same T_G [152,175,202–209] and varying e.g. from 0.06 to 0.09 nm even in the same type of reactors at 300°C [203,207] have been reported. This variation of the results might come from the difference in precursor doses [203,207,210,211] and/or deviation in carrier gas flow conditions that may lead to the overlapping of pulses. Nevertheless, the growth rate decrease in conjunction with T_G increase clearly correlates to the decreasing contribution of surface exchange reactions taking place [175] and low density of the favored OH-reaction sites at higher temperatures [177–179]. Latter effect is of great importance since ligand exchange has been proposed as the main reaction mechanism [175,180,181,182,185] for HfO₂ formation.

Low thermal activation of the precursor chemisorption at lower temperatures leads to highly disordered films [204] with unreasonably high impurity concentration. For instance, films deposited at 226°C in the HfCl₄-H₂O process contained 2.4±0.3 at% of residual chlorine and 5.1±0.5 at% of hydrogen, whereas with the increase of T_G to 400°C, the concentration of chlorine decreased down to 0.1 at% and the hydrogen concentration stabilized at a level of 0.2 at% [202]. Other precursor combination like HfI₄-H₂O offer slightly lower halide content at 300°C but the difference is not significant [206]. In the films deposited in the HfI₄-O₂ process, the concentration of residual iodine did not exceed 0.1 at% at $T_G \geq 500^\circ\text{C}$ [213,214]. However, for acceptable growth rate of about 0.11–0.12 nm, relatively high T_G (500–750°C) was needed. Halogen-free films with growth rate of about 0.09 nm can be achieved via alkylamides–water (e.g. Hf(NEtMe)₄-H₂O) but considerable impurity content of C and H (e.g. 0.3–0.6 at-% of C and 2–3 at-% of H at 250°C) have been reported [215]. Post-deposition annealing (800°C) slightly reduced contamination in the films but the impurity concentration still reached higher values than those corresponding to HfCl₄-H₂O process performed at 300°C [216]. Similarly, Ferrari et al [217] have applied high temperature ($\leq 1050^\circ\text{C}$) post-deposition annealing to the films grown using the HfCl₄-H₂O precursor combination. It was revealed that chloride is rather stable in the film and difficult to remove, while interface impurities can more easily be outdiffused. Likely, indiffusion of oxygen or water accelerated chlorine outdiffusion and initiated an interfacial layer growth. In the as-deposited films, the chlorine concentration is more pronounced in the regions that are closer to the substrate [218]. During the annealing process, the impurities may cause etching and void defect formation [219,220]. Thus, the initial film composition achieved in the as-deposited state influences the properties of annealed films too, making the studies of the as-grown films very important.

Lower concentration of chlorine impurities obtained at elevated temperatures [181,182] is an evidence of more complete hydrolysis reaction that might be related to lower stability of oxychloride-like surface species. In addition, increased H₂O dose and/or longer pulse can provide better initial crystallinity [210,211,212] and lower impurity content [180]. Accordingly, Delabie et al. [180] have determined about 10 times lower chlorine concentration in the films

deposited at 300°C when H₂O pulse was increased from 0.3 sec to 10 sec. Although the thickness of the interfacial layer did not depend on the H₂O pulse time, the D_{it} was slightly reduced. Another way is to replace oxygen precursor in the HfCl₄ process to more reactive O₃, which can reduce concentration of Cl residues in a film and improve dielectric properties [15,16]. However, ozone process produces thicker IL, which naturally causes higher CET values and therefore modest scaling possibilities when compared with conventional H₂O process [15,16].

2.3.1. Nucleation and interfacial layers

HfO₂ growth from HfCl₄ and H₂O can be initiated through the ligand exchange reactions while the effectiveness and uniformity of nucleation correlate to the density of favorable surface sites. Therefore different pretreatment techniques are applied either to retard or provoke nucleation. In the case of most optimal nucleation (Figure 8, linear dependence), the HfCl₄-H₂O precursor combination results in initiation of HfO₂ growth through Si-OH (silanol) surface sites [176,187,188,221–225]. Most commonly the silicon surface is pretreated by using hydrofluoric acid (HF) and deionized H₂O or by HF and deionized H₂O/O₃ solution. The surface layer obtained in this way has been referred to as wet oxide [187,188,223]. Oxygen bridges (Si-O-Si) are mainly generated by thermally grown silicon oxide formed by rapid thermal oxidation (RTO) in O₂ environment after etching the substrate in HF [188,223]. Hydrophobic (Si-H) sites are introduced simply by etching the native oxide in HF solution. In the latter case, H-terminated surface clearly inhibited nucleation [151,187,188, 221,222] and caused non-uniform island-like growth. On the H-terminated surface, the Hf atom density was about of 0.3–0.4 Hf/nm² after one HfCl₄-H₂O exchange reaction, i.e. after the first ALD cycle, while on fully hydroxylated wet oxide, the Hf atom density up to 3.9 Hf/nm² was achieved [223]. Accordingly about 5 cycles is needed to form a monolayer of HfO₂ on Si-OH surface, while more than 20 cycles must be applied on Si-H surface [222] at T_G of 300°C. Somewhat less significant impact of surface pretreatment has been observed when Hf(NEtMe)₄ (Tetrakis-EthylMethylAmino hafnium, TEMAH) [209,226–228] and Hf(N(Me)₂)₄ (Tetrakis(dimethylamino)hafnium, TDMAH) [229] were used as the metal precursors. Thus, reactivity of the latter precursors towards dehydroxylated surfaces is obviously higher than that of HfCl₄. In the TEMAH-based process, islandic-type growth has been observed during about 20 cycles ($t_{ox} \sim 1.2$ nm) while in corresponding chloride process, 50 cycles ($t_{ox} \sim 3$ nm) were needed to achieve film continuity on HF-last Si surface [209].

In the HfCl₄-H₂O based process, the Hf-atom density depends on the thickness and uniformity of wet oxide layer being highest at an oxide thickness of 1.2 nm [223]. The steric hindrance of the adsorbed -HfCl₃ (Figure 4) limit the Hf-atom density to 2.9 Hf/nm². However, if HfCl₄ reacts with two OH surface sites (-HfCl₂ is formed in the adsorbate layer), the Hf-atom density increases to

4.4 Hf/nm² [223]. It has been reported that the latter reactions are dominant at lower T_G [175]. In the first cycles, chemisorbed Hf is likely bonded to O atoms originated from OH surface sites as well as O atoms belonging to SiO₂ covering the Si substrate. Accordingly, adsorption of the Hf precursor follows competitive route between both bridging O atoms from the first HfO₂ layer and OH surface sites [105,223,230]. While complete HfO₂ has been formed, nucleation and growth proceeds via the Hf-OH surface sites allowing one to suggest different reactivity than on Si-OH sites. For uniform HfO₂ growth, density of Hf species remains, however, well below the steric hindrance limitation, possessing Hf-atom density value of about 1.2–1.5 Hf/nm² [223] and being clearly dependent on regeneration of favorable OH sites. The density of OH groups decreases with increasing T_G [175] because of easier dehydroxylation at elevated temperatures. Nevertheless, reactions over oxygen bridges insignificantly should contribute to the film growth at temperatures below 400°C [175].

In addition to the aforementioned, the crystallographic orientation of the substrate or growing film can determine how effectively OH sites are (re)generated [105,231]. Nyns et al. [105] have shown that oxidation is slower on Si (1 0 0) than on the corresponding Si(1 1 0) due to the lower number of surface atoms, which inherently are able to form OH-sites. In the case of HfO₂, the (−1 1 1) surface of the monoclinic phase retains higher coverage of OH sites than the (0 0 1) surface does at T_G values below 300°C [231]. However, above ~400°C the (−1 1 1) surface gets completely dehydroxylated. Meanwhile at elevated temperatures (0 0 1) surface sustain reasonable OH coverage and completely dehydroxylates above 530°C [231]. Notably the adsorption energy of H₂O is significantly higher on the (0 0 1) surface than on the (−1 1 1) surface.

Besides efficient nucleation, optimal HfO₂/Si interface formation is a key factor to reduce D_{it} and improve carrier mobility in silicon covered by the high- k gate stack. Many research groups have provided several routes of how the IL is formed either already during the film growth or after post-deposition annealing (Figure 10) [15,232–234].

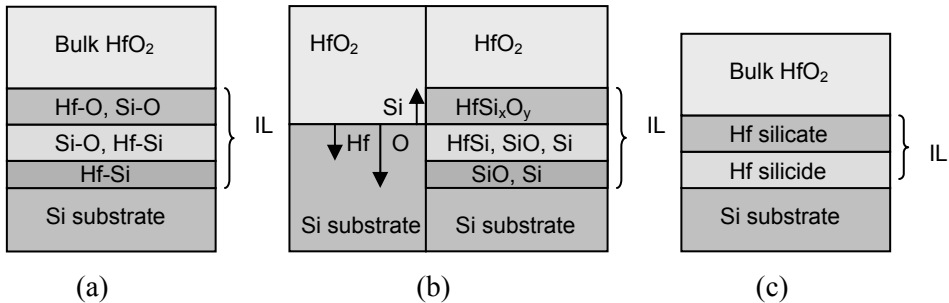


Figure 10. Possible HfO₂/Si interface formation routes through (a) mixed layer [233], (b) interdiffusion with different starting layer [232] and (c) over two step mixing reaction [234].

Nevertheless, IL formation and composition depends on the Hf, O and Si diffusion and their ability to be (re)combined before bulk HfO_2 is formed. Compared with other elements, oxygen diffuses more easily either due to its release from Si/SiO₂ or through grain boundaries present in polycrystalline HfO_2 [232,235,236]. In the latter case, oxygen can diffuse up to 10⁴ times faster than through bulk material [237]. The effect can be clearly seen when PDA processes are performed in the O₂ environment [236–240]. However, low concentration of O₂ or usage of O₃ at temperature below 800°C can provide more reliable control over the IL formation [236,238,241,242]. In the case of optimized ozone treatment, stronger Hf-O bonding together with low concentration of oxygen vacancies obtained can reduce leakage current by more than two orders of magnitude compared to that obtained in the case of the oxygen treatment [241]. Obviously, at temperatures above 800°C, regrowth of the interfacial layer and changes in film morphology appear. In the case of high vacuum treatment, oxidation to SiO_x like layer is efficiently retarded but above 800°C HfO_2 is transformed to HfSi_x [243,244]. Even more, in oxygen-deficient ambient, two step silicide/silicate like IL layer formation (Figure 10 (c)) [234] without the possibility to invoke SiO_x layer may take place during HfO_2 deposition. However, silicide-like IL layer is disadvantageous as Hf-Si_x bonds are confirmed to be metallic resulting effective channels for electron transport. These bonds can also reduce effective band gap and band offset with silicon [232].

2.3.2. Structure of HfO_2

At room temperature and atmospheric pressure, HfO_2 forms stable monoclinic crystal phase that transforms to tetragonal phase at about 1300 K and into cubic phase at about 2700 K [250,251]. Although in ALD processes, growth rate and structure of films depend on the growth temperature, precursors and substrates used, it has been proven that HfO_2 tends to form dominantly polycrystalline monoclinic phase [201,206; 212,214,252,253] with some preferential orientation (i.e. film texture) on silicon as well as silica substrate [202,254]. Besides T_G , reactor setup and precursor chemistry seem to influence the texture formation [206,255,256]. In the case of low thermal activation, certain film thickness is often needed to start crystallization. For instance, such behavior has been reported at 300°C where crystallization has become detectable after formation of ~ 5–30 nm thick amorphous HfO_2 film [175,205].

At T_G of 880–940°C, metastable cubic phase has been obtained in the surface layer of about 10 nm in thickness [254]. Formation of the latter phase highly depends on HfCl_4 and H_2O dose being most developed at higher HfCl_4 and low H_2O doses. Metastable cubic phase has also been obtained at 600°C in films with thicknesses up to 4 nm [257]. Furthermore, formation of orthorhombic or tetragonal phase has been reported at certain film thicknesses and temperatures as well [175,212]. Metastable high-temperature phases can be addi-

tionally stabilized at lower temperatures via incorporation of dopant atoms and/or controlling the dimensions of crystallites. For instance in ZrO_2 , which has similar properties and growth behavior as HfO_2 , tetragonal phase can be stabilized when particle size is less than 30 nm [258]. From technological point of view, cubic and tetragonal phases offer higher dielectric constant than corresponding monoclinic phase does (see Table 1). This inherently allows further EOT scaling. It has been shown that the stabilization of tetragonal HfO_2 by Si addition [260] and cubic HfO_2 by Y doping [261,262,263] is feasible. Furthermore, with proper deposition process and post-deposition annealing parameters, cubic HfO_2 can be stabilized without any additional dopants [73].

Due to possible optical applications, some studies have been focused on crystallization of HfO_2 on transparent quartz substrates [201,202]. Expectedly, changes in the film structure have influenced optical properties of the films, partially because of the corresponding changes in the surface roughness, partially because of variation of the refractive index and light scattering inside the films due to the polycrystalline nature of the films. As noted before, changes in the crystal structure and increasing surface roughness may also lead to a marked growth rate increase in ALD processes which has been reported for instance for TiO_2 [264,265], ZrO_2 [266] and Cr_2O_3 [267].

2.3.3. Topography

HfO_2 surface topography and surface roughness is highly determined by the initial nucleation and further structure evolution. Mitchell et al. [247] and Hausmann et al. [255] have clearly shown formation of separated conical grains at low T_G that may originate either already from the starting surface or from the growing film. In thicker films or at higher deposition temperatures, these grains coalesce and form polycrystalline layer. HRTEM studies of the films with thicknesses around 80–100 nm have shown lateral grain size decrease from 60 to 35 nm upon T_G increase from 225 to 450°C in the HfCl_4 - H_2O process [247]. In the case of about 100 nm thick HfO_2 films deposited from $\text{Cp}_2\text{Hf}(\text{CH}_3)_2$ and H_2O , surface RMS roughness have decreased from 4.3 to 2.9 nm when T_G was increased from 350 to 400°C [23]. Similar effect has been seen for the precursor combination $\text{Hf}[\text{N}(\text{CH}_3)(\text{C}_2\text{H}_5)]_4$ - H_2O . RMS roughness values of 7.9 and 3.9 nm have been measured for 132 and 170 nm thick films deposited at 200 and 300°C respectively [215]. Another work that has compared as-deposited films grown in different halide-based process at 300°C has reported RMS values of 2.3 nm and 1.8 nm for 62 and 54 nm thick films deposited from HfI_4 - H_2O and HfCl_4 - H_2O processes, respectively [206]. Replacement of H_2O with O_3 in HfCl_4 -based ALD process has resulted in more than 2 times smoother surfaces [15]. At deposition temperatures exceeding 450°C, columnar structure [247,253] is likely formed as crystallites grow preferably in thickness [202] rather than laterally [247] at these temperatures. It is obvious that structure formation and crystallite growth both influence the surface roughening. Due to

crystallization of initially amorphous films, post-deposition annealing has also enhanced film roughness [152,268]. Crystalline films are, on the other hand, more stable in PDA processes.

2.4. Research objectives

When the studies described in this thesis were initiated in 2003, some experimental and theoretical studies on the effects of substrate temperature on the composition, growth mechanism and structure of HfO_2 films grown by ALD had been published [175,176,182,203,254]. In this thesis, the effect of structure development on growth rate and related surface roughness evolution of the HfO_2 films was taken under systematic consideration. Due to the various applications of HfO_2 , including those in optical devices, transparent (quartz) substrates were supplemented to these studies. Initial nucleation [187,188] was of great importance as islandic growth severely degrades film properties, especially in terms of interface and defect state formation. Consequently, different substrate pretreatment was studied to obtain more uniform nucleation. As growth per cycle has very distinct temperature-dependent feature in the HfCl_4 - H_2O process [175,247], the initial stage of film growth was investigated at different temperatures. At higher temperatures, different ALD chemistries were used to study possible variations in structure and nucleation [I,II].

Effect of structure evolution on growth per cycle has a great importance when exact thickness and film properties are essential for certain application. Therefore relatively wide thickness range as well as customized metrology for accurate thickness measurements was applied to understand this effect and its influence on film properties [I,III–V].

Besides, influence of the reactor set-up on the growth rate and film structure was of particular interest. Latter study was initiated because of controversial results obtained from different research groups while dissimilar growth rates had been obtained in similar reactors [203,207,210,211]. For that reason, influence of the carrier gas pressure and flow rate on the growth rate and structure was carried out. This topic is described in paper [IV]

The effect of the reactor setup and corresponding structural changes on density, refractive index and light absorption of the film was essential task of the research. The measurements were important as these thin film parameters also influence electrical properties that were not directly characterized in this thesis. Selected film properties are closer discussed in papers [I,III,IV].

3. EXPERIMENTAL METHODS

3.1. Film growth

All films studied in this work were grown in a flow-type hot-wall ALD reactor [175,202]. For real-time (*in-situ*) growth monitoring experiments substrate holder was replaced with quartz crystal microbalance [175,269,270]. Usually growth experiments [I–III,V] were carried out at a pressure of 2 mbar in the growth zone. Pressures of up to 4.5 mbar and linear gas flow rates ranging from 0.7 to 7.6 m/s (determined at $T_G = 300^\circ\text{C}$) were used in some studies [IV]. Solid precursors were volatilized inside the reactor. Pulsing of the precursors was accomplished by changing the carrier gas flow direction through the precursor source. Depending on the precursor chemistry either vapor of distilled H_2O or O_2 (AGA 99.999 %) was used as an oxygen precursor. Oxygen precursors were introduced into the reactor from external reservoirs whereas the flow rates of these precursors were adjusted with a needle valve. Nitrogen (AGA 99,999 %) was used as a purging and carrier gas. Before deposition Si substrates were cleaned in HF and afterwards rinsed in deionized water, if not stated otherwise. Quartz substrates were ultrasonically cleaned in ethanol. All films described in this thesis were studied in “as-deposited” state i.e. no additional post-deposition treatment was made.

3.2. Quartz crystal microbalance studies

The quartz crystal microbalance (QCM) technique was introduced for characterization of ALD processes at elevated temperatures by Aarik et al [270]. The essence of quartz crystal microbalance (QCM) technique is based on piezoelectric properties of quartz crystal [271] that allow precise recording mass increase of the sensor through its resonant frequency variations:

$$\Delta f = -\frac{2f_0^2 \Delta m}{A\sqrt{\mu\rho}} = -C\Delta m. \quad (4)$$

In Eq. 4, Δf is the quartz crystal frequency change, f_0 is the resonant frequency of the unloaded quartz, Δm is the mass change, A is the surface area, μ is the shear modulus of the AT-cut quartz ($2.947 \cdot 10^{11} \text{ g cm}^{-1}\text{s}^{-2}$), ρ is the density of quartz (2.648 g cm^{-3}), and C is a crystal dependent parameter. Due to the difficulties of direct conversion of frequency to film thickness, raw data of frequency is often used [136]. Alternative route is to record period of quartz crystal oscillation instead of frequency [175,269,272]. Such experimental setup provides better sensor signal linearity and thereby more reliable results.

QCM signal fluctuation caused by the instabilities of the heaters is major concern at higher T_G [273]. Slow temperature drifts can be corrected by using QCM signal that was recorded before and after ALD process studied [274,275]. This allows baseline extrapolation to take into account these slow drifts. Fast temperature fluctuations caused by precursor pulsing, on the other hand, can not be determined and corrected reliably because they influence the QCM signal simultaneously with mass changes. To diminish the effect of these temperature fluctuations, optimum dose of precursors, well-balanced gas supply and carefully chosen temperature profile in the growth zone were used.

Considerable amount of film material was usually deposited before any QCM measurements in order to avoid influence of the silver electrodes of a quartz crystal on the results. The thickness of this buffer layer was usually about 5–10 nm [175]. Due to this buffer layer QCM studies presented in this thesis were not affected by possible initial growth limitations.

With QCM, the mass increase per growth cycle (Δm_0 in Figure 11) can be monitored. Furthermore, using the $\Delta m_0/\Delta m_1$ ratio, it is possible to estimate the ligand to metal ratio in the chemisorbed layer formed during metal precursor pulse. The latter ratio gives an estimation of how many ligands are released in each reaction step during the film formation. The shape of the QCM signal also provides valuable information on the adsorbate layer stability as well as on the precursor decomposition, inefficient precursor transportation, reactivity of precursors etc.

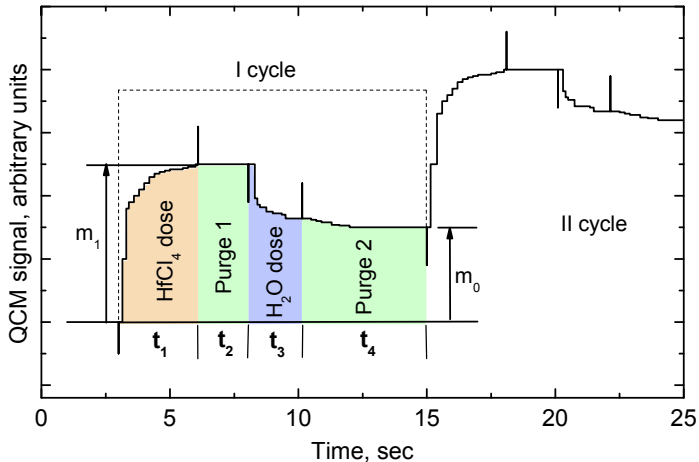


Figure 11. QCM signal recorded for HfCl₄-H₂O ALD process.

The measurement of Δm_0 enables one to determine surface self-saturation efficiency of new precursor combinations and/or to optimize reactor setup also in the cases when the effect of temperature fluctuations related to the precursor

pulses can not be excluded. In the studies described in the thesis, this approach was used to investigate the effect of carrier gas pressure and flow rate on ALD of HfO₂ (and ZrO₂) [IV]. In these QCM studies the duration of precursor pulses and purge times were varied to see, if and when the ALD process is self-limiting. Corresponding dependencies were recorded at different substrate temperatures, and carrier gas pressures and flow rates. In the QCM studies [IV], high frequency crystals with a resonant frequency of around 30 MHz were used to maintain acceptable sensor sensitivity and count resolution. With these crystals, sensitivity that was better than 0.1 monolayer was achieved.

3.3. Film characterization

3.3.1. Structure studies

X-ray diffraction

X-rays are used to study the internal (crystalline) structure of materials since their wavelength is in the range 0.05–0.25 nm which is of the same order of magnitude as the inter-atomic distances in solids. The X-ray diffraction (XRD) method that was explained already in 1912 by Max Laue [276] relies on the constructive interference of X-rays scattered from a crystal lattice (Figure 12). The condition for the constructive interference, i.e. for the strongest signal that can be recorded when the angle of the incident beam fulfils Bragg law, is:

$$m\lambda = 2d \sin \theta . \quad (5)$$

In Eq. 5, m is an integer number, λ is the wavelength of the incident beam, d is the distance between the crystalline planes i.e. interplanar distance, and θ is the angle between the incident beam and crystal surface.

Depending on the sample under investigation, two different scan modes can be applied (Figure 12). A symmetric or standard Bragg-Brentano ($\theta/2\theta$) scan is used to determine the crystal planes parallel to the sample surface (Figure 12(a)). In this measurement setup, the angle θ of the incoming beam with respect to the sample surface is varied, simultaneously keeping the detector at an angle of 2θ with respect to the incoming beam. The angle θ , at which a diffraction peak is observed, can then be inserted into Eq. 5 to give the interplanar distance. Besides the diffraction peak angle, the full width at half maximum (FWHM) of that peak contains information about the film structure. In the case of a perfect crystal, the FWHM is inversely proportional to the thickness of the crystalline layer while, in the case of polycrystalline films, FWHM allows determination of the mean crystallite size. Usually Bragg-Brentano mode is used for thick (poly-) crystalline films.

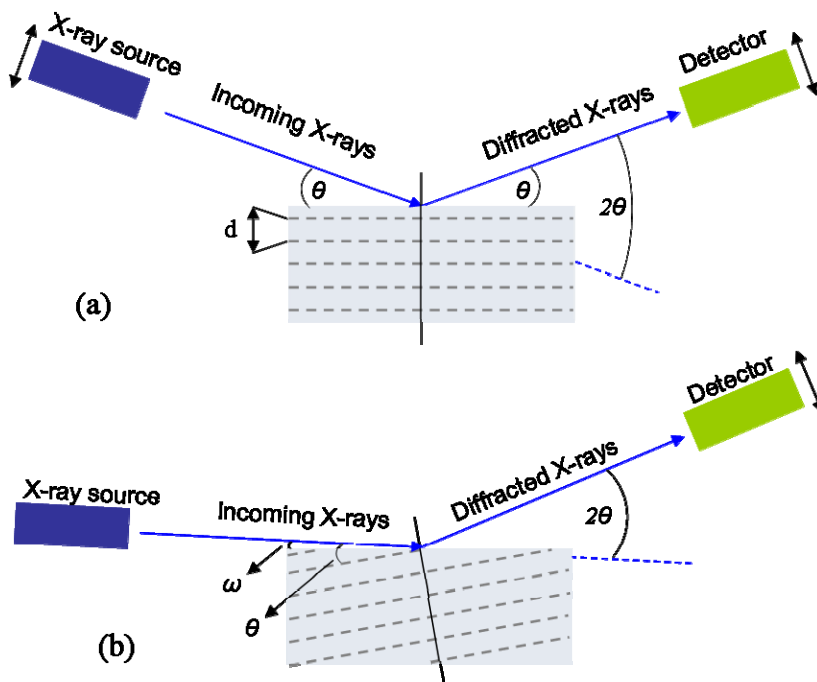


Figure 12. Schematic presentation of (a) symmetrical Bragg-Brentano $\theta-2\theta$ and (b) fixed grazing incidence angle X-ray diffraction scan.

In thinner films, particularly in those where crystallization is weak, i.e. in predominantly amorphous films with small amount of crystalline phases, fixed angle grazing incidence X-ray diffraction (GIXRD) should be used instead of standard XRD (Figure 12(b)). The benefit of the latter geometry relies on its enhanced surface sensitivity (Figure 13) as small angle of incidence (in our studies $\omega = 0.4-0.5^\circ$) drastically reduces penetration depth. Therefore, structure evolution with the film thickness increase can be easily studied even for the mainly amorphous regions as the substrate signal is dramatically reduced. In contrast to the Bragg-Brentano geometry, the lattice planes, which are not parallel to the sample surface, are analysed by GIXRD. Similarly to Bragg-Brentano geometry, the detector is placed at an angle of 2θ with respect to the incoming beam but the crystallographic plane contributing to signal has offset of $\theta - \omega$ compared to the film surface.

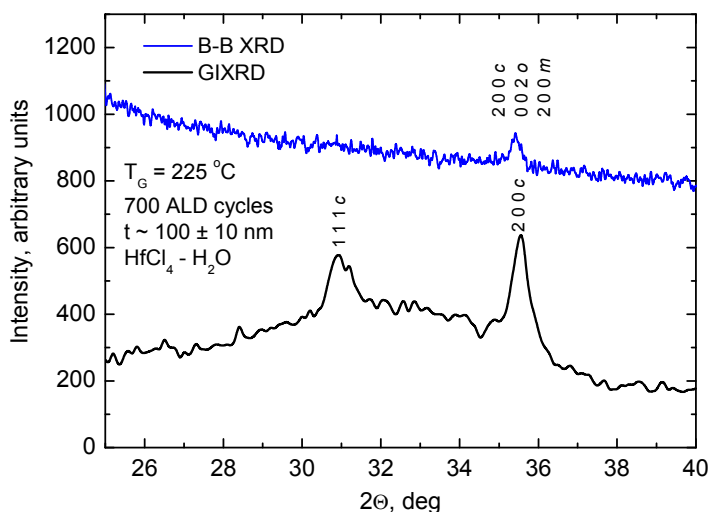


Figure 13. XRD signals of HfO₂ film recorded at different geometries. Reflections of cubic, monoclinic and orthorhombic phase are denoted by *c*, *m*, *o* after Miller indices.

In the study this thesis is based on, XRD analysis was used to detect the crystalline phases as well as sizes of crystallites in the films [III,IV]. The measurements were made by using both scanning methods to improve both the accuracy and sensitivity, because the films studied were of very different thickness and structure.

The equipment for Bragg-Brentano XRD analysis was based on a diffractometer DRON-1 (Nauchpribor, Russia) having a symmetrical coupled $\theta/2\theta$ step scanning system and a X-ray tube with CuK α ($\lambda = 0.15$ nm) radiation. For GIXRD and X-ray reflection (XRR) measurements, a reconstructed diffractometer URT-1 (Nauchpribor, Russia) was applied. All XRD, GIXRD and XRR data were analyzed by AXES software package [277]. The crystallite sizes were estimated by using Voigt decomposition method for fitting the diffraction peaks.

Reflection high energy electron diffraction

The reflection high energy electron diffraction (RHEED) method (Figure 14) is similar to the GIXRD because glancing incidence is constant and does not exceed few degrees [278]. The small incidence angle ensures that electrons penetrate only through a very thin surface layer (<10 nm) making this technique extremely surface sensitive.

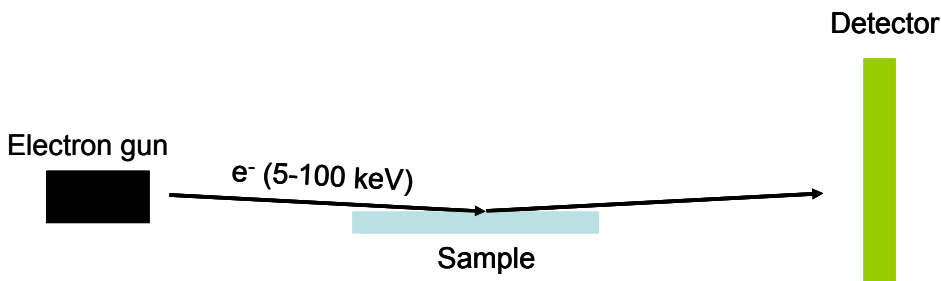


Figure 14. Simplified scheme of RHEED measurement setup.

Depending on the surface morphology, crystallite orientations and surface reconstruction, different types of RHEED patterns can be collected from the crystalline surface (Figure 15). Single crystal with atomically flat surface produces a set of sharp diffraction spots (Figure 15 (a)). However, when terraces decrease in size i.e. increase in density, the diffraction spots transform into streaks while the streak width is inversely proportional to the terrace size (Figure 15 (b)). In the case of single crystal film with rough surface, transmission pattern is produced i.e. electron beam penetrates through the crystallites and set of broad spots are generated (Figure 15 (c)). Polycrystalline or textured films produce a set of concentric circles or arcs (Figure 15 (d)).

The RHEED method is frequently used for in-situ monitoring of the film growth in high vacuum reactors [279]. In our studies, however, ex-situ measurements were carried out to characterize the surface structure of thin films [I].

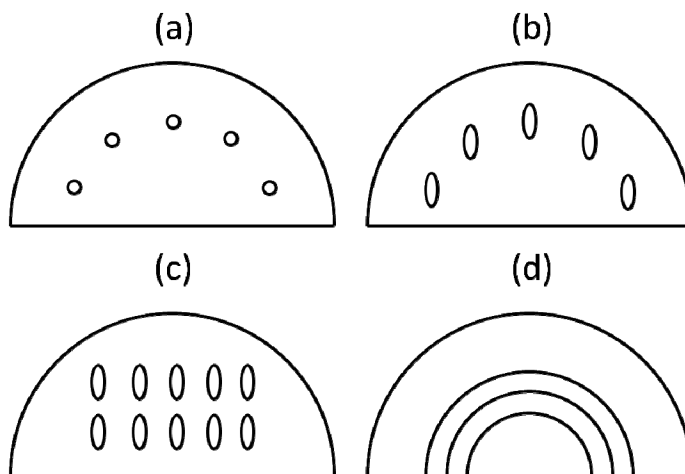


Figure 15. RHEED diffraction patterns of (a) single crystal film with atomically flat surface, (b) single crystal film with small terraces, (c) single crystal film with rough surface and (d) polycrystalline film.

RHEED patterns were recorded with an electron diffractometer EMR-100 (SEIMI, Ukraine). The energy and current of the primary beam were set to 75 keV and 20–30 μA respectively, while the impingement glancing angle was $\leq 10^\circ$. These measurement parameters enabled obtaining the structural information from a surface layer with a thickness of less than 5 nm.

3.3.2. Film thickness and composition measurements

For thickness and growth rate measurements, combination of different characterization methods was exploited because of the accuracy limitations [280–282] of the techniques in the wide thickness range used in this study [I–IV]. XRR was chosen because in addition to thickness, film density and roughness can be determined by this method. In XRR, the reflectance of the sample is measured as a function of the grazing incidence angle of X-rays. Due to interference effects of the radiation reflected from the film surface and that reflected from the film/substrate interface, oscillations depending on the film thickness occur in the reflectance curve. The X-ray beam undergoes total reflection from the film surface at incident angles lower than the critical angle for reflection. At angles higher than the critical angle, the incident beam penetrates into the film, and the intensity of the reflected X-rays decreases significantly. The density of the material can be determined on the basis of the critical angle value [283,284]. From the period of oscillations that are formed due to the X-ray interference, one can estimate the film thickness [283,284]. The surface roughness of the film can be determined from the decrease of the oscillation amplitude in the reflectivity curve (Figure 16). In the XRR curves of the films with high surface roughness, no oscillation can be observed and, thus, the thickness of these films can not be determined from the XRR data (Figure 16, blue line).

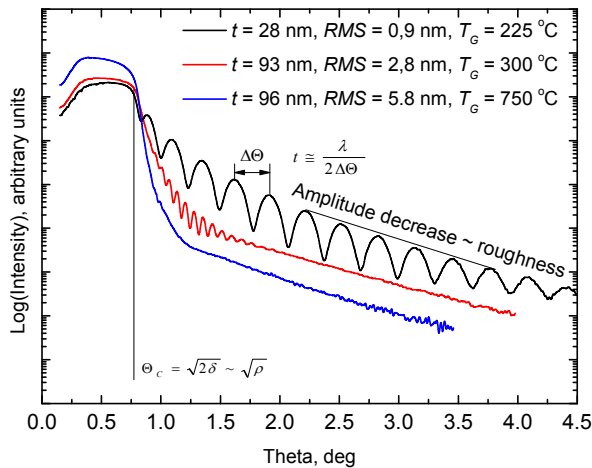


Figure 16. XRR curves of HfO₂ films with different thickness and surface roughness. RMS values are taken from AFM measurements.

The thicknesses of thicker films deposited on quartz substrates were calculated from optical transmission spectra, using envelope method for fitting oscillation curves and Swanepoel homogeneous single layer approximation [285]. These calculations yielded also the refractive index and extinction coefficient values that were under investigation in this work [I,III,IV]. The extinction coefficient values determined in this way depended on absorption as well as scattering of the light in the films. The uncertainty of thickness determination from optical measurements markedly increased with the decrease of the film thickness below 100–150 nm. In such thickness range, accurate fitting of the transmission spectra (Figure 17) turns out to be a complex task because of limited number of oscillations.

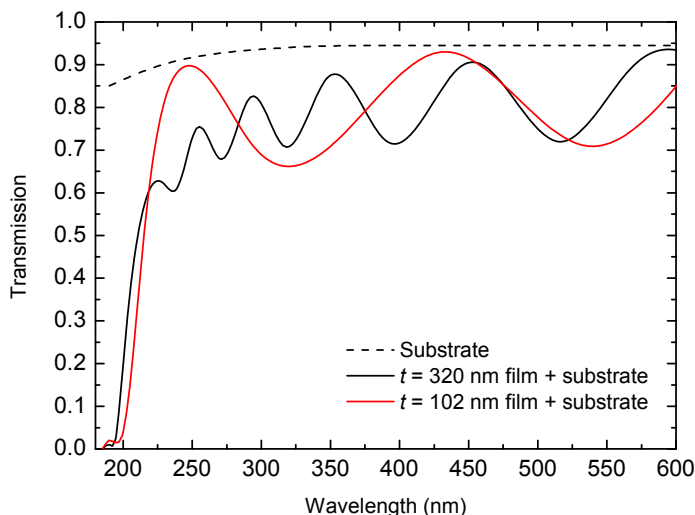


Figure 17. Optical transmission spectra of HfO₂ films with different thicknesses.

In order to overcome the limitations of the XRR and spectroscopic techniques, the films were also measured by X-ray fluorescence (XRF) method to determine relative mass thickness of the films [280]. The method gives accurate values of the mean film thickness independently of surface roughness. However, reference samples with known density are desirable in XRF studies. In our experiments, two films deposited on Si and SiO₂ substrates with known thicknesses measured by XRR and optical method were used as the reference samples.

For some samples [I,III,IV], thickness and composition was calculated by using electron probe microanalysis (EPMA) [280]. However, quantitative X-ray microanalysis of highly insulating media is very complicated task because electron beam irradiation can cause sample charging effects that increase uncertainty in thickness and composition determination [V]. It was found that HfO₂ film thickness value obtained from EPMA studies strongly depended on

the primary electron energy ($E_0 = 5\text{--}40$ keV), X-ray lines (Hf $K\alpha$, Hf $L\alpha$) used in analysis and substrate conductivity [V]. These effects were less pronounced at lower E_0 and thinner films, however. Besides, primary electron scattering seemed to be affected by the local electric fields in HfO_2 that were possibly related to the rechargeable defects. Therefore, film quality was also crucial. Nevertheless, by using Hf $L\alpha$ lines and smaller energies, accurate thickness determination of HfO_2 thin films was possible [V]. For composition measurements, $K\alpha$ lines were used for other elements. To convert the film mass determined by EPMA to the thickness, film densities measured by XRR were used. In our studies, this approach allowed accurate measurement of HfO_2 films with thicknesses up to ~ 100 nm. In the case of thicker films our density determination was not accurate enough and probably for this reason, the thickness values diverged from those measured by other methods [280,V].

3.3.3. X-ray photoelectron spectroscopy

X-ray photoelectron spectroscopy (XPS) studies were carried out to characterize the initial stage of the HfO_2 growth in terms of nucleation efficiency and possible interface formation [I,II]. In this method, X-rays or synchrotron radiation beam is focused on the sample surface and the energies of the scattered photoelectrons are recorded. The technique relies on the photoelectric effect that is described by the following relationship:

$$E_{kin} = h\nu - E_{bind} - \phi_{sample} \quad (6)$$

The kinetic energy of a photoelectron outside the sample, E_{kin} , is determined by the photon energy, $h\nu$, of the incident monochromatic radiation, binding energy, E_{bind} , of the electron in atom and the potential barrier present at the surface, i.e. the sample work function, ϕ_{sample} . Usually, E_{bind} that is a measure of the energy required to release an electron from its atomic or molecular orbital is the measure of interest. In a spectrometer, however, the electron kinetic energy is measured. Therefore the binding energy can be determined, if sample work function and photon energy is known.

The escape depth of an electron depends on the photon energy. Thus, surface sensitivity can be easily varied. Furthermore, the photo-ionization cross-section is a function of photon energy. This allows enhancing or suppressing photo-emission from different core levels. In XPS, information depth is determined by the inelastic mean free path (IMFP), which is a distance that an electron can pass through in a solid before losing a part of its energy. It turns out that 95% of the photoelectron signal comes from the surface region with a thickness of 3 IMFP values. The remaining 5% comes from deeper regions. In our studies, photon energy of 131 eV was used and the corresponding kinetic energy of Hf 4f photoelectrons was about 110 eV. The IMFP value of these electrons was

estimated to be ~ 0.5 nm. Hence, information originated from the thickness of about $d_{3IMFP} \approx 1.5$ nm. That is up to four outermost atomic layers.

It is known that the core level energy depends slightly on the chemical state of the atom. The change of a photoemission line position due to different chemical environments is known as a chemical shift. Although in a solid, the core electrons are localized at the atom and valence electrons are responsible for the chemical bonding, the local environment influences the binding energies of the core electrons as well. A chemical shift depends on the number, type and oxidation state of neighboring atoms and on the crystal structure of the film that all cause changes in the valence charge of the atom. This feature is used to understand the formation of an interfacial layer between a substrate and a film. For instance, Hf 4f doublet peak (Hf 4f_{7/2} and Hf 4f_{5/2}) position in Hf-silicate is shifted 0.4–0.7 eV to the higher binding energies than that in pure HfO₂ [286,287]. In the case of Si 2p peak analysis (Figure 21), the main Si⁰ peak is located at about ~ 99.3 eV while the components corresponding to higher oxidation state (Si⁴⁺ ~ 103 eV, Si^{*} ~ 102.5 , Si³⁺ ~ 102 eV etc.) are close to that making interpretation a very complicated task. Therefore, for exact IL composition analysis, angle-resolved XPS and synchrotron radiation is often used to understand the spatial formation of interface and possible diffusion processes [233,245,246].

All our XPS measurements were carried out in MAXlab synchrotron center in Lund, Sweden, at beamline 31 [288]. This beamline can be used either to record photoelectron spectra from selected areas on the sample surface or to scan the sample to obtain an image showing the lateral distribution of XPS signal [288,289]. In our studies, mainly spectroscopic measurements were carried out. Application of image mode (Figure 18) was limited by too low lateral resolution.

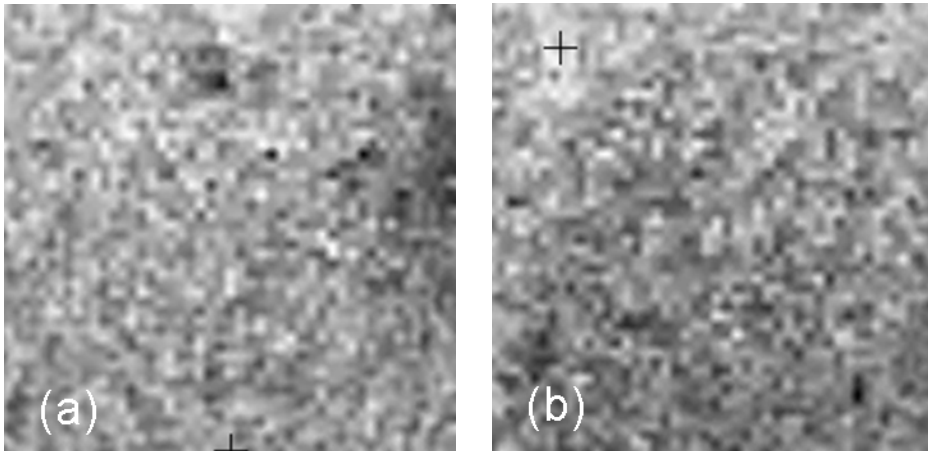


Figure 18. $120 \times 120 \mu\text{m}$ Hf4f scans of HfO₂ films deposited with (a) 15 cycles ($t_{ox} = 1.2$ nm) at 300°C and (b) 100 cycles ($t_{ox} = 1.0$ nm) at 600°C. Image pixel size is $2 \times 2 \mu\text{m}$.

3.3.4. Atomic force microscopy

Atomic force microscopy (AFM) measurements were used to study surface topography and roughness of films. All AFM experiments were carried out in intermittent-contact AFM (IC-AFM) mode while the films under investigation were exposed to the air. IC-AFM was needed to reduce possible artefacts caused by the adsorbate species on top of the film surface. In this mode of operation, the cantilever is oscillated close to its resonance frequency and the tip taps the surface only periodically, unlike the contact mode where tip is continuously in contact with the sample surface [290]. The surface topography is monitored through the changes of oscillation amplitude as tip-to-sample spacing fluctuates when surface is scanned. To improve resolution, *Ultralevels*TM probes with typical tip curvature of less than 10 nm were used. The equipment available for experiments described in this thesis was Autoprobe CP-II (Veeco), which was used for roughness measurements and imaging of surface structures. All roughness data were collected from the area of $5 \times 5 \mu\text{m}^2$ at least at three different regions of the sample surface. Surface root mean square (RMS) roughness and grain sizes were analyzed by Veeco SPMlab NT v6.0.2 software package.

4. RESULTS AND DISCUSSION

This chapter summarizes the ALD studies based on $\text{HfCl}_4\text{-H}_2\text{O}$ [I–V] and $\text{HfI}_4\text{-H}_2\text{O}$ [I], $\text{HfI}_4\text{-O}_2$ [I–II] chemistry routes.

4.1. Nucleation

The initial stage of HfO_2 growth studied at the substrate temperatures 300 and 600°C significantly depends on the silicon surface activation and halide chemistry used (Figure 19). It was revealed that due to the low number of favored adsorption sites, HfCl_4 nucleation onto hydrophobic Si-H surface (Figure 19 (a), HF-last) and on dehydroxylated silicon (Figure 19 (b)) is fairly limited. At 300°C, minimum growth delay of about 3–4 ALD cycles on HF-etched silicon substrate was determined [I], while after 4 cycles, weak Hf 4f peak was observed (Figure 19 (a)). In this case, the valence band (VB) structure was mainly determined by silicon substrate [291] and indicated islandic formation of HfO_2 . Other studies have reported incubation periods reaching up to 10–20 cycles at similar conditions [187,188,222]. To achieve continuous film, more than 50 cycles i.e. ~3 nm of HfO_2 has usually been needed [209]. By contrast, attenuated substrate signal and clear Hf 4f doublet peak was observed in our experiments on hydroxylated Si-OH surface already after 4 ALD cycles (Figure 19 (a)) [I,II]. After 7 cycles substrate signal was already insignificant and allowed us to conclude that the growth was predominantly two-dimensional on the hydroxylated surface. These results are in agreement with studies of other authors noting that wet oxide is sufficient to enhance chemisorption of HfCl_4 at 300°C [187,188,221,222,224,225].

At elevated temperatures, the starting Si-OH surface is likely turned to Si-O-Si surface because of the H_2O desorption discussed previously (Figure 5). Accordingly, HfCl_4 adsorption on silicon is not favoured at 600°C. Even after 50 cycles only substrate signal [291] is determined (Figure 19 (b)) while the Hf signal becomes significant after 100 cycles [I,II]. In the processes using HfI_4 as a precursor, improved nucleation achieved (Figure 19 (b)) is most probably because of higher reactivity of Hf precursor towards Si-O-Si terminated surface. For instance, a marked rate of HfO_2 growth can be revealed already after 30 cycles when $\text{HfI}_4\text{-O}_2$ precursor system is used [I]. As a result, both iodide-based processes studied provide more two-dimensional growth than the chloride process does.

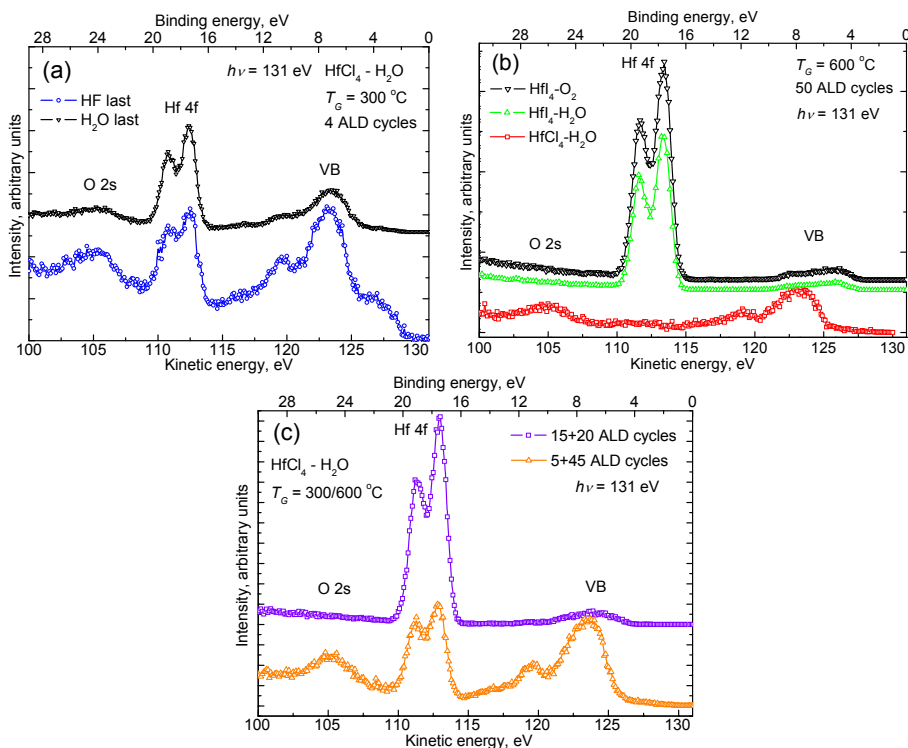


Figure 19. Hf 4f XPS spectra of HfO₂ films deposited (a) at 300°C on H₂O-last and HF-last silicon, (b) at 600°C on H₂O-last silicon from different precursor systems and (c) in two-step (300/600°C) processes on H₂O-last silicon at different seed layer thicknesses.

As HfCl₄ chemisorption at 600°C is more efficient on HfO₂ than on Si, a two-temperature ALD process was also studied. In this process, a low-temperature seed layer was deposited at 300°C to initiate HfO₂ growth at 600°C (Figure 19 (c)). Expectedly, nucleation at 600°C depended on the thickness and uniformity of the seed layer (Figure 19 (c)). Comparing Figure 19 (a) and (c), one can see that the HfO₂ layer deposited by applying 4 ALD cycles at 300°C covers Si more uniformly than the layer deposited by successive applying 5 cycles at 300°C and 40 cycles at 600°C. This result enables one to conclude that the seed layer that was deposited at 300°C by applying 5 cycles became non-uniform after heating the sample to 600°C. At somewhat greater thickness (15 cycles applied at 300°C), however, the seed layer remained uniform during heating because it resulted in uniform substrate coating after applying of only 20 cycles at 600°C (Figure 19 (c))

Two dimensional initiation of growth in the HfCl₄-H₂O process can be achieved by using hydroxylated starting surfaces and lower deposition temperatures or two-temperature deposition sequence completed at elevated temperatures. In the latter process, nucleation is improved but no advancement of

electrical properties appeared at the film thicknesses up to 10 nm [253]. Both leakage current and trap densities were higher than in the films deposited at 300°C noting that films were more defective either because of the interface structure or increased void density related to the crystallization and surface roughening.

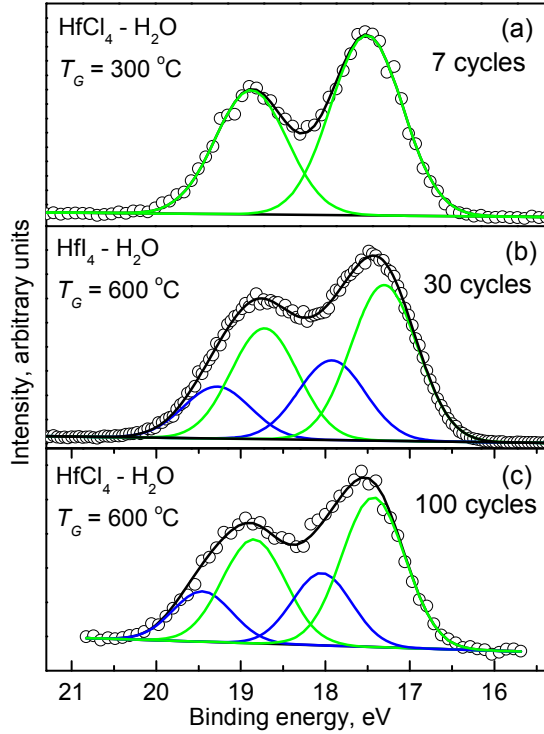


Figure 20. Fitting of Hf 4f peaks for HfO₂ thin films deposited at (a) 300°C from HfCl₄ and H₂O process, (b) at 600°C from HfI₄ and H₂O and (c) at 600°C from HfCl₄ and H₂O.

Fitting the Hf 4f doublet of the films deposited by applying 7 ALD cycles at 300°C (Figure 20 (a)) revealed contribution of only the main components. Consequently, HfO₂ is formed without any interfacial layer between growing film and the substrate material [11]. This result is in agreement with other reports as well [245,247]. Very thin HfO₂ films deposited at this temperature are still amorphous. Therefore oxygen diffusion via grain boundaries is limited. According to Miyata et al [239], the substrate oxidation is slow at deposition temperatures below 400°C and is influenced by the oxygen pressure and film thickness. In our studies, the water dose (pulse length) was possibly not high enough to reoxidize the substrate and/or the film was sufficiently uniform to block molecular oxygen diffusion. Low oxygen precursor pressure, on the other

hand, initiates formation of oxygen deficient HfO_2 , which inherently can consume some of the oxygen from the SiO_2 starting surface [235,236,241].

Contrarily, films deposited at $T_G = 600^\circ\text{C}$ (Figure 20) either from $\text{HfCl}_4\text{-H}_2\text{O}$ or $\text{HfI}_4\text{-H}_2\text{O}$ precursor systems, resulted in formation of silicate-like interfacial layer, as the main Hf 4f component contained additional high-energy doublet line [III]. This is in agreement with other reports noting that, at higher temperatures (exceeding 350°C), interfacial layer is formed [247,253].

From the contribution of the fitted doublet-line areas in Figure 20 one can note that the silicate component was more significant in the case of films deposited in the iodide-based processes than in the case of those grown from HfCl_4 and H_2O . Similarly, a series of Si 2p measurements of films deposited at $T_G = 600^\circ\text{C}$ from HfCl_4 and H_2O revealed interfacial layer formation (Figure 21). However, interpretation of the IL composition from these data is somewhat more complicated. In the Si 2p spectrum, several suboxide peaks appear between the main Si and SiO_2 peaks. These additional peaks may be related to the formation of Si-O-Hf bonds. Another possible explanation is that the band is composed of a Si^{4+} component of SiO_2 along with three intermediate components of the suboxide species, $\text{Si}^{1+}\text{-Si}^{3+}$, at the interface without invoking the possibility of the silicate formation. Anyway, suboxide shoulder clearly appeared at all film thicknesses studied, noting that non-stoichiometric SiO_x or silicate-like interfacial layer was formed during the deposition. Possibly, both silicate and SiO_x part is present in the IL because Si oxidation is very fast at these temperatures [239]. Due to low reactivity of HfCl_4 towards Si surface, the surface is non-uniformly covered with the metal precursor and HfO_2 film material in the initial stage of deposition and the silicon substrate can be easily oxidized during the H_2O pulse.

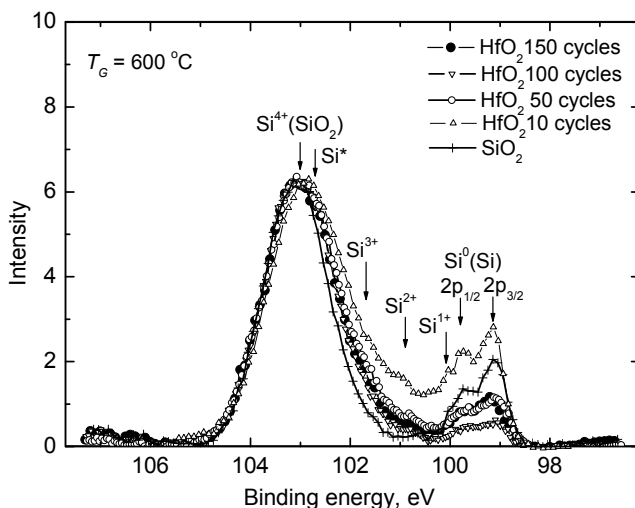


Figure 21. Si 2p XPS spectra of SiO_2 and HfO_2/Si structures with HfO_2 thin films deposited at 600°C by applying 10–150 cycles.

The increase of the silicon substrate signal that seems to take place during the first 10 cycles (Figure 21) is likely an artifact connected with the inhomogeneity of the deposited layer and dissimilar SiO₂ thicknesses on the different Si substrates used. Following deposition of additional film material resulted in the decrease of signals from both pure silicon substrate and suboxide. This result is an indication of further oxidation of silicon substrate, at least in its uncovered regions.

4.2. Growth rate

4.2.1. Influence of substrate temperature and carrier gas flow on growth rate

HfCl₄-H₂O ALD process followed the self-limiting nature over a T_G range 180–750°C [IV,175,269] studied in this work. In this range, the growth rate decreases on silicon as well as on quartz substrates with increasing T_G [I,III,IV,202,247], most probably due to decreasing concentration of the surface hydroxyl groups and corresponding changes in possible reaction mechanism [175]. Constant growth rate observed in the T_G region of 600–750°C indicates that at higher temperatures, the concentration of adsorption sites and the mechanism of exchange reactions are independent of temperature. An explanation for this behavior is dehydroxylation of surface with the increase of temperature to 600°C and terminating the H₂O treated surface by bridged oxygen at higher temperatures [231]. At all temperatures studied, somewhat higher growth rate was obtained on quartz substrates, especially at elevated temperatures allowing one to suggest different film structure and/or surface roughness compared to those of films deposited on silicon substrates.

Somewhat more surprising result is the dependence of the growth rate on the carrier gas pressure and flow under conditions that ensure selflimited ALD-type growth. QCM studies carried out at 225–300°C indicated that increased carrier gas flow expectedly improved precursor transportation as saturation of Δm_0 was obtained at shorter precursor pulses. At the same time the saturation level also depended on the carrier gas flow and decreased with the increase of that (Figure 22).

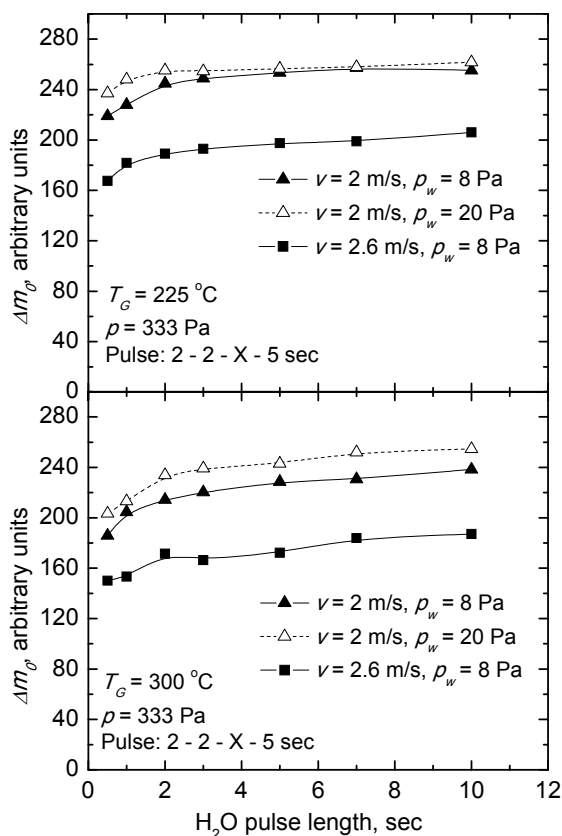


Figure 22. QCM studies of the impact of growth temperature, carrier gas flow rate and water dose to the $\text{HfCl}_4\text{-H}_2\text{O}$ ALD process.

The saturation level depended also on the partial pressure of H_2O varied from 8 to 20 Pa. The impact of H_2O pressure on Δm_0 was more distinguished at 300°C than at 225°C . However, the increase was only 8–10 % when the pressure was increased from 8 to 20 Pa (Figure 22). This change is smaller than the corresponding decrease caused by the increase of v . In order to understand possible role of overlapping the precursor pulses and corresponding CVD-type reactions, both purge periods were varied from 1 to 10 s. Overlapping was an issue at short purge periods (0.2–1 sec), lower v and lower T_G (particularly at $T_G \leq 225^\circ\text{C}$). At lower carrier gas flow rates, short purge periods resulted in increased growth rate that was most likely connected with mixing the precursors in the gas phase. The highest changes in Δm_0 were caused by the reduction of the purge following the H_2O pulse. At higher v values and purge periods exceeding 2 sec, the contribution of precursor overlapping was negligible [IV]. In further studies that were carried out to investigate the effect of carrier gas on the growth rate, only

these process parameters were used that ensured ALD growth with negligible contribution of CVD-type processes.

Ex-situ measurements confirmed a significant effect of v and chamber pressure, p , on the growth rate of HfO_2 . The increase of v from 2.6 to 5.4 m/s at constant p reduced the growth rate from 0.12 to 0.087 nm while at constant v , an increase of p from 200 to 740 Pa reduced the growth rate from 0.15 to 0.085 nm [IV]. Analysis of the results of QCM and ex-situ measurements allowed a conclusion that at $T_G \leq 350^\circ\text{C}$, v and p have more significant impact on the surface reactions during and/or after H_2O pulse influencing dehydroxylation of the surface and desorption of H_2O from the surface [IV].

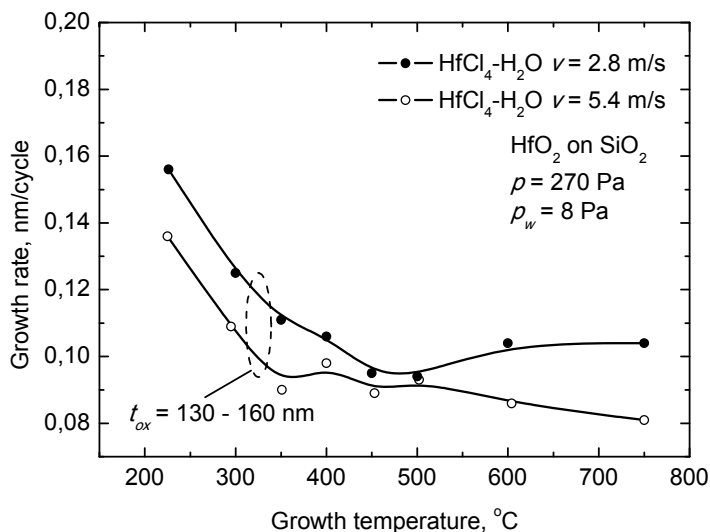


Figure 23. Growth rate as a function of T_G for different precursor combinations and different carrier gas flow rates.

It is worth noting that the increase of substrate temperature as well as carrier gas flow and pressure result in a decrease of growth rate (Figure 23) possibly due to faster dehydroxylation of the surface after H_2O pulse [IV]. Usually an increase in T_G results in more complete exchange reactions i.e. also in lower concentration of impurities that can remain in the film. The increase of the carrier gas flow rate and pressure provides a similar effect. For instance, chlorine concentration can be well diminished by choosing either higher v or p in the growth zone [IV]. At 300°C , the chlorine concentration decreased from 0.34 ± 0.04 to 0.18 ± 0.03 mass % when v was increased from 2.6 to 5.3 m/s. The increase of chamber pressure from 330 Pa to 730 Pa reduced the chlorine content from 0.34 ± 0.04 to 0.24 ± 0.03 mass% [IV].

4.2.2. Influence of film thickness on growth rate

In the $\text{HfCl}_4\text{-H}_2\text{O}$ process, HfO_2 started to grow without noticeable incubation period at substrate temperatures of 300°C and below [I,III]. Fairly constant slope of the thickness versus number of cycles dependence was determined at T_G of 180°C . Marked nonlinearity appeared, however, for the films grown at $225\text{--}450^\circ\text{C}$. At 225°C , growth rate of 0.14 nm per cycle was determined for the thickness range $0\text{--}100\text{ nm}$ while for thicker ($100\text{--}350\text{ nm}$) films, the slope of the thickness versus number of cycles curve reached 0.19 nm per cycle. At T_G of $255\text{--}300^\circ\text{C}$, such transition appeared already in the range of $40\text{--}50\text{ nm}$, while at 450°C , a growth rate increase was observed after reaching the thickness of $10\text{--}12\text{ nm}$. As a result of these changes the mean growth rate determined as the ratio of the film thickness to the number of cycles applied also depended on the film thickness (Figure 24). It should be noted that these changes caused in the growth rate by the increase of film thickness are in correlation with the thickness values at which crystallization starts in HfO_2 films deposited by ALD from HfCl_4 and H_2O [175,212,247].

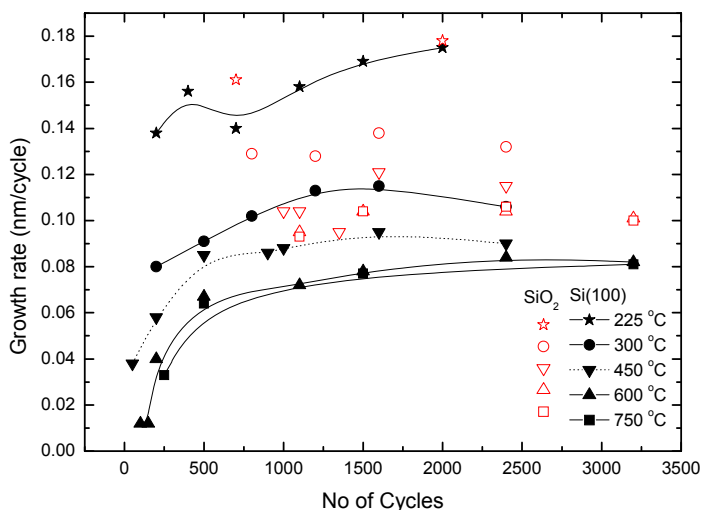


Figure 24. Mean growth rate as a function of the number of ALD cycles for HfO_2 films deposited on $\text{Si}(1\ 0\ 0)$ and SiO_2 (fused silica) substrates at various temperatures. Partial pressure of H_2O was 8 Pa .

In the T_G range of $600\text{--}750^\circ\text{C}$, incubation periods up to $100\text{--}200$ cycles were observed for the $\text{HfCl}_4\text{-H}_2\text{O}$ process while further the thickness increased without nonlinearities, which would exceed the experimental uncertainty. Clearly the reactivity of HfCl_4 towards dehydroxylated Si-O sites is limited at these temperatures, as the same process on HfO_2 buffer layer [I] induced growth rate of about 0.03 nm already at the very first cycles. Markedly faster growth

obtained on HfO₂ is evidently due to higher abundance of hydroxyl groups on the surface of HfO₂ or higher reactivity of HfCl₄ towards the dehydroxylated surface of HfO₂ when compared with the reactivity towards dehydroxylated SiO₂.

At T_G of 600°C, HfI₄-H₂O and HfI₄-O₂ [I] processes started without any incubation period and showed higher growth rate in following deposition process than the HfCl₄-H₂O process did. Likely, differences in reaction mechanisms [231] may induce higher growth rate in the iodide process. Most probably, partial decomposition of iodide precursor on substrate surface [292] is a reason for why at these temperatures, HfI_x species could be adsorbed even without the exchange reactions that have been observed and considered to be responsible for ALD at lower temperatures [292].

4.3. Phase composition and structure development

4.3.1. Influence of substrate material on structure of films

Somewhat surprisingly, GIXRD studies revealed differences in the crystallite orientations obtained in relatively thin films deposited on Si(1 0 0) and Si(1 1 1) substrates at 300°C (Figure 25) whereas at higher temperatures, no obvious differences occurred.

In the film grown at 300°C to a thickness of 50 nm (500 ALD cycles applied) on Si(1 1 1) substrate, the $\bar{1}$ 1 1 reflection was the most intense while on Si(1 0 0), the 1 1 1 reflection showed the highest intensity (Figure 25 (a)). This indicates that at least some of the crystallites were nucleated at the substrate surface and the orientation was partially determined by the crystallographic orientation of the substrate, although amorphous phase dominated in the films in their very initial growth stage [I]. After 700 ALD cycles (Figure 25 (a)) the difference in orientation of crystallites became weaker and the 0 0 2 reflection obtained the highest intensity independently of substrates used.

These data well correlate to the HRTEM [247] and XPS [III] results confirming that formation of HfO₂ on silicon without any interfacial SiO_x or Hf-silicate layer can be achieved at T_G of 300–350°C. As mentioned earlier, initial nucleation largely depends on the hydroxyl group density at the starting surface, while different orientation of the substrate may either invoke or suppress substrate oxidation during initial film growth. Therefore, in the T_G range of 300 to 350°C nucleation differences provoked orientation change, possibly, due to the different starting layer as well as by uneven film formation. The latter explanation applies also for the growth at somewhat higher temperatures where non-uniform nucleation, which is more significant on silicon substrates, promotes agglomeration and supports development of preferential (0 0 1) orientation [III]. Indeed, films deposited in a T_G range of 400–500°C on silicon showed more developed texture compared to the films deposited on SiO₂ substrates (see Section 4.3.3).

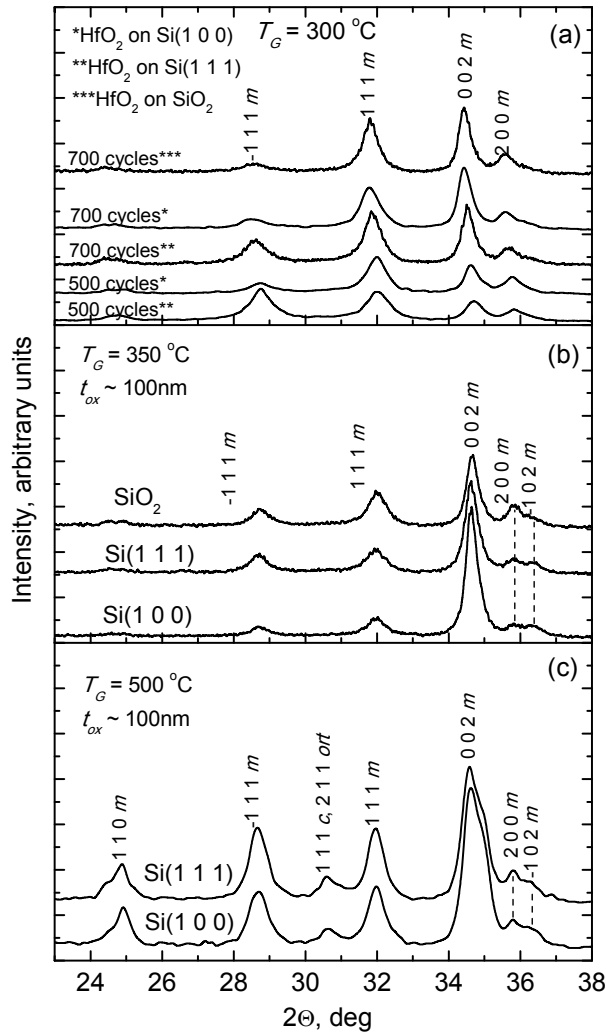


Figure 25. GIXRD patterns of films deposited at (a) 300°C, (b) 350°C and (c) 500°C with various numbers of ALD cycles applied. Films were deposited at $p_w = 8$ Pa. Reflections of cubic and monoclinic phases are denoted by *c* and *m*, respectively, after Miller indices

According to our studies, the effect of substrate orientation on the growth rate did not exceed the experimental uncertainty at any deposition temperature used. This was somewhat anticipated result as the overall changes in orientation of crystallites related to substrate orientation were relatively weak compared with those caused by the development of the (0 0 1) orientation with increasing film thickness [III].

4.3.2. Influence of film thickness and growth temperature on phase composition and texture development

GIXRD studies of films deposited at 225, 255 and 300°C showed clear dependence of the crystallinity on the film thickness. Indeed, no crystalline phases were detected in the films with the thicknesses up to 50 nm deposited at 225°C. Cubic phase was found in the outer layers of about 100 nm thick films, in clear correlation with earlier HRTEM studies [247]. With the further increase of the film thickness, pronounced monoclinic phase with preferred (0 0 1) orientation was formed in these films (Figure 26(a)).

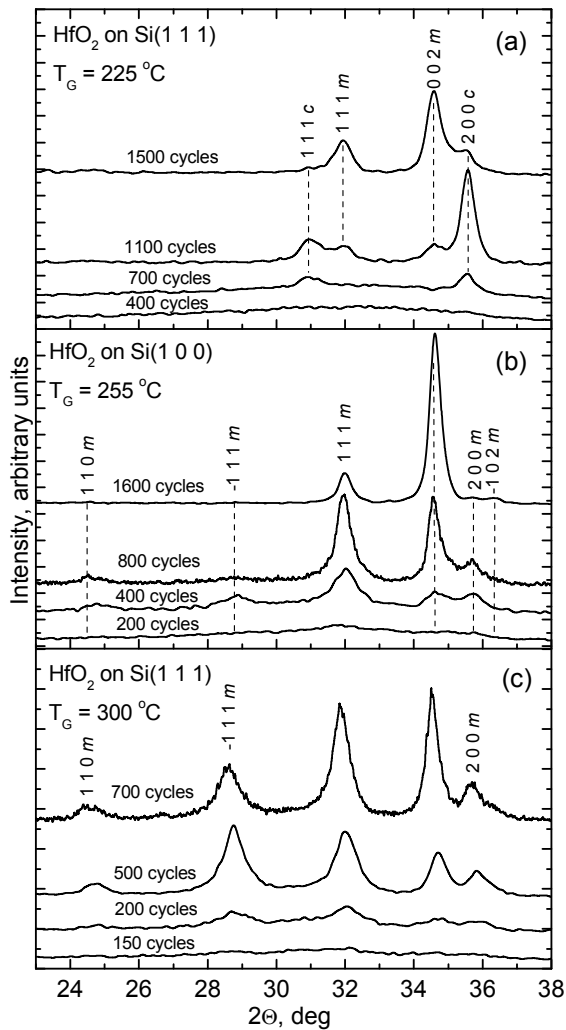


Figure 26. GIXRD patterns of films deposited at different temperatures and numbers of ALD cycles applied. Films were deposited at $p_w = 8$ Pa. Reflections of cubic and monoclinic phases are denoted by *c* and *m*, respectively, after Miller indices.

In the films deposited at 255°C and higher temperatures, monoclinic HfO₂ as the main crystalline phase was detected (Figure 26 (b) and (c)). The $-1\ 1\ 1$ reflection was most intense in the case of films deposited at 300°C on Si(1 1 1) substrates while the $1\ 1\ 1$ reflection was most intense one for the films deposited on both SiO₂ and Si (1 0 0) substrates. Thus, some crystallites nucleated at the substrate surface and their orientation was at least partially determined by the substrate orientation, as discussed in previous section. The effect of substrate expectedly became weaker with the increase of the film thickness and the 0 0 2 reflections started to dominate in diffraction patterns of thicker films deposited on all substrates studied in this work.

RHEED studies of films deposited at 300°C revealed, in agreement with the GIXRD measurements, formation of the amorphous phase at thicknesses up to 8–10 nm [I]. Thicker films grown at this temperature contained detectable amounts of monoclinic phase according to RHEED [I] as well as GIXRD (Figure 26) data. In the thinnest films deposited at 600°C, RHEED detected face-centered cubic phase [I]. With the increase of the thickness to 10–15 nm, the monoclinic phase also appeared while after increasing the film thickness above 30 nm only monoclinic phase was observed by the surface-sensitive RHEED method. When comparing different chemistries, most developed crystal structure was obtained in the case of HfCl₄–H₂O process, while iodide process yielded reasonably high amount of amorphous phase in the initial stage of deposition. Still, comparing different iodide processes, somewhat better crystallinity was observed in the HfI₄–O₂ process than in the HfI₄–H₂O process.

Lower concentration of crystalline phases in the films deposited at substrate temperatures below 300 °C is obviously connected with the high impurity content and kinetic factors, which limit the structure formation during the growth process. At low T_G , the stability of the intermediate oxychloride-like surface species evidently increases causing higher amount of residues in the films [182]. In order to achieve higher degree of crystallinity and lower impurity concentration, increased H₂O dose has been usually applied [210–212]. In our case, increase of p_w from 8 to 20 Pa caused diminishing of the chlorine content from 4.1 at% to 3.4 at%, respectively, for $T_G = 300^\circ\text{C}$ [III]. At higher temperatures, nucleation processes evidently influenced crystallization in the initial stage of deposition. HfCl₄–H₂O process showing the most non-uniform nucleation [I] resulted in more crystalline films compared with those obtained in the HfI₄-based processes.

According to the standard Bragg-Brentano XRD studies, all films that were deposited in the T_G range of 300–750°C and were thicker than 30 nm, contained mainly polycrystalline monoclinic phase [III,IV]. Comparison of the crystal structures in the 100–250 nm thick films deposited on single crystal silicon and fused silica substrates can be found in Figure 27.

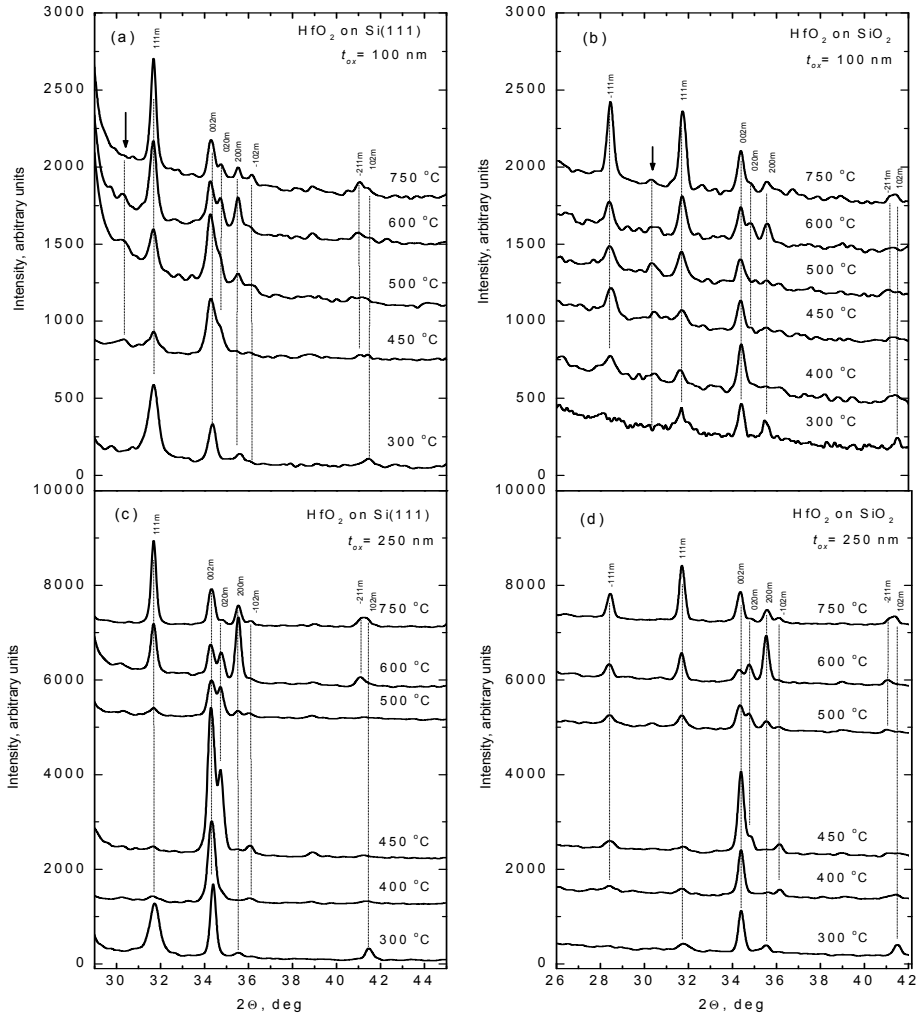


Figure 27. Bragg-Brentano XRD patterns of (a, b) 100 ± 10 nm and (c, d) 250 ± 25 nm thick HfO_2 films grown on (a, c) $\text{Si}(1\ 1\ 1)$ and (b, d) SiO_2 at different temperatures. Films were grown at $p_w = 8$ Pa. Reflections of monoclinic phase are denoted by m after Miller indices.

Largest differences in the textures of films deposited on different substrate materials were revealed for $T_G = 300^\circ\text{C}$ (Figure 27). HRTEM [247] and XPS [IV] studies indicated that at 300°C , HfO_2 film was formed on silicon without any interfacial layer. This suggests that initial stage of the growth could be different, as the very first cycles on Si substrate greatly depend on the surface pretreatment i.e. on the surface activation [I]. As can be seen in Figure 27 (a) and (b), 100 nm film on $\text{Si}(1\ 1\ 1)$ was primarily (1 1 1)-oriented, while that deposited on SiO_2 substrate showed preferential (0 0 1) orientation. In the films

with the thickness of about 250 nm deposited at the same temperature, (0 0 1) orientation was dominant in both cases. However, in the case of films deposited on silicon substrates, the 1 1 1 reflection was still relatively strong, while in the films grown on quartz, the intensity of this reflection is very low. Relative peak calculation [III] showed similar intensity ratios I_{002}/I_{111} for 250 nm thick films deposited on silicon and 100 nm thick films deposited on quartz. Thus, initially the film orientation was evidently determined by the crystalline Si(1 1 1) substrate as already discussed but after reaching at certain thickness the orientation of preferential growth (i.e. (0 0 1) orientation) started to dominate. This assessment is also based on comparison of θ - 2θ XRD patterns with the GIXRD data (Figure 26), indicating that preferential (0 0 1) orientation is more developed in upper layers of the films grown on silicon substrate. As amorphous SiO₂ substrate initially lacks such guiding force, films tend to grow with preferential (0 0 1) direction from the very beginning of deposition. No major differences in XRD and GIXRD results were revealed in that case. Expectedly, no marked effect of silicon substrates on the film texture has been observed, when films with a thickness of about 400 nm have been studied [202].

However, some studies have shown clearly preferred (0 0 1) direction on silicon [255] already for about 30 nm thick films. In the latter work, a short ALD cycles with time parameters of 0.4-0.5-0.5-0.5 s were used for deposition while the pressure was around 1 kPa in the reaction chamber [255]. Unfortunately, no information about the carrier gas flow rate was reported in the publication describing that work. Difference in the carrier gas flow rate may explain faster formation of (0 0 1) texture, as our studies have revealed more significant development of this texture at higher carrier gas pressures and flow rates [IV] whereas according to our studies [IV], most significant dependence of crystallite orientation on the gas flow parameters occurred in the films deposited at 300°C. Hausmann et al. [255] reported most dominant (010) reflection of monoclinic phase for about 100 nm thick HfO₂, but they used a different precursor system and also lower pressure (33 Pa) in the reaction zone, although the linear flow rate was comparable (3.0 m/s) to that used in our experiments.

In thicker films deposited on Si(1 1 1) at 450°C, additional (0 1 0) orientation clearly appeared (Figure 27), although the intensity of the 0 1 0 peak was still 2 times lower than that of the 0 0 1 peak. In the films deposited on quartz, the 0 1 0 peak was also noticeable but minor compared to that of the films deposited on silicon substrates. In thinner films deposited at 500°C, the 1 1 1 reflection was of marked intensity, while in thicker films deposited at this temperature relatively intense 0 1 0 peak was present again. At temperatures of 600–750°C polycrystalline films without well-developed texture were formed. In thinner films deposited at 600°C, the 1 1 1 peak was the most intense one and the relative intensities of the peaks were very similar for the films deposited on Si and SiO₂ substrates. This was an expected result, as at this temperature, SiO₂ interfacial layer is formed on silicon substrate in the initial stage of deposition [II].

Strongest influence of the carrier gas flow rate and pressure on the structure of HfO_2 films was observed at 300°C [IV]. As mentioned already, higher chamber pressure at constant flow rate caused preferential growth of thin films with (0 0 1) orientation. Similarly higher gas flow rate supported dominating of (0 0 1) orientation. For comparison, at T_G of $450\text{--}750^\circ\text{C}$, changes in carrier gas flow rate and pressure did not have marked influence on the film structure and texture any more.

Returning back to the effect of the film thickness on the growth rate, one can summarise that at the deposition temperatures studied, the largest variations in the growth rate with increasing film thickness occurred in the thickness ranges where transition from the amorphous to crystalline phase was observed. Therefore, one can note that crystallization influences the growth rate. The influence of the further phase transitions on the growth rate that could have appeared at $T_G = 225^\circ\text{C}$, where transition from cubic phase to monoclinic one was observed, did not exceed uncertainty of our experimental methods. Instead, the texture development that was due to faster growth of (0 0 1)-oriented crystallites caused a noticeable increase of the growth rate at temperatures $400\text{--}450^\circ\text{C}$.

4.4. Topography

4.4.1. Nucleation uniformity and surface roughness of HfO_2 thin films

Surface roughness of the films in the initial stage of their growth was studied in detail at the deposition temperatures of 300 and 600°C . As shown above (Figure 19 (a) and Figure 24), HfO_2 deposition starts without delays at 300°C . This result indicates that nucleation is uniform. Data of AFM measurements well supported this conclusion as after applying 7–15 ALD cycles (Figure 28, Figure 29), i.e. deposition of films with the thicknesses up to 1.7 nm, the surface RMS roughness value that equaled to 0.2 nm only slightly exceeded that of the pure substrate, which was $0.1\text{--}0.15$ nm.

With increasing thickness of the HfO_2 layer, the absolute value of the surface roughness gradually increased (Figure 29) while the ratio of the surface roughness to the mean film thickness, i.e. the relative roughness, continuously decreased (Table 2). It is clear that this kind of growth does not differ significantly from the two-dimensional one because the surface roughness value remains small compared to the film thickness (Figure 29). Most probably, relatively high amount of amorphous phase formed in the films under these deposition conditions suppressed crystallization and possible grain boundary formation and, in this way, also limited the surface roughening.

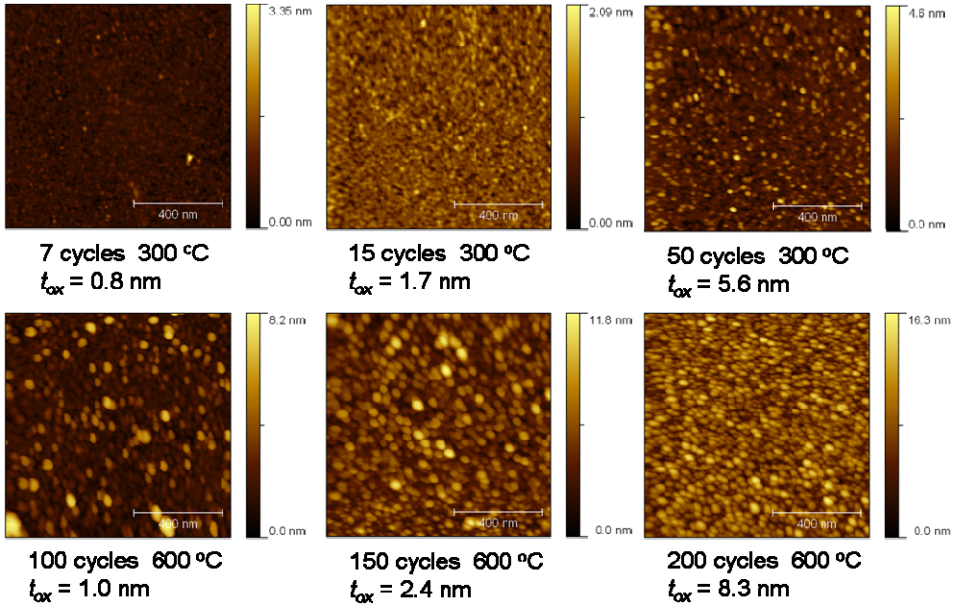


Figure 28. $1 \times 1 \mu\text{m}$ IC-AFM topography patterns of HfO_2 films deposited at 300 and 600°C by applying 7 to 200 ALD cycles.

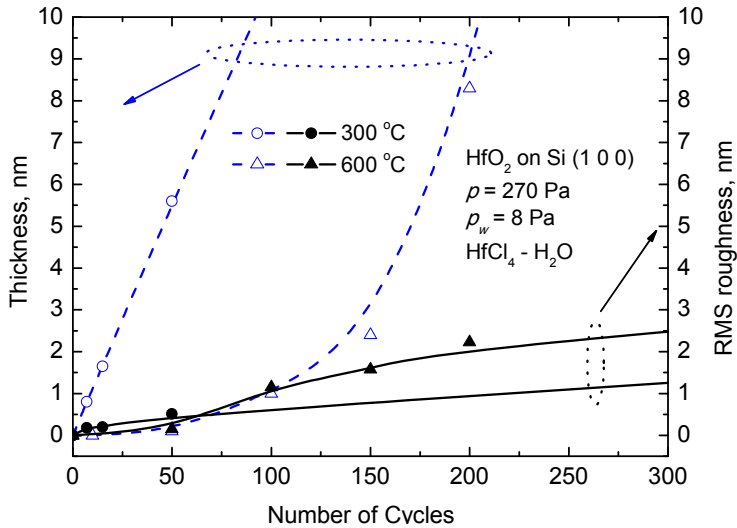


Figure 29. Thickness and RMS roughness vs number of ALD cycles for HfO_2 films deposited at 300 and 600°C .

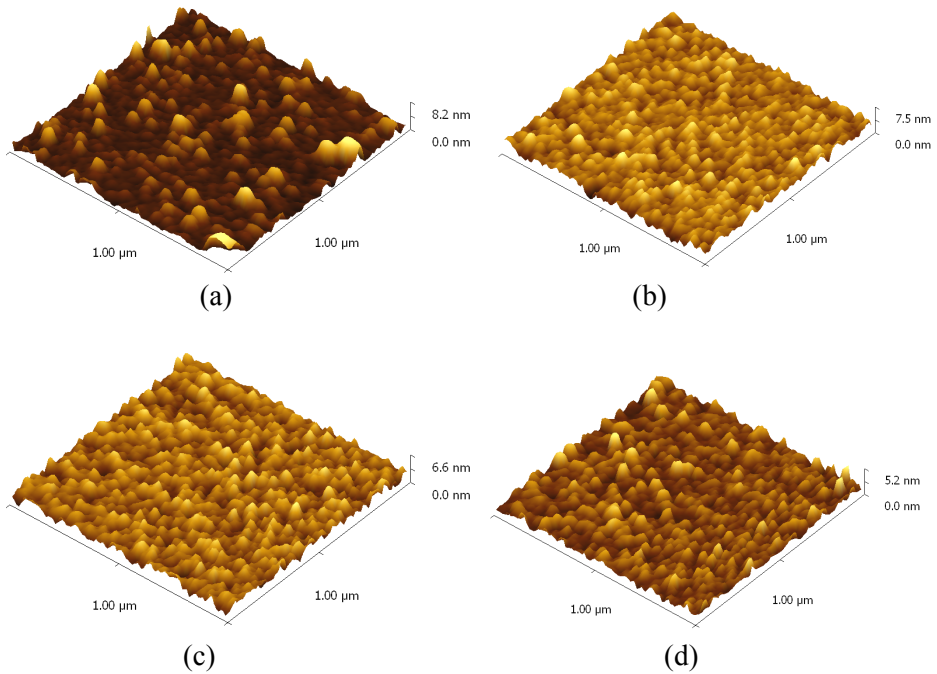


Figure 30. IC-AFM topography images of films after 100 ALD cycles (a),(c),(d) at 600°C and (b) 300/600°C by applying (a),(b) $\text{HfCl}_4\text{-H}_2\text{O}$, (c) $\text{HfI}_4\text{-O}_2$ and (d) $\text{HfI}_4\text{-H}_2\text{O}$ chemistry routes. Films were deposited at $p_w = 8$ Pa and using 2.6 m/s flow rate.

Contrarily, at $T_G = 600^\circ\text{C}$, nucleation is nonuniform in the $\text{HfCl}_4\text{-H}_2\text{O}$ ALD process [I–III] resulting in films with high surface roughness from the beginning of growth (Figure 29). Correspondingly, the RMS surface roughness of thinner films was close to the mean thickness (Table 2) and the growth of HfO_2 was clearly three-dimensional under these conditions.

In order to improve the uniformity of film growth at higher temperature we used an HfO_2 buffer layer that was deposited at 300°C (Figure 30(b)). As a result, at similar film thickness, we were able to reduce the relative roughness significantly (Table 2). Even better results were achieved when $\text{HfI}_4\text{-O}_2$ and $\text{HfI}_4\text{-H}_2\text{O}$ processes were used for deposition of HfO_2 films (Figure 30 (c), (d), Table 2).

Table 2 AFM results of the films deposited at different temperatures and precursor systems used.*

Process	T_G , °C	Substrate	No of ALD cycles	Thickness, nm	RMS roughness, nm	Relative roughness, %
HfCl ₄ -H ₂ O	300	Si	7	0.8	0.2	25
HfCl ₄ -H ₂ O	300	Si	15	1.7	0.2	12
HfCl ₄ -H ₂ O	300	Si	50	5.6	0.5	9
HfCl ₄ -H ₂ O	600	Si	100	1.0	1.2	120
HfCl ₄ -H ₂ O	600	Si	150	2.4	1.6	67
HfCl ₄ -H ₂ O	600	Si	200	8.3	2.2	27
HfCl ₄ -H ₂ O	300/600	Si	15+90	5.4	0.9	17
HfI ₄ -H ₂ O	600	Si	100	6.0	0.7	12
HfI ₄ -O ₂	600	Si	100	8.0	1.0	13

*N₂ flow used corresponded to linear flow rate of 2.6 m/s at T_G of 300°C.

4.4.2. Influence of crystallization processes on surface roughness

In Figure 31, thickness and RMS roughness are plotted to better understand topography development related to the thickness increase in the range where most significant changes in crystallinity appear in the films deposited at 225°C. In a region of 0–700 cycles (0–100 nm), predominantly amorphous films were obtained while the growth rate was 0.14 nm/cycle. It is noteworthy that surface roughness was nearly proportional to the film thickness increasing up to 3.1 nm with the increase of the film thickness to 100 nm.

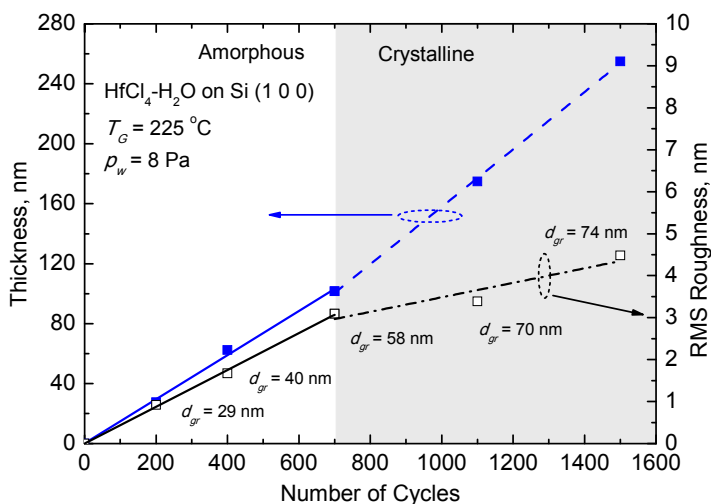


Figure 31. Thickness and RMS roughness of HfO₂ films deposited at 225°C on Si(1 0 0) as a function of ALD cycles. Indication of the average AFM grain size is denoted as d_{gr} .

This dependence significantly differs from the one observed for films deposited at 300 and 600°C. Afterwards, in the range of 700–2000 cycles (100–350 nm) where marked amounts of cubic and monoclinic polymorphs were formed in the films (Figure 26 (a)), the growth rate increased to 0.19 nm/cycle but the surface roughness continued to increase with much lower rate than earlier. As a result of these changes, the RMS roughness value increased only from 3.1 to 4.5 nm with the increase of film thickness from 100 to 240 nm (Figure 31).

AFM images (Figure 32) as well as results of HRTEM studies [247] allow a conclusion that initial relatively fast roughening is connected with the evolution of crystallites in an amorphous layer. These crystallites, which are relatively far from each other in thinner films and randomly distributed, grow faster than the amorphous phase does and, in this way, start to increase the surface roughness (Figure 32). Further decrease in the rate of roughness development is likely connected with the coalescence of those grains. Similar amorphous-to-crystalline growth transition takes place also at 300°C but usually in a thickness region of 0–35 nm and is highly dependent on the process parameters such as H₂O dose, surface pre-treatment, N₂ flow rate, precursor combination etc. In our studies,

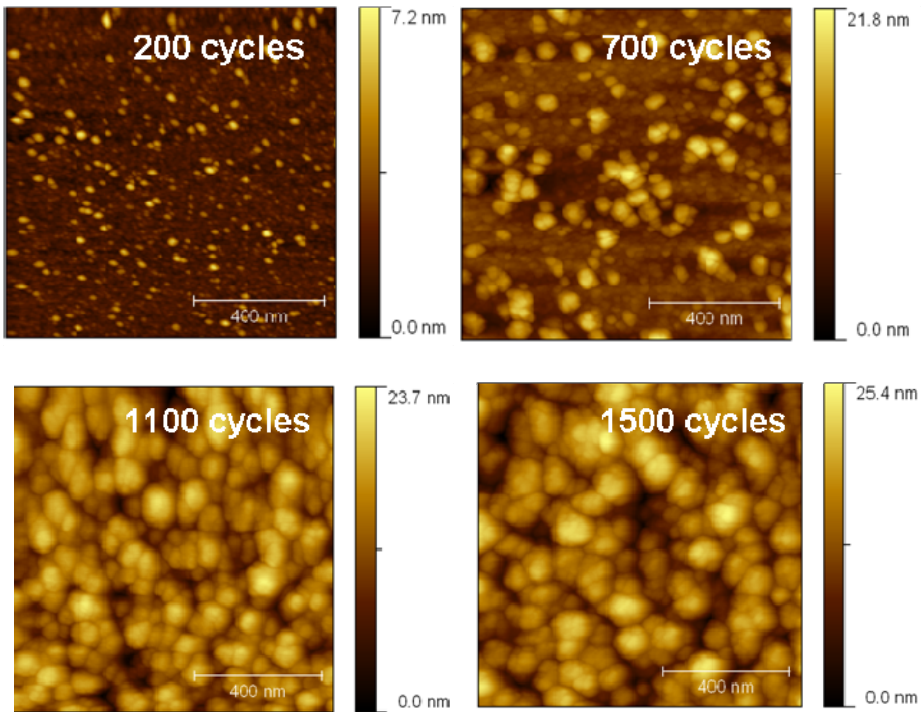


Figure 32. 1×1 μm IC-AFM topography patterns of HfO₂ films deposited at 225°C by applying 200–1500 ALD cycles. Films were deposited using HfCl₄–H₂O chemistry routes, water partial pressure of 8 Pa and carrier gas flow rate of 2.6 m/s.

marked amounts of crystalline phase were recorded by GIXRD for the films with thicknesses ~ 20 nm and greater (Figure 26 (c)). Correspondingly, an increase of the growth rate can be observed starting from similar film thicknesses. Still, contribution of crystallization to overall growth rate and surface roughness was less obvious at 300°C than at 225°C, probably also due to the smaller sizes of crystallites (Figure 34). At 600°C, crystalline phases were formed already from the very beginning of the growth process, at least in the $\text{HfCl}_4\text{-H}_2\text{O}$ process. Therefore, no phase transitions influencing the growth rate occur at this temperature. Instead, nonuniform nucleation related to low reactivity of precursors towards silicon substrates and the formation of bigger crystallites [III] invoke three dimensional film growth, which results in surface RMS roughness that is comparable to the mean film thickness in the initial stage of deposition.

4.4.3. Influence of growth temperature and carrier gas flow rate on surface roughness

Films with thicknesses of 90–250 nm were used to study the effect of T_G and carrier gas flow rate on the surface roughness of HfO_2 films deposited on $\text{Si}(1\ 0\ 0)$ and SiO_2 substrates. To reduce the effect of the thickness variations on the roughness [201,267], relative roughness values (Figure 33(a)) interpolated to constant thickness were used [III]. Obviously, relatively high surface roughness of films deposited on Si and SiO_2 substrates at 225°C (Figure 33 (a), III) was mainly due to the presence of conically shaped proto-crystallites, which grew faster than alternatively smooth amorphous phase between the crystallites (Figure 32) [247]. In the T_G range of 300–450°C higher surface roughness clearly correlated to the film texture [III].

Higher flow rates of carrier gas did not influence the roughness in the T_G range of 500–750°C (Figure 33(a)). In this range, the effect did not exceed experimental uncertainty whereas at lower temperatures, a significant influence of the carrier gas flow rate on the surface roughness occurred. Particularly, higher v reduced roughness in the T_G range of most preferential texture formation. In the range of 225–300°C, by contrast, films with rougher surfaces grew at higher v values.

In the T_G range of 300–450°C, higher surface roughness clearly correlates with the texture [III]. For instance, films deposited on silicon had rougher surfaces as well as more developed texture compared with the films of similar thickness deposited on quartz. Although faster growth of (0 0 1)-oriented crystallites was observed [III], sizes of these crystallites reached only 36 nm in about 100 nm thick HfO_2 films deposited on silicon (Figure 34 (a)). With the increase of film thickness to 250 nm crystallite sizes increased to about 70 nm (Figure 34 (b)). Similar tendency was observed for films deposited on quartz substrates. However, in thinner films, the crystallites were about 30% smaller

on SiO₂ substrates than those formed in the films deposited on silicon. At those temperatures crystallites with the (1 1 1) orientation possessed even smaller sizes, staying between 12–20 nm on both substrates at the thicknesses 100–250 nm. AFM studies of about 100 nm thick films determined grain sizes of 40–54 nm in the lateral direction (Figure 34 (c)). These values are comparable to grain sizes of ~35 nm determined for similar films by HRTEM [247]. With the increase of the film thickness to 250 nm the grain sizes measured by AFM increased to 54–63 nm.

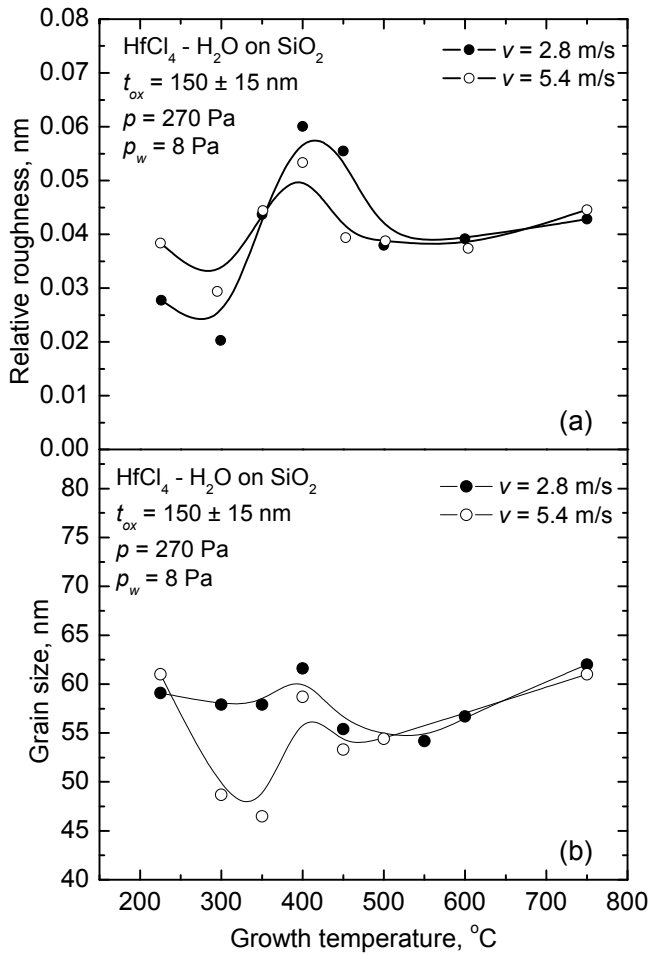


Figure 33. (a) Relative roughness and (b) grain size as a function of growth temperature of the films deposited on SiO₂ substrate at different carrier gas flow rates. Roughness data is collected from the scanning area of 5×5 μm.

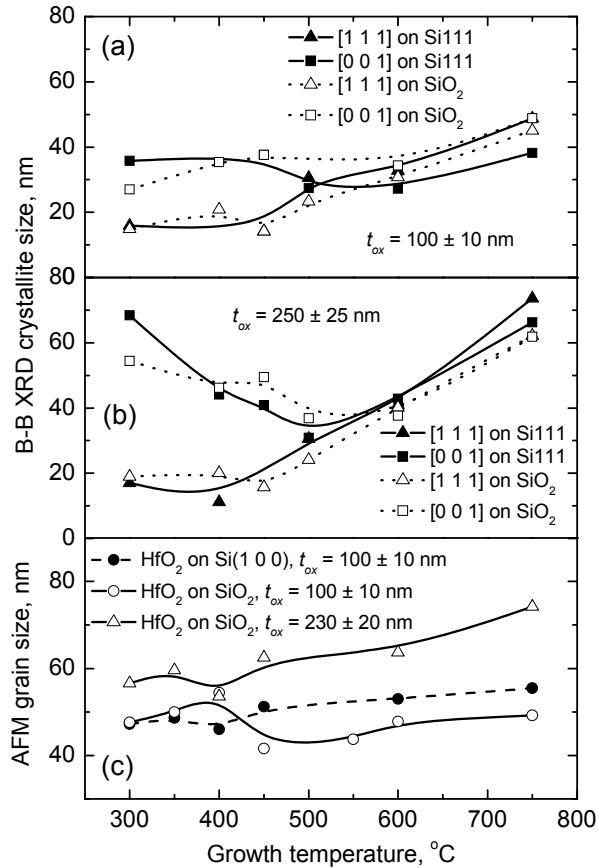


Figure 34. (a,b) XRD crystallite size and (c) AFM grain size as a function of growth temperature of films deposited on SiO₂ and Si (1 0 0) substrate.

Roughness decrease observed with the increase of T_G from 450 to 500°C is consistent with less developed texture of the films deposited at higher temperatures [III]. Further increase of the surface roughness at temperatures above 500°C is evidently related to monotonic increase of grain sizes determined from AFM images as well as crystallite sizes measured by XRD. Grain analysis of about 100 nm thick films indicated that lateral crystallite sizes were systematically lower on quartz than on Si. An exception is the range of medium temperatures, especially around 400°C.

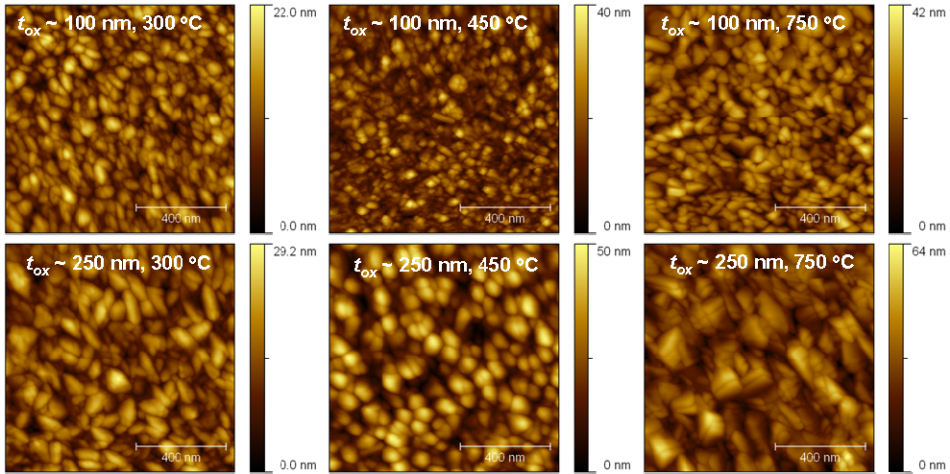


Figure 35. $1 \times 1 \mu\text{m}$ IC-AFM topography patterns of HfO_2 films with thicknesses of 100 to 250 nm deposited at 300, 450 and 750°C. Films were deposited using $\text{HfCl}_4\text{-H}_2\text{O}$ chemistry routes, H_2O partial pressure of 8 Pa and carrier gas flow rate of 2.6 m/s.

4.5. Optical properties of HfO_2

It is known that refractive index is related to the density of a film material [294]. Therefore in addition to refractive index, the density as a function of T_G was studied in this work (Figure 36). At the temperatures up to 500°C, the refractive index clearly correlated to the density of HfO_2 films. Transition from amorphous phase to the polycrystalline one caused a significant increase of both parameters (Figure 36). In our predominantly amorphous films ($T_G = 225^\circ\text{C}$), densities of 8.8 to 9.1 g/cm^3 upon different process parameter were obtained. These value are slightly higher than the theoretical value of 8,6 g/cm^3 calculated for amorphous phase [298]. This difference is in good agreement with the result that our films contained some amount crystalline phases (Figure 26, III). The refractive index values of 1.98–2.01 obtained in our experiments were well comparable to those reported for amorphous HfO_2 films earlier [155].

With the increase of T_G from 500 to 750°C, the refractive index of the films deposited in the $\text{HfCl}_4\text{-H}_2\text{O}$ process markedly decreased while no changes were observed in the density. At these temperatures, the sizes of randomly oriented crystallites (Figure 34) [III] as well as the surface roughness (Figure 33(a)) markedly increased with deposition temperature. Such structure can cause light scattering not only at the rough surface but also inside a film due to the grain boundary formation and corresponding inhomogeneity of the film material.

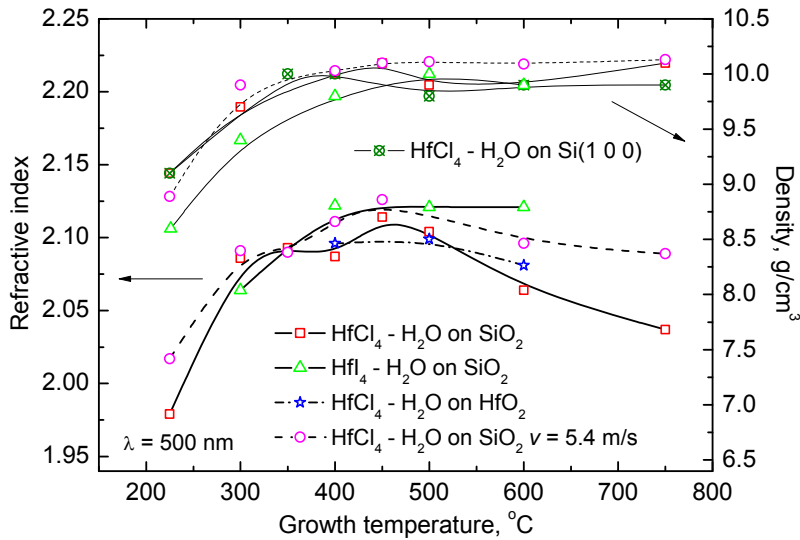


Figure 36. Effect of deposition temperature on density calculated from XRR data for HfO₂ films deposited on Si(1 0 0) and SiO₂ and on HfO₂ buffer layer, and on refractive index determined for wavelengths of 500 nm from transmission spectra of HfO₂ films deposited on SiO₂ substrates. Films were deposited at $p_w = 8$ Pa.

Higher refractive index of films deposited in the HfI₄-H₂O process at 600°C can be explained by higher uniformity of these films compared with those deposited in chloride-based process. This difference is not surprising because one can obtain smoother surfaces and more homogeneous material for the films deposited in the HfI₄-based processes due to the uniform nucleation in the initial growth stage [I,II]. A significant influence of the film structure on the refractive index has been noted also in several earlier reports [216,295,296]. Similarly to our studies demonstrating that the highest refractive indices can be obtained with textured films of (001) orientation (Figure 36), Ni et al [155] have shown refractive index increase with texture development in polycrystalline film. Structure formation is closely related to the film composition i.e. concentration of impurities that remain in the films especially at lower temperature. Thus, high residual chlorine and hydrogen concentration may lead in lower densities and refractive indices in these films. Indeed, higher water dose reduced concentration of halogen residues and stimulated crystallization which resulted in an increase of the refractive index too [III].

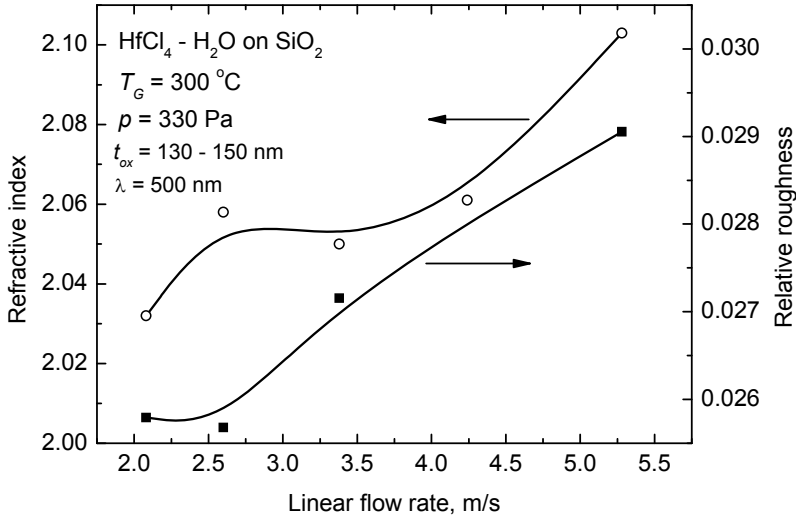


Figure 37. Refractive index and relative roughness as a function of carrier gas linear flow rate. Refractive index was determined for a wavelength of 500 nm from transmission spectra of HfO_2 films deposited on SiO_2 substrates. Films were deposited at $p_w = 8$ Pa.

Similar effect can be seen when higher carrier gas flow rate is used (Figure 37). Simultaneous increase in refractive index and relative roughness correlate with the improvement in structure development and decrease in the concentration of residues inside the film. Besides, higher flow rate enhances texture development [IV], which was already mentioned as a factor causing increase of refractive index and surface RMS roughness.

Usually a polycrystalline film has a higher extinction coefficient than an amorphous one does. This is mainly because of the loss of light by random reflections at the rough surface of the polycrystalline sample and at the interfaces between crystallites i.e. at grain boundaries. In that sense, one can conclude that in our films, the surface roughness as well as crystallite sizes influenced the scattering losses. As can be seen, this influence clearly appeared with increasing film thickness and with increasing deposition temperature. In both cases, one can see that the greater the sizes of surface features and crystallites inside the films, the higher the level of optical losses. For comparison, relatively low values of the extinction coefficient were determined for amorphous films deposited at 180–225°C. In the case of films deposited at 225°C, one can also see a marked increase of the extinction coefficient with the increase of film thickness from 100 to 160 nm. In this thickness range, growth of crystallites in predominantly amorphous matrix became significant although no remarkable surface roughening could be observed (Figure 31) [III]. In the case of films grown at higher temperatures, one can note that, due to the increase of the carrier gas

flow, optical losses are pretty much suppressed through improved structure. At lower deposition temperatures, however, the increase of the carrier gas flow results in deposition of film with stronger absorption, most probably because of increased surface roughness of these films (Figure 33 (a)). Hence, in our measurements, the extinction coefficient determined from the transmission spectra of the films included contribution from the absorption of light in the film material as well as from the scattering of light caused by the surface roughness and material inhomogeneity [293]. As demonstrated, the refractive index can be optimized and optical losses can be reduced by appropriate choice of the precursor system, deposition temperature as well as carrier gas flow parameters used in the ALD process.

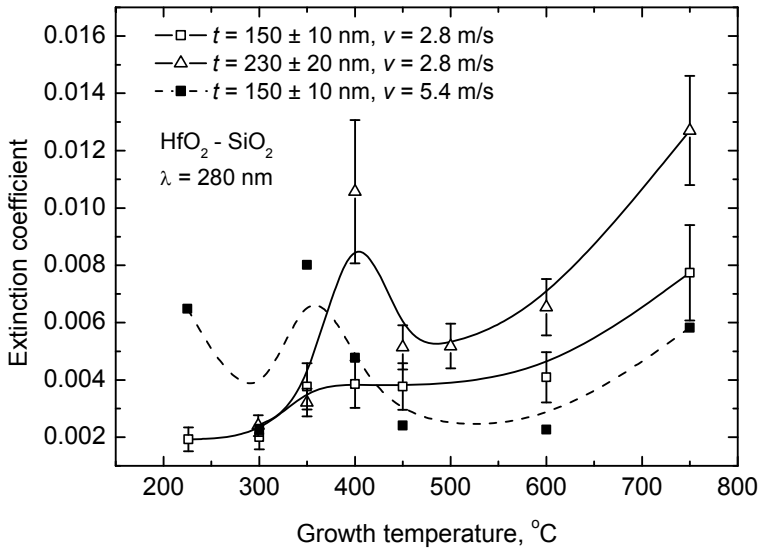


Figure 38. Extinction coefficient as a function of growth temperature for films with different thicknesses. Films were deposited at $p_w = 8$ Pa and carrier gas flow rates shown on the graph.

5. SUMMARY AND CONCLUSIONS

In this study, properties of HfO_2 thin films deposited in a wide substrate temperature range of 180–750°C were investigated as a function of ALD process parameters. For the chloride-based process, our studies revealed marked influence of the substrate temperature as well as film thickness on the growth rate on both, silicon and fused silica substrates. Non-linear dependence of the film thickness on the number of ALD cycles applied was observed in the case of relatively thick films. The studies performed allow one to conclude that this effect was related to crystallization processes, development of preferential orientation and increase of the surface roughness.

It was found that the reactivity of metal precursors towards the silicon substrate significantly depended on temperature. At high substrate temperatures non-uniform three-dimensional nucleation with easily detectable growth delays was observed. Incubation periods before steady state growth emerged in chloride-based process from growth temperatures exceeding 400°C and became longer at higher temperatures. At temperatures up to 300°C, the chloride-based process allowed uniform nucleation and smooth two-dimensional growth in our experiments. Differently from the chloride-based process, $\text{HfI}_4\text{-H}_2\text{O}$ and $\text{HfI}_4\text{-O}_2$ processes resulted in relatively uniform nucleation and initialization of film growth without marked incubation periods also at substrate temperatures up to 600°C.

It was demonstrated that the growth rate and structure of films as well as concentration of residues in the films depended on the linear flow rate and pressure of carrier gas as well. Higher carrier gas flow rates resulted in a markedly lower growth rate but also lower concentration of residues in the films. The effect was obviously related to the influence of carrier gas flow parameters on the adsorption and desorption processes, composition of the adsorbate layer and mass exchange between the surface layer and gas phase.

As expected, crystallization processes caused densification of HfO_2 films with increasing deposition temperature and film thickness. Most significant changes in the material density were observed at deposition temperatures up to 300°C. With the further increase of the deposition temperature to 750°C, no significant density changes were observed. By contrast, the refractive index of films deposited from HfCl_4 and H_2O that increased together with density at lower temperatures, decreased with the increase of deposition temperature from 500 to 750°C. Thus, the highest refractive index values i.e. the highest optical density was obtained for the films with most developed texture, whereas for these films, the highest values of RMS roughness were also recorded. Increase of carrier gas flow rate resulted in some increase of refractive index in predominantly amorphous films deposited at lower temperatures. Simultaneous increase in the surface roughness indicated that higher refractive index values were evidently due to more preferential initiation of crystallization processes at higher carrier gas flow rates.

Optical losses studied were due to the absorption of light in the film material as well as scattering caused by the surface roughness and structural inhomogeneity inside the films. The highest values of optical losses were determined for the films with most developed texture deposited at 400–450°C and for the films with the greatest grain sizes and high surface roughness obtained at highest deposition temperature used i.e. at 750°C. Expectedly, relatively low values of the extinction coefficient were determined for amorphous films. At higher deposition temperatures, somewhat lower optical losses were obtained for the films deposited at higher carrier gas flow rates.

SUMMARY IN ESTONIAN

Hafniumdioksiidi aatomkihtsadestamine – nukleatsioon, kasv, ja struktuuri muutused kiledes

Käesolev väitekiri hõlmab tehnoloogiliselt tähtsa kilematerjali, hafniumdioksiidi (HfO_2), aatomkihtsadestamise ja omaduste uurimist sõltuvalt sadestusprotsessi parameetritest. Uurimistöös kasutatud lähteainete kombinatsioonid ($\text{HfCl}_4\text{-H}_2\text{O}$, $\text{HfI}_4\text{-H}_2\text{O}$ ja $\text{HfI}_4\text{-O}_2$) ning lai sadestustemperatuuride ($180\text{--}750^\circ\text{C}$) ja kilepaksuste vahemik ($0\text{--}320\text{ nm}$) võimaldas uurida HfO_2 kasvukiiruse sõltuvust kile paksusest, kristallisatsioonist, tekstuurst, kile pinnakaredusest ja alusmaterjalist.

Töös selgitati välja, et kõrgetel temperatuuridel on HfO_2 kasv ränialustele kloriidil põhinevas protsessis oma algfaasis äärmiselt ebahütlane ja kolme-dimensionaalne. Aeglasem kasv kile moodustumise algfaasis oli selgesti nähtav kasvutemperatuuridel, mis ületasid 400°C , ning selle mõju tugevnes temperatuuri tõusuga. Eelistatult kahe-dimensionaalne kasv ja tunduvalt ühtlasema paksusega HfO_2 kiled saadi sadestustemperatuuridel kuni 300°C . Erinevalt kloriidil põhinevast protsessist, võimaldasid töös kasutatud $\text{HfI}_4\text{-H}_2\text{O}$ ja $\text{HfI}_4\text{-O}_2$ lähteainete kombinatsioonid sadestada ühtlase paksusega kilesid juba kasvu algfaasis temperatuuridel kuni 600°C .

Kandegaasi voolu kiirus ja rõhk kasvukambris mõjutasid kasvukiirust, kile struktuuri ja puhtust. Selgus, et suurem kandegaasivoog põhjustas väiksema kasvukiiruse, kuid samas võimaldas kilest efektiivsemalt eemaldada jääkprodukte.

Ootuspäraselt sõltus HfO_2 tihedus kristallisatsiooniprotsessidest, mis avaldusid kasvutemperatuuri tõusu ja kile paksuse kasvuga. Suurimad muutused toimusid amorfse faasi üleminekul kristalliliseks (monokliinseks) faasiks temperatuuridel kuni 300°C . Edasine temperatuuri tõus kile tihedust oluliselt ei mõjutanud. Kuni temperatuurideni 500°C järgisid murdumisnäitaja muutused tiheduse muutusi, kuid kasvutemperatuuri edasisel tõusul 750°C -ni hakkas murdumisnäitaja erinevalt tihedusest vähenema. Kõrgeimad murdumisnäitaja väärtused saadi kiledel, mis omasid kõige tugevamat kristallitide eelisorientatsiooni ehk tekstuuri. Madalamatel kasvutemperatuuridel põhjustas suurem kandegaasi voolukiirus samaaegse murdumisnäitaja ja kareduse suurenemise, mis on tõenäoliselt tingitud efektiivsemast kristallisatsioonist.

Optiliste omaduste uuringustest selgus, et optilised kaod kilematerjalist on tingitud valguse neeldumisest ning hajumisest kiles, kusjuures viimane sõltub nii pinnakaredusest kui ka struktuuri ebahütlusest kile sees. Leiti, et suurimad kaod esinevad kiledes, millel on suur pinnakaredus ja tugev tekstuur või milles on tekkinud suuremad kristallidid. Suhteliselt väikesed olid optilised kaod siledates amorfsetes kiledes, mis olid valmistatud madalamatel temperatuuridel. Optilisi kadusid kõrgematel temperatuuridel valmistatud kiledes oli võimalik vähendada kasutades kilede sadestamisel suuremaid kandegaasi voolu kiiruseid.

ACKNOWLEDGEMENTS

I wish to thank my supervisors Prof. Jaan Aarik and Prof. Väino Sammelselg for guiding me during the years that were needed to complete this thesis. I appreciate their patience with me.

All co-authors are thanked for their commitment in the publications. My special thanks belong to Dr. Hugo Mändar, Dr. Arvo Kikas, Dr. Teet Uustare, Dr. Aarne Kasikov, Ms. Jelena Asari and Mr. Peeter Ritslaid without whom the comprehensive characterization of the materials would not have been possible. I also wish to acknowledge the help and assistance of Dr. Aleks Aidla and Alma-Asta Kiisler in the growth experiments.

I am grateful to all my colleagues in the Laboratory of Thin-Film Technology for providing friendly and fruitful working atmosphere.

I am thankful for my family for their patience during my PhD studies.

The study has been supported by the Estonian Science Foundation (grant no. 5032, 5861, 6651, 7845, 8666, Eurocores/Eurographene programme), European Social Fund (grant no. MTT1), Estonian Ministry of Education and Research (targeted projects SF0180042s07, SF0382149s02 and SF0180046s07) and Graduate School “Functional Materials and Processes”.

REFERENCES

1. S.-Y. Oh, C.-G. Ahn, J.-H. Yang, W.-J. Cho, M.-G. Jang, *Microelec. Eng.*, 85 (2008) 1206.
2. A. Tsormpatzoglou, D.H. Tassis, C.A. Dimitriadis, M. Mouis, G. Ghibaud, N. Collaert, *Semicond. Sci. Technol.*, 24 (2009) 125001.
3. E. Gerritsen, N. Emonet, C. Caillat, N. Jourdan, M. Piazza, D. Fraboulet, B. Boeck, A. Berthelot, S. Smith, P. Mazoyer, *Solid-State Elect.*, 49 (2005) 1767.
4. J. G. Fossum, Z. Zhou, L. Mathew, B.-Y. Nguyen, *Solid-State Elect.*, 54 (2010) 86.
5. W. Rösner, E. Landgraf, J. Kretz, L. Dreeskornfeld, H. Schäfer, M. Städele, T. Schulz, F. Hofmann, R.J. Luyken, M. Specht, J. Hartwich, W. Pamler, L. Risch, *Solid-State Elect.*, 48 (2004) 1819.
6. K. Kim, S.Y. Lee, *Microelec. Eng.*, 84 (2007) 1976.
7. T. Suntola, *Thin Solid Films*, 216 (1992) 84.
8. M. Ritala, M. Leskelä, in *Handbook of Thin Film Materials*, Vol 1, Nalwa, H.S. (Ed.), Academic Press, San Diego, (2001) 103.
9. T. Suntola, J. Antson, A. Pakkala, S. Lindfors, *SID 80 Digest* 11 (1980) 108.
10. J. Robertson, *Rep. Prog. Phys.*, 69 (2006) 327.
11. G.D. Wilk, R.M. Wallace, J.M. Anthony, *J. Appl. Phys.*, 89 (2001) 5243.
12. M.T. Bohr, R.S. Chau, T. Ghani, and K. Mistry, *IEEE Spectrum*, 44 (2007) 29.
13. C. Auth, M. Buehler, A. Cappellani, C. Choi, G. Ding, W. Han, S. Joshi, B. McIntyre, M. Prince, P. Ranade, J. Sandford, C. Thomas, *Intel Tech. J.*, 12 (2008).
14. L. Niinistö, J. Päiväsäari, J. Niinistö, M. Putkonen, M. Nieminen, *Phys. Stat. Sol., A* 201 (2004) 1443.
15. H.B. Park, M. Cho, J. Park, S.W. Lee, H.-K. Kang, J.-C. Lee, S.-J. Oh, *J. Appl. Phys.*, 94 (2003) 3641.
16. S. Spiga, C. Wiemer, G. Tallarida, G. Scarel, S. Ferrari, G. Seguini, M. Fanciulli, *Appl. Phys. Lett.*, 87 (2005) 112904.
17. H. Iwai, S. Ohmi, *Microelec. Rel.*, 42 (2002) 465.
18. H. Wong, H. Iwai, *Microelec. Eng.*, 83 (2006) 1867.
19. S.E. Thompson, S. Parthasarathy, *Mat. Tod.*, 9 (2006) 20.
20. R.L. Puurunen, *J. Appl. Phys.*, 97 (2005) 121301.
21. S.M. George, *Chem. Rev.*, 110 (2010) 111.
22. H. Kim, H.-B.-R. Lee, W.-J. Maeng, *Thin Solid Films*, 517 (2009) 2563.
23. J. Niinistö, M. Putkonen, L. Niinistö, S. L. Stoll, K. Kukli, T. Sajavaara, M. Ritala, M. Leskelä, *J. Mater. Chem.*, 15 (2005) 2271.
24. J. Niinistö, M. Mäntymäki, K. Kukli, L. Costelle, E. Puukilainen, M. Ritala, M. Leskelä, *J. Cryst. Growth*, 312 (2010) 245.
25. J.S. Kilby, *United States Patent 3,138,745* (1959).
26. D.L. Critchlow, *IEEE Proc.*, 87 (1999) 659.
27. G.E. Moore, *Electronics*, 38 (1965) 114.
28. S.-H. Lo, D.A. Buchanan, Y. Taur, *IBM J. Res. Develop.*, 43 (1999) 32.
29. N. Yang, W.K. Henson, J.R. Hauser, J.J. Wortman, *IEEE Trans. Elect. Dev.*, 46 (1999) 1464.
30. D.A. Buchanan, *IBM J. Res. Develop.*, 43 (1999) 245.

31. R. Degraeve, G. Groeseneken, R. Bellens, J.L. Ogier, M. Depas, P.J. Roussel, H.E. Maes, *IEEE Trans. Elect. Dev.*, 45 (1998) 904.
32. M. Jeong, V. Narayanan, D. Singh, A. Topol, V. Chan, Z. Ren, *Mat. tod.*, 9 (2006) 26.
33. A. Jakubowski, L. Lukasiak, *Mat. Sci.-Pol.*, 26 (2008) 5.
34. J. Robertson, *Rep. Prog. Phys.*, 69 (2006) 327.
35. E. Ghiraldelli, C. Pelosi, E. Gombia, G. Chiavarotti, L. Vanzetti, *Thin Solid Films*, 517 (2008) 434.
36. J. Aarik, A. Kasikov, M. Kirm, S. Lange, T. Uustare, H. Mändar, *Proc. of SPIE*, 5946 (2004) 594601.
37. R.H. French, *J. Amer. Ceram. Soc.*, 73 (1990) 477.
38. M.-H. Tang, Y.-C. Zhou, X.-J. Zheng, Z. Yan, C.-P. Cheng, Z. Ye, Z.-S. Hu, *Trans. Nonferrous Met. Soc. China*, 16 (2006) 163.
39. X.J. Wang, L.D. Zhang, J.P. Zhang, G. He, M. Liu, L.Q. Zhu, *Mat. Lett.*, 62 (2008) 4235.
40. W.H. Chang, P. Chang, W.C. Lee, T.Y. Lai, J. Kwo, C.-H. Hsu, J.M. Hong, M. Hong, *J. Cryst. Growth*, 323 (2011) 107.
41. G.D. Wilk, R.M. Wallace, J.M. Anthony, *J. Appl. Phys.*, 89 (2001) 5243.
42. C. Chaneliere, S. Four, J.L. Autran, R.A.B. Devine, *Electrochem. Sol. State Lett.*, 2 (1999) 291.
43. T. Busani, R.A.B. Devine, *J. Appl. Phys.*, 98 (2005) 044102.
44. P.A. Murawala, M. Sawai, T. Tatsuta, O. Tsuji, S. Fujita, S. Fujita, *Jpn. J. Appl. Phys.*, 32 (1993) 368.
45. J.-Y. Zhang, I.W. Boyd, *Appl. Phys.*, A 70 (2000) 657.
46. M. Kadoshima, M. Hiratani, Y. Shimamoto, K. Torii, H. Miki, S. Kimura, T. Nabatame, *Thin Solid Films*, 424 (2003) 224.
47. W.D. Kim, G.W. Hwang, O.S. Kwon, S.K. Kim, M. Cho, D.S. Jeong, S.W. Lee, M.H. Seo, C.S. Hwang, Y.-S. Min, Y.J. Cho, *J. Electrochem. Soc.*, 152 (2005) C552.
48. J. Aarik, A. Aidla, H. Mändar, T. Uustare, M. Schuisky, A. Hårsta, *J. Cryst. Growth*, 242 (2002) 189.
49. B. Hudec, K. Husekova, E. Dobrocka, T. Lalinsky, J. Aarik, A. Aidla and K. Fröhlich, *IOP Conf. Series: Mat. Sci. Eng.*, 8 (2010) 012024.
50. K. Fröhlich, J. Aarik, M. Ľapajna, A. Rosová, A. Aidla, E. Dobročka and K. Hušková, *J. Vac. Sci. Technol.*, B27 (2009) 266.
51. S.K. Kim, W.-D. Kim, K.-M. Kim, C.S. Hwang, J. Jeong, *Appl. Phys. Lett.*, 85 (2004) 4112.
52. S.K. Kim, G.W. Hwang, W.-D. Kim, C.S. Hwang, *Electrochem. Sol.-State Lett.*, 9 (2006) F5.
53. W.D. Kim, G.W. Hwang, O.S. Kwon, S.K. Kim, M. Cho, D.S. Jeong, S.W. Lee, M.H. Seo, C.S. Hwang, Y.-S. Min, Y.J. Cho, *Electrochem. Sol.-State Lett.*, 8 (2005) F59.
54. M.E. Tobar, J. Krupka, E.N. Ivanov, R.A. Woode, *J. Appl. Phys.*, 83 (1998) 1604.
55. N. Klein, C. Zuccaro, U. Dähne, H. Schulz, N. Tellmann, R. Kutzner, A.G. Zaitsev, R. Wördenweber, *J. Appl. Phys.*, 78 (1995) 6683.
56. J. Pascual, J. Camassel, H. Mathieu, *Phys. Rev. B*, 18 (1978) 5606.
57. H. Tang, K. Prasad, R. Sanjinès, P.E. Schmid, F. Lèvy, *J. Appl. Phys.*, 75 (1994) 2042.

58. P.D. Kirsch, C.S. Kang, J. Lozano, J.C. Lee, J.G. Ekerdt, *J. Appl. Phys.*, 91 (2002) 4353.
59. Y.-S. Lin, R. Puthenkovilakam, J.P. Chang, *Appl. Phys. Lett.*, 81 (2002) 2041.
60. W.J. Zhu, T. Tamagawa, M. Gibson, T. Furukawa, T.P. Ma, *IEEE Elect. Dev. Lett.*, 23 (2002) 649.
61. H. Kato, T. Nango, T. Miyagawa, T. Katagiri, K.S. Seol, Y. Ohki, *J. Appl. Phys.*, 92 (2002) 1106.
62. V.V. Afanas'ev, A. Stesmans, F. Chen, X. Shi, S.A. Campbell, *Appl. Phys. Lett.*, 81 (2002) 1053.
63. V. Gritsenko, D. Gritsenko, S. Shaimeev, V. Aliev, K. Nasyrov, S. Erenburg, V. Tapilin, H. Wong, M.C. Poon, J.H. Lee, J.-W. Lee, C.W. Kim, *Microelect. Eng.*, 81 (2005) 524.
64. M. Modreanu, P. K. Hurley, B. J. O'Sullivan, B. O'Looney, J.-P. Senateur, H. Rousell, F. Rousell, M. Audier, C. Dubourdiou, I. W. Boyd Q. Fang, T. L. Leedham, S. A. Rushworth, A. C. Jones, H. O. Davies, and C. Jimenez, *Proc. SPIE*, 4876 (2003) 1236.
65. N. Ikarashi, K. Manabe, *J. Appl. Phys.*, 94 (2003) 480.
66. M. Seo, S.K. Kim, J.H. Han, C.S. Hwang, *Chem. Mater.*, 22 (2010) 4419.
67. R. Puthenkovilakam, J.P. Chang, *J. Appl. Phys.*, 96 (2004) 2701.
68. M. Balog, M. Schieber, M. Michman, S. Patai, *Thin Solid Films*, 41 (1977) 247.
69. S. Sayan, T. Emge, and E. Garfunkel, Xinyuan Zhao, L. Wielunski, R. A. Bartynski, and David Vanderbilt J. S. Suehle, S. Suzer, M. Banaszak-Holl, *J. Appl. Phys.*, 96 (2004) 7485.
70. M.C. Cheynet, S. Pokrant, F.D. Tichelaar, J.-L. Rouvière, *J. Appl. Phys.*, 101 (2007) 054101.
71. J. Aarik, H. Mändar, M. Kirm, L. Pung, *Thin Solid Films*, 466 (2004) 41.
72. X. Zhang, H. Tu, X. Wang, Y. Xiong, M. Yang, L. Wang, J. Du, *J. Cryst. Growth*, 312 (2010) 2928.
73. S. Migita, Y. Watanabe, H. Ota, H. Ito, Y. Kamimuta, T. Nabatame, A. Toriumi, *VLSI Tech. Dig.*, (2008) 152.
74. J. Robertson, K. Xiong, S.J. Clark, *Thin Solid Films*, 496 (2006) 1.
75. J.P. Chang, Y.-S. Lin, *Appl. Phys. Lett.*, 79 (2001) 3666.
76. S. Sayan, N.V. Nguyen, J. Ehrstein, T. Emge, E. Garfunkel, M. Croft, X. Zhao, D. Vanderbilt, I. Levin, E.P. Gusev, H. Kim, P.J. McIntyre, *Appl. Phys. Lett.*, 86 (2005) 152902.
77. S. Miyazaki, *J. Vac. Sci. Technol.*, B 19 (2001) 2212.
78. Y. Zhou, N. Kojima, K. Sasaki, *J. Phys. D: Appl. Phys.*, 41 (2008) 175414.
79. Y. Zhou, N. Inosaka, K. Sasaki, M. Kumeda, *Jpn. J. Appl. Phys.*, 48 (2009) 060208.
80. J. Aarik, H. Mändar, M. Kirm, *Proc. Estonian Acad. Sci. Phys. Math.*, 52 (2003) 289.
81. M. Balog, M. Schieber, M. Michman, S. Patai, *Thin Solid Films*, 47 (1977) 109.
82. S. Monaghan, K. Cherkaoui, É. O'Connor, V. Djara, P.K. Hurley, L. Oberbeck, E. Tois, L. Wilde, S. Teichert, *IEEE electron device letters*, 30 (2009) 219.
83. N. Konofaos, E. K. Evangelou, *Semicond. Sci. Technol.* 18 (2003) 56.
84. C.H. Chen, Y.K. Fang, C.W. Yang, S.F. Ting, Y.S. Tsair, M.F. Wang, S.C. Chen, C.H. Yu, M.S. Liang, *Sol.-State Elect.*, 45 (2001) 461.
85. K. Eriguchi, Y. Harada, M. Niwa, *IEDM Tech. Digest*, (1999) 323.

86. Y.C. YeO, Q. Lu, W.C. Lee, T.J. King, C. Hu, X. Wang, X. Guo, T.P. Ma, *IEEE Elect. Dev. Lett.*, 21 (2000) 540.
87. J.M. Rafi, E. Simoen, A. Mercha, N. Collaert, K. Hayama, F. Campabadal, C. Claeys, *Sol.-State Elect.*, 51 (2007) 1201.
88. T. Schram, L.-A° Ragnarsson, G. Lujan, W. Deweerd, J. Chen, W. Tsai, K. Henson, R.J.P. Lander, J.C. Hooker, J. Vertommen f, K. De Meyer, S. De Gendt, M. Heyns, *Microelect. Reli.*, 45 (2005) 779.
89. Y.Y Lebedinskii, A.V. Zenkevich, *Microelect. Rel.*, 47 (2007) 649.
90. Makoto Yoshimi, *Sol.-State Elect.*, 46 (2002) 951.
91. Lijuan Huang, Jack O. Chu, S. A. Goma, C. P. D’Emic, Steven J. Koester, Donald F. Canaperi, Patricia M. Mooney, S. A. Cordes, James L. Speidell, R. M. Anderson, and H.-S. Philip Wong, *IEEE Elect. Dev.*, 49 (2002) 1566.
92. T. Skotnicki, J.A. Hutchby, T.-J. King, H.-S.P. Wong, F. Boeuf, *IEEE Circ. Dev. Mag.*, (2005) 16.
93. H. Lu, W.-Y. Lu, Y. Taur, *Semicond. Sci. Technol.*, 23 (2008) 015006.
94. T. Tanaka, K. Tomioka, S. Hara, J. Motohisa, E. Sano, T. Fukui, *Appl. Phys. Exp.*, 3 (2010) 025003.
95. J.P. Colinge, *Microelect. Eng.*, 84 (2007) 2071.
96. A. Javey, J. Guo, D.B. Farmer, Q. Wang, D. Wang, R.G. Gordon, M. Lundstrom, H. Dai, *Nan. Lett.*, 4 (2004) 447.
97. I. Martin-Fernandez, M. Sansa, M.J. Esplandiu, E. Lora-Tamayo, F. Perez-Murano, P. Godignon, *Microelect. Eng.*, 87 (2010) 1554.
98. B.H. Lee, J. Oh, H.H. Tseng, R. Jammy, H. Huff, *Mat. Tod.*, 9 (2006) 32.
99. V. Schmidt, H. Riel, S. Senz, S. Karg, W. Riess, U. Gçsele, *Smal.*, 2 (2006) 85.
100. D. Wang, Q. Wang, A. Javey, R. Tu, H. Da, H. Kim, P.C., *Appl. Phys. Lett.*, 83 (2003) 2432.
101. Y. Li, F. Qian, J. Xiang, C.M. Lieber, *Mat. Tod.*, 9 (2006) 18.
102. M.C. Lemme, T.J. Echtermeyer, M. Baus, B.N. Szafranek, J. Bolten, M. Schmidt, T. Wahlbrink, H. Kurz, *Sol.-State Elect.*, 52 (2008) 514.
103. F. Schwierz, *Nat. Nanotech.*, 5 (2010) 487.
104. Y.-C. Yeo, *Thin Solid Films*, 34 (2004) 462.
105. L. Nyns, L.-Å. Ragnarsson, L. Hall, A. Delabie, M. Heyns, S. Van Elshocht, C. Vinckier, P. Zimmerman, S. De Gendt, *J. Elect. Soc.*, 155 (2008) G9.
106. K. Kukli, J. Niinistö, A. Tamm, J. Lu, M. Ritala, M. Leskelä, M. Putkonen, L. Niinistö, F. Song, P. Williams, P. N. Heys, *Microelect. Eng.* 84 (2007) 2010.
107. K. Kukli, M. Ritala, M. Leskelä, J. Sundqvist, L. Oberbeck, J. Heitmann, U. Schröder, J. Aarik, A. Aidla, *Thin Solid Films*, 515 (2007) 6447.
108. K. Kukli, J. Niinistö, A. Tamm, M. Ritala, M. Leskelä, *J. Vac. Sci. Technol. B* 27 (2009) 226.
109. X. Liu, S. Ramanathan, A. Longdergan, A. Srivastava, E. Lee, T.E. Seidel, J.T. Barton, D. Pang, R.G. Gordon, *J. Elect. Soc.*, 152 (2005) G213.
110. J. Niinistö, K. Kukli, A. Tamm, M. Putkonen, C.L. Dezelah, L. Niinistö, J. Lu, F. Song, P. Williams, P.N. Heys, M. Ritala, M. Leskelä, *J. Mater. Chem.*, 18 (2008) 3385.
111. K. Tse, J. Robertson, *Mat. Sci. Semicond. Proc.*, 9 (2006) 964.
112. K. Kukli, J. Aarik, A. Aidla, T. Uustare, I. Jõgi, J. Lu, M. Tallarida, M. Kemell, A.-A. Kiisler, M. Ritala, M. Leskelä, *J. Cryst. Growth*, 312 (2010) 2025.
113. T. Aaltonen, M. Ritala, K. Arstila, J. Keinonen, M. Leskelä, *Chem. Vap. Dep.*, 10 (2004) 215.

114. S.K. Kim, S.Y. Lee, S.W. Lee, G.W. Hwang, C.S. Hwang, J.W. Lee, J. Jeong, *J. Elect. Soc.*, 154 (2007) D95.
115. J.H. Han, S.W. Lee, G.-J. Choi, S.Y. Lee, C.S. Hwang, C. Dussarrat, J. Gatineau, *Chem. Mater.*, 21 (2009) 207.
116. Y.K. Lu, W. Zhu, X.F. Chen, R. Gopalkrishnan, *Microelect. Eng.*, 83 (2006) 371.
117. T. Nabatame, K Segawa, M. Kadoshima, H. Takaba, K. Iwamoto, S. Kimura, Y. Nunoshige, H. Satake, T. Ohishi, A. Toriumi, *Mat. Sci. Semicond. Proc.*, 9 (2006) 975.
118. J.Y. Son, W.J. Maeng, Woo-Hee Kim, Y.H. Shin, Hyungjun Kim, *Thin Solid Films*, 517 (2009) 3892.
119. M. Ľapajna, P. Pisečny, R. Lupták, K. Hušekova, K. Fröhlich, L. Harmatha, J.C. Hooker, F. Roozeboom, J. Jergel, *Mat. Sci. Semicond. Proc.* 7 (2004) 271.
120. K. Kukli, T. Aaltonen, J. Aarik, J. Lu, M. Ritala, S. Ferrari, A. Hårsta, M. Leskelä, *J. Electrochem. Soc.*, 152 (2005) F75-F82.
121. A. Kosola, M. Putkonen, L.-S. Johansson, L. Niinistö, *Appl. Surf. Sci.*, 211 (2003) 102.
122. S. Clima, G. Pourtois, N. Menou, M. Popovici, A. Rothschild, B. Kaczer, S. Van Elshocht, X.P. Wang, J. Swerts, D. Pierreux, S. De Gendt, D.J. Wouters, J.A. Kittl, *Microelect. Eng.*, 86 (2009) 1936.
123. J.A. Kittl, K. Opsomer, M. Popovici, N. Menou, B. Kaczer, X.P. Wang, C. Adelman, M.A. Pawlak, K. Tomida, A. Rothschild, B. Govoreanu, R. Degraeve, M. Schaekers, M. Zahid, A. Delabie, J. Meersschant, W. Polspoel, S. Clima, G. Pourtois, W. Knaepen, C. Detavernier, V.V. Afanas'ev, T. Blomberg, D. Pierreux, J. Swerts, P. Fischer, J.W. Maes, D. Manger, W. Vandervorst, T. Conard, A. Franquet, P. Favia, H. Bender, B. Brijs, S. Van Elshocht, M. Jurczak, J. Van Houdt, D.J. Wouters, *Microelect. Eng.*, 86 (2009) 1789.
124. G. Molas, M. Bocquet, E. Vianello, L. Perniola, H. Grampeix, J.P. Colonna, L. Masarotto, F. Martin, P. Brianceau, M. Gély, C. Bongiorno, S. Lombardo, G. Pananakakis, G. Ghibaudo, B. De Salvo, *Microelect. Eng.*, 86 (2009) 1796.
125. S. Maikap, P.-J. Tzeng, T.-Y. Wang, H.-Y. Lee, C.-H. Lin, C.-C. Wang, L.-S. Lee, J.-R. Yang, M.-J. Tsai, *Jap. J. Appl. Phys.*, 46 (2007) 1803.
126. J. Robertson, *J. Vac. Sci. Tech.*, B 18 (2000) 1785.
127. S. Maikap, S.Z. Rahaman, T.C. Tien, *Nanotech.*, 19 (2008) 435202.
128. D.B. Farmer, R.G. Gordon, *J. Appl. Phys.*, 101 (2007) 124503.
129. P.H. Yeh, L.J. Chen, P.T. Liu, D.Y. Wang, T.C. Chang, *Electrochim. Act.*, 52 (2007) 2920.
130. T. Kauerauf, B. Govoreanu, R. Degraeve, G. Groeseneken, and H. Maes, *Sol.-State Elect.*, 49 (2005) 695.
131. L. Zhang, H. C. Jiang, C. Liu, J.W. Dong, P. Chow, *J. Phys. D: Appl. Phys.* 40 (2007) 3707.
132. Y. Chang, F. Ducroquet, E. Gautier, O. Renault, J. Legrand, J.F. Damlencourt, F. Martin, *Microelect. Eng.*, 72 (2004) 326.
133. E. Ghiraldelli, C. Pelosi, E. Gombia, G. Chiavarotti, L. Vanzetti, *Thin Solid Films*, 517 (2008) 434.
134. A.H. Heuer, *J. Eur. Cer. Soc.*, 28 (2008) 1495.
135. R. Katamreddy, R. Inman, G. Jursich, A. Soulet, C. Takoudis, *Appl. Phys. Lett.*, 89 (2006) 262906.
136. A. Rahtu (PhD thesis), 2002.

137. S.W. Whangbo, Y.K. Choi, K.B. Chung, H.K. Jang, C.N. Whang, *J. Vac. Sci. Technol.*, A 19 (2001) 410.
138. I. Jögi, K. Kukli, J. Aarik, A. Aidla, J. Lu, *Mat. Sci. Semicond. Proc.*, 9 (2006) 1084.
139. G.B. Alers, D.J. Werder, Y. Chabal, H.C. Lu, E.P. Gusev, E. Garfunkel, T. Gustafsson, R.S. Urdahl, *Appl. Phys. Lett.*, 73, (1998) 1517.
140. H. Ono, Y. Hosokawa, T. Ikarashi, K. Shinoda, N. Ikarashi, *J. Appl. Phys.*, 89 (2001) 995.
141. M. Gutowski, J. E. Jaffe, C.-L. Liu, M. Stoker, R. I. Hedge, R. S. Rai, P. J. Tobin, *Appl. Phys. Lett.*, 80 (2002) 1897.
142. Y.-S. Lin, R. Puthenkovilakam, J.P. Chang, *Appl. Phys. Lett.*, 81 (2002) 2041.
143. J. Zhu, Z.G. Liu, *Appl. Phys. A* 80, (2005) 1769.
144. Y. Lu, O. Bui, S. Hall, I.Z. Mitrovic, W. Davey, R.J. Potter, P.R. Chalker, *Microelect. Rel.* 47 (2007) 722.
145. P.K. Park, E.-S. Cha, S.-W. Kang, *Appl. Phys. Lett.*, 90 (2007) 232906.
146. M.-H. Cho, Y.S. Roh, C.N. Whang, K. Jeong, H.J. Choi, S.W. Nam, D.-H. Ko, J.H. Lee, N.I. Lee, K. Fujihara, *Appl. Phys. Lett.*, 81 (2002) 1071.
147. D. Ishikawa, S. Kamiyama, E. Kurosawa, T. Aoyama, Y. Nara, *Jpn. J. Appl. Phys.* 48 (2009) 04C004.
148. H. Kim, P.C. McIntyre, K.C. Saraswat, *Appl. Phys. Lett.*, 88 (2003) 106.
149. G. He, M.Liu, L.Q. Zhu, M.Chang, Q.Fang, L.D. Zhang, *Surf. Sci.*, 576 (2005) 67.
150. M.-H. Cho, Y. S. Roh, C. N. Whang, K. Jeong, S. W. Nahm, D.-H. Ko, J. H. Lee, N. I. Lee, and K. Fujihara, *Appl. Phys. Lett.*, 81 (2002) 3472.
151. E. P. Gusev, C. Cabral Jr., M. Copel, C. D'Emic, and M. Gribelyuk, *Microelect. Eng.*, 69 (2003) 145.
152. D. Triyoso, R. Liu, D. Roan, M. Ramon, N. V. Edwards, R. Gregory, D. Werho, J. Kulik, G. Tam, E. Irwin, X.-D. Wang, L. B. La, C. Hobbs, R. Garcia, J. Baker, B. E. White Jr., and P. Tobin, *J. Elect. Soc.*, 151 (2004) F220.
153. M. Quevedo-Lopez, M. El-Bouanani, S. Addepalli, J.L. Duggan, B.E. Gnade, R.M. Wallace, M.R. Visokay, M. Douglas, L. Colombo, *Appl. Phys. Lett.*, 79 (2001) 4192.
154. M. Quevedo-Lopez, M. El-Bouanani, B.E. Gnade, R.M. Wallace, M.R. Visokay, M. Douglas, M.J. Bevan, L. Colombo, *J. Appl. Phys.*, 92 (2002) 3540.
155. J. Ni, Z.-C. Li, Z.-J. Zhang, *Front. Mater. Sci. Chi.*, (2008) 381.
156. A. Waldorf, J. Dobrowolski, B. Sullivan, L. Plante, *Appl. Opt.* 32 (1993) 5583.
157. J. Khoshman, M. Kordesch, *Surf. Coat. Tech.* 201 (2006) 3530.
158. X.T. Zu, X.Q. Chen, W.G. Zheng, X.D. Jiang, X.D. Yuan, X.P. Li, X. Xiang, *Nucl. Instr. Meth. Phys. Res. B.* 266 (2008) 3195.
159. M. Alvisi, F. De Tomasi, M.R. Perrone, M.L. Protopapa, A. Rizzo, F. Sarto, S. Scaglione, *Thin Solid Films*, 396 (2001) 44.
160. P. Torchio, A. Gatto, M. Alvisi, G. Albrand, N. Kaiser, C. Amra, *Appl. Opt.* 41 (2002) 3256.
161. J. Yuan, L. Yuan, H. He, K. Yi, Z. Fan, J. Shao, *Appl. Surf. Sci.* 254 (2008) 4864.
162. M.L. Grilli, F. Menchini, A. Piegari, D. Alderighi, G. Toci, M. Vannini, *Thin Solid Films*, 517 (2009) 1731.
163. M. Fadel, O.A. Azim, O.A. Omer, R.R. Basily, *Appl. Phys. A: Mater. Sci. Proc.*, 66 (1998) 335.

164. R. R. Goncalves, G. Carturan, M. Montagna, M. Ferrari, L. Zampedri, S. Pelli, G. C. Righini, S. J.L. Ribeiro, Y. Messaddeq, *Opt. Mat.* 25 (2004) 131.
165. J. Yuan, H. Qi, Y. Zhao, Z. Fan, J. Shao, *Chin. Opt. Lett.*, 6 (2008) 223.
166. J. Wang, H.P. Li, R. Stevens, *J. Mater. Sci.* 27 (1992) 5397.
167. J.M. Léger, J. Haines, B. Blanzat, *J. Mater. Sci. Lett.* 13 (1994) 1688.
168. J.M. Léger, A. Atouf, P.E Tomaszewski, A.S. Pereira, *Phys. Rev. B* 48 (1993) 93.
169. S.M.A. Durrani, M.F. Al-Kuhaili, *Materials Chem. Phys.*, 109 (2008) 56.
170. A. Avila-García, M. García-Hipólito, *Sens. Actuators B*, 133 (2008) 302.
171. N. Selvakumar, H. C.Barshilia, K.S. Rajam, A.Biswas, *Sol. Energ. Mat. Sol. Cel.*, 94 (2010) 1412.
172. T. Suntola, J. Antson, 1977, US Patent No. 4 058 430.
173. M. Leskelä, M. Ritala, *J. Phys. IV, C-5* (1995) 937.
174. M. Leskelä, M. Kemell, K. Kukli, V. Pore, E. Santala, M. Ritala, J. Lu, *Mat. Sci. Eng., C* 27 (2007) 1504.
175. J. Aarik, A. Aidla, A.-A. Kiisler, T. Uustare, V. Sammelselg, *Thin Solid Films*, 340 (1999) 110.
176. R.L. Puurunen, *J. Appl. Phys.*, 95 (2004) 4777.
177. O. Sneh, Michelle A. Cameron, S.M. George, *Surf. Sci.*, 364 (1996) 61.
178. S. Haukka, A. Root, *J. Phys. Chem.*, 98 (1994) 1695.
179. S. Haukka, E.-L. Lakomaa, T. Suntola, *Appl. Surf. Sci.*, 82-3 (1994) 548.
180. A. Delabie, M. Caymax, B. Brijs, D. P. Brunco, T. Conard, E. Sleenckx, S. Van Elshocht, L.-Å. Ragnarsson, S. De Gendt, and M. M. Heyns, *J. Electrochem. Soc.*, 153 (2006) F180.
181. Y. Widjaja, and C.B. Musgrave, *J. Chem. Phys.*, 117 (2002) 1931.
182. M. Deminsky, A. Knizhnik, I. Belov, S. Umanskii, E. Rykova, A. Bagatur'yants, B. Potapkin, M. Stoker, A. Korkin, *Surf. Sci.*, 549 (2004) 67.
183. P.J. Stout, V. Adams, P.L.G. Ventzek, *J. Vac. Sci. Tech.*, B 24 (2006) 2372.
184. A.B. Mukhopadhyay, C.B. Musgrave, *Chem. Phys. Lett.*, 421 (2006) 215.
185. A.B. Mukhopadhyay, C.B. Musgrave, J.F. Sanz, *J. Americ. Chem. Soc.*, 130 (2008) 11996.
186. M. Ylilammi, *Thin Solid Films*, 279 (1996) 124.
187. M.L. Green, M.-Y. Ho, B. Busch, G.D. Wilk, T. Sorsch, T. Conard, B. Brijs, W. Vandervorst, P.I. Räisänen, D. Muller, M. Bude, J. Grazul, *J. Appl. Phys.* 92 (2002) 7168.
188. M.A. Alam, M.L. Green, *J. Appl. Phys.* 94 (2003) 3403.
189. J. Aarik, K. Kukli, A. Aidla, L. Pung, *Appl. Surf. Sci.*, 103 (1996) 331.
190. P.K. Park, J.-S. Roh, B.H. Choi, S.-W. Kang, *Electrochem. Sol.-State Lett.*, 9 (2006) F34.
191. S.-J. Park, W.-H. Kim, H.-B.-R. Lee, W.J. Maeng, H. Kim, *Microelect. Eng.* 85 (2008) 39.
192. J.A. Venables, G.D.T. Spiller, M. Hanbucken, *Rep. Prog. Phys.*, 47 (1984) 399.
193. J. A. Venables, *Cam. Univ. Press*, 2000.
194. R.L. Puurunen, *Chem. Vap. Dep.*, 10 (2004) 159.
195. R.L. Puurunen, W. Vandervorst, *J. Appl. Phys.*, 96 (2004) 7686.
196. K. Kukli, M. Ritala, M. Leskelä, T. Sajavaara, J. Keinonen, A.C. Jones, J.L. Roberts, *Chem. Mater.*, 15 (2003) 1722.
197. J. Niinistö, M. Putkonen, L. Niinistö, S.L. Stoll, K. Kukli, T. Sajavaara, M. Ritala, M. Leskelä, *J. Mater. Chem.*, 15 (2005) 2271.

198. M. Cho, R. Degraeve, G. Pourtois, A. Delabie, L.-Å. Ragnarsson, T. Kauerauf, G. Groeseneken, S. De Gendt, M. Heyns, C.S. Hwang, *IEEE Trans. El. Dev.*, 54 (2007) 752.
199. A. Soulet, L. Duquesne, G. Jursich, R. Inman, A. Misra, N. Blasco, C. Lachaud, Y. Marot, R. Prunier, M. Vautier, S. Anderson, P. Clancy, and M. Havlicek, *Semicond. Fabtech*, 27 (2005) 74
200. H. Kattelus, M. Ylilammi, J. Salmi, T.R. Aho, E. Nykänen, I. Suni, *Mat. Res. Soc. Symp. Proc.*, 284 (1993) 511.
201. M. Ritala, M. Leskelä, L. Niinistö, T. Prohaska, G. Friedbacher, M. Grasserbauer, *Thin Solid Films*, 250 (1994) 72.
202. J. Aarik, A. Aidla, H. Mändar, V. Sammelselg, T. Uustare, *J. Cryst. Growth*, 200 (2000) 105.
203. G. Scarel, C. Wiemer, S. Ferrari, G. Tallarida, M. Fanciulli, *Proc. Estonian Acad. Sci. Phys. Math.* 52 (2003) 308.
204. X. Yu, C. Zhu, H. Hu, A. Chin, M.F. Li, B.J. Cho, D.-L. Kwong, P.D. Foo, M.B. Yu, *IEEE Elect. Dev. Lett.* 24 (2003) 63.
205. M. Cho, J. Park, H.B. Park, C.S. Hwang, J. Jeong, K.S. Hyun, *Appl. Phys. Lett.* 81 (2002) 334.
206. K. Kukli, M. Ritala, T. Sajavaara, J. Keinonen, M. Leskelä, *Thin Solid Films*, 416 (2002) 72.
207. K. Kukli, M. Ritala, M. Leskelä, T. Sajavaara, J. Keinonen, D.C. Gilmer, R. Hedge, R. Rai, L. Prabhu, *J. Mater. Sci.: Mater. Elect.*, 14 (2003) 361.
208. R.G. Vitchev, J.J. Pireaux, T. Conard, H. Bender, J. Wolstenholme, C. Defranoux, *Appl. Surf. Sci.* 235 (2004) 21.
209. P.D. Kirsch, M.A. Quevedo-Lopez, H.-J. Li, Y. Senzaki, J.J. Peterson, S.C. Song, S.A. Krishnan, N. Moumen, J. Barnett, G. Bersuker, P.Y. Hung, B.H. Lee, T. Lafford, Q. Wang, D. Gay, J.G. Ekerdt, *J. Appl. Phys.*, 99 (2006) 023508.
210. R. Matero, A. Rahtu, M. Ritala, M. Leskelä, T. Sajavaara, *Thin Solid Films* 368 (2000) 1.
211. R. Kuse, M. Kundu, T. Yasuda, N. Miyata, A. Toriumi, *J. Appl. Phys.* 94 (2003) 6411.
212. K. Kukli, J. Aarik, M. Ritala, T. Uustare, T. Sajavaara, J. Lu, J. Sundqvist, A. Aidla, L. Pung, A. Hårsta, M. Leskelä, *J. Appl. Phys.*, 96 (2004) 5298.
213. J. Aarik, J. Sundqvist, A. Aidla, J. Lu, T. Sajavaara, K. Kukli, A. Hårsta, *Thin Solid Films*, 418 (2002) 69.
214. K. Kukli, M. Ritala, J. Sundqvist, J. Aarik, J. Lu, T. Sajavaara, M. Leskelä, A. Hårsta, *J. Appl. Phys.*, 92 (2002) 5698.
215. K. Kukli, M. Ritala, M. Leskelä, T. Sajavaara, J. Keinonen, *Chem. Vap. Dep.* 8 (2002) 199.
216. K. Kukli, T. Pilvi, M. Ritala, T. Sajavaara, J. Lu, M. Leskelä, *Thin Solid Films*, 491 (2005) 328.
217. S. Ferrari, G. Scarel, C. Wiemer, M. Fanciulli, *J. Appl. Phys.*, 92 (2002) 7675.
218. J.-J. Ganem, I. Trimaille, I.C. Vickridge, D. Blin, F. Martin, *Nucl. Inst. Meth. Phys. Res. B*, 219-220 (2004) 856.
219. N. Miyata, T. Nabatame, T. Horikawa, M. Ichikawa, A. Toriumi, *Appl. Phys. Lett.*, 82 (2003) 3880.
220. P.S. Lysaght, B. Foran, G. Bersuker, P.J. Chen, R.W. Murto, H.R. Huff, *Appl. Phys. Lett.* 82 (2003) 1266.

221. D. H. Triyoso, R. I. Hedge, J. Grant, P. Fejes, R. Liu, D. Roan, M. Ramon, D. Werho, R. Rai, L. B. La, J. Baker, C. Garza, T. Guenther, B. E. White Jr., and P. J. Tobin, *J. Vac. Sci. Tech.*, B 22 (2004) 2121.
222. M.L. Green, A.J. Allen, X. Li, J. Wang, J. Ilavsky, A. Delabie, R.L. Puurunen, B. Brijs, *Appl. Phys. Lett.*, 88 (2006) 032907.
223. L. Nyns, A. Delabie, M. Caymax, M.M. Heyns, S. Van Elshocht, C. Vinckier, S. De Gendt, *J. Electrochem. Soc.*, 155 (2008) G269.
224. H.S. Chang, H. Hwang, M.-H. Cho, D.W. Moon, *Appl. Phys. Lett.*, 86 (2005) 031906.
225. K.B. Chung, C.N. Whang, H.S. Chang, D.W. Moon, M.-H. Cho, *J. Vac. Sci. Tech.*, A 25 (2007) 141.
226. K. Kukli, M. Ritala, J. Lu, A. Hårsta, M. Leskelä, *J. Electrochem. Soc.*, 151, (2004) F189.
227. M.-T. Ho, Y. Wang, R.T. Brewer, L.S. Wielunski, Y.J. Chabal, N. Moumen, M. Boleslawski, *Appl. Phys. Lett.*, 87 (2005) 133103.
228. J. C. Hackley, T. Gougousi, and J. D. Demaree, *J. Appl. Phys.*, 102 (2007) 034101.
229. J.C. Hackley, J.D. Demaree, T. Gougousi, *J. Vac. Sci. Technol. A* 26 (2008) 1235.
230. M. Tallarida, K. Karavaev, D. Schmeisser, *J. Vac. Sci. Technol.*, B 27 (2009) 300.
231. A.B. Mukhopadhyay, J.F. Sanz, C.B. Musgrave, *Chem. Mater.*, 18 (2006) 3397.
232. H. Wong, K.L. Ng, N. Zhan, M.C. Poon, C. W. Kok, *J. Vac. Sci. Technol.*, B 22 (2004) 1094.
233. T. Ting-Ting, L. Zheng-Tang, L. Wen-Ting, Z. Wen-Hua, *Chin. Phys. Lett.*, 25 (2008) 3750.
234. P.F. Lee, J.Y. Dai, H.L.W. Chan, C.L. Choy, *Ceram. Internat.*, 30 (2004) 1267.
235. W.L. Scopel, A.J.R. da Silva, W. Orellana, A. Fazzio, *Appl. Phys. Lett.*, 84 (2004) 1492.
236. R.M.C de Almeida, I.J.R. Baumvol, *Surf. Sci. Rep.*, 49 (2003) 1.
237. U. Brossmann, R. Wurschum, U. Sodervall, H.E. Schaefer, *J. Appl. Phys.*, 85 (1999) 7646.
238. N. Miyata, M. Ichikawa, T. Nabatame, T. Horikawa, A. Toriumi, *Jpn. J. Appl. Phys. Vol. 42* (2003) L138.
239. N Miyata, *Appl. Phys. Lett.*, 89 (2006) 102903.
240. R. Jiang, Z. Li, *Semicond. Sci. Technol.* 24 (2009) 065006.
241. S. J. Wang, P.C. Lim, A.C.H. Huan, C.L. Liu, J.W. Chai, S.Y. Chow, J.S. Pan, Q. Li, C.K. Ong, *Appl. Phys. Lett.*, 82 (2003) 2047.
242. L. Wang, P.K. Chu, A. Anders, N.W. Cheung, *J. Appl. Phys.*, 104 (2008) 054117.
243. H. Takahashi, S. Toyoda, J. Okabayashi, H. Kumigashira, M. Oshima, Y. Sugita, G.L. Liu, Z. Liu, K. Usuda, *Appl. Phys. Lett.*, 87 (2005) 012903.
244. A. Zenkevich, Y. Lebedinskii, G. Scarel, M. Fanciulli, A. Baturin, N. Lubovin, *Microelect. Rel.* 47 (2007) 657.
245. J.-C. Lee, S.-J. Oh, M. Cho, C.S. Hwang, R. Jung, *Appl. Phys. Lett.* 84 (2005) 1305
246. A.A. Sokolov, E.O. Filatova, V.V. Afanas'ev, E.Y. Taracheva, M.M. Brzhezinskaya, A.A. Ovchinnikov, *J. Phys. D: Appl. Phys.* 42 (2009) 035308.
247. D.R.G. Mitchell, A. Aidla, J. Aarik, *Appl. Surf. Sci.* 253 (2006) 606.
248. O. Renault, D. Samour, J.-F. Damlecourt, *Appl. Phys. Lett.* 81 (2002) 3627.

249. M. Tallarida, K. Karavaev, D. Schmeisser, *J. Vac. Sci. Tech.*, B 27(1), 2009.
250. R.E. Hann, P.R. Suitch, J.L. Pentecost, *J. Am. Ceram. Soc.* 68 (1985) 285.
251. O. Ohtaka, T. Yamanaka, S. Kume, N. Hara, H. Asano, F. Izumi, *J. Am. Ceram. Soc.* 78 (1995) 233.
252. K. Kukli, M. Ritala, T. Pilvi, T. Aaltonen, J. Aarik, M. Lautala, M. Leskelä, *Mater. Sci and Eng.*, B 118 (2005) 112.
253. K. Kukli, J. Aarik, T. Uustare, J. Lu, M. Ritala, A. Aidla, L. Pung, A. Hårsta, M. Leskelä, A. Kikas, V. Sammelselg, *Thin Solid Films*, 479 (2005) 1.
254. J. Aarik, A. Aidla, H. Mändar, T. Uustare, K. Kukli, M. Schuisy, *Appl. Surf. Sci.* 173 (2001) 15.
255. D.M. Hausmann, R.G. Gordon, *J. Cryst. Growth*, 249 (2003) 251.
256. J. Niinistö, M. Putkonen, L. Niinistö, S.L. Stoll, K. Kukli, T. Sajavaara, M. Ritala, M. Leskelä, *J. Mater. Chem.*, 15 (2005) 2271.
257. A. Niilisk, J. Aarik, T. Uustare, H. Mändar, S. Tkachev, M. Manghnani, *Proc. of SPIE*, 5946 (2005) 59460E-1.
258. A. Navrotsky, *Geochem. Trans.*, 4 (2003) 34.
259. X. Zhao, D. Vanderbilt, *Phys. Rev. B*, 65 (2002) 233106.
260. K. Tomida, K. Kita, A. Toriumi, *Appl. Phys. Lett.*, 89 (2006) 142902.
261. K. Kita, K. Kyuno, A. Toriumi, *Appl. Phys. Lett.*, 86 (2005) 102906.
262. J. Niinistö, M. Mäntymäki, K. Kukli, L. Costelle, E. Puukilainen, M. Ritala, M. Leskelä, *J. Cryst. Growth*, 312 (2010) 245.
263. A Tamm, K Kukli, J Niinistö, J Lu, M Ritala, M Leskelä, *Mat. Sci. Eng.*, 8 (2010) 012022.
264. J. Aarik, A. Aidla, H. Mändar, V. Sammelselg, *J. Cryst. Growth*, 220 (2000) 531.
265. J. Aarik, J. Karlis, H. Mändar, T. Uustare, V. Sammelselg, *Appl. Surf. Sci.*, 181 (2001) 339.
266. M. Cassir, F. Coubin, C. Bernay, P. Vernoux, D. Lincot, *Appl. Surf. Sci.*, 193 (2002) 120.
267. A. Tarre, J. Aarik, H. Mändar, A. Niilisk, R. Pärna, R. Rammula, T. Uustare, A. Rosental, V. Sammelselg, *Appl. Surf. Sci.*, 254 (2008) 5149.
268. S.-W. Jeong, H.J. Lee, K.S. Kim, M.T. You, Y. Roh, T. Noguchi, W. Xianyu, J. Jung, *Thin Solid Films*, 515 (2006) 526.
269. J. Aarik, A. Aidla, H. Mändar, T. Uustare, V. Sammelselg, *Thin Solid Films*, 408 (2002) 97.
270. J. Aarik, A. Aidla, A. Jaek, M. Leskelä, L. Niinistö, *J. Mater. Chem.*, 4 (1994) 1239.
271. G. Sauerbrey, *Z. Phys.* 155 (1959) 206.
272. E. Benes, M. Gröschl, W. Burger, M. Schmid, A48 (1995) 1.
273. M.N. Rocklein, S.M. George, *Anal. Chem.*, 75 (2003) 4975.
274. A. Rahtu, M. Ritala, *Appl. Phys. Lett.*, 80 (2002) 521.
275. J. Aarik, A. Aidla, A. Jaek, M. Leskelä, L. Niinistö, *J. Mater. Chem.*, 4 (1994) 1239.
276. M. Laue, *Proc. Bavar. Acad. Sci.*, (1912) 363.
277. H. Mändar, J. Flesche, V. Mikli, T. Vajakas, *J. Appl. Crystallogr.* 32 (1999) 345.
278. S. Nishikawa and S. Kikuchi, *Nature*, 122 (1928) 726.
279. J.M. Van Hove, P.R. Pukite, P.I. Cohen, *J. Vac. Sci. Technol.*, B3 (1985) 563.
280. V. Sammelselg, J. Aarik, A. Aidla, A. Kasikov, E. Heikinheimo, M. Peussa, L. Niinistö, *J. Anal. At. Spectrom.*, 14 (1999) 523.

281. M. Schuisky, K. Kukli, J. Aarik, J. Lu, A. Härsta, *J. Cryst. Growth*, 235 (2002) 293.
282. S. Lehto, L. Niinistö, I. Yliruokanen, *Fresen. J. Anal. Chem.* 346 (1993) 608.
283. E. Chason, T.M. Mayer, *Crit. Rev. Sol. Stat. Mater. Sci.*, 22 (1997) 1.
284. A. Van der Lee, *Sol. Stat. Sci.*, 2 (2000) 257.
285. R. Swanepoel, *J. Phys. E* 16 (1983) 1214.
286. O. Renault, D. Samour, D. Rouchon, Ph. Holliger, A.-M. Papon, D. Blin, S. Marthon, *Thin Solid Films* 428 (2003) 190.
287. O. Renault, D. Samour, J.-F. Damlencourt, D. Blin, F. Martin, S. Marthon, N. T. Barrett, P. Besson, *Appl. Phys. Lett.*, 81 (2002) 3627.
288. <http://www.maxlab.lu.se/beamlines/bl31/> (05.05.2011)
289. U. Johansson (PhD thesis), 1997.
290. Park Scientific Instruments, *Users Guide to AutoProbe CP*, 1997.
291. S. Sayan, E. Garfunkel, S. Suzer, *Appl. Phys. Lett.*, 80 (2002) 2135.
292. K. Forsgren, A. Härsta, J. Aarik, A. Aidla, J. Westlinder, J. Olsson, *J. Electrochem. Soc.* 149 (2002) F139.
293. R. Swanepoel, *J. Phys. E: Sci. Instrum.* 17 (1984) 896
294. F.L. Martinez, M. Toledano-Luque, J.J. Gandia, *J. Phys. D App. Phys.*, 40 (2007) 5256.
295. J. Wang, R. L. Maier, H. Schreider, *Appl Opt.* 47 (2008) 189.
296. R. Chow, S. Falabella, G. E. Loomis, F. Rainer, C. J. Stolz, M. R. Kozlowski, *Appl. Opt.* 32 (1993) 5567.
297. D.H. Triyoso, R.I. Hegde, B.E. White Jr., P.J. Tobin, *J. Appl. Phys.* 97 (2005) 124107.
298. C. Kaneta, T. Yamasaki, *Micr. Eng.* 84 (2007) 2370–2373.

PUBLICATIONS

CURRICULUM VITAE

General data

Name and surname: Raul Rammula
Date and place of birth: 16.02.1981, Võru, Estonia
Citizenship: Estonian
Marital status: single, cohabiting
Contact: Institute of Physics, University of Tartu,
Riia 142, 51014, Tartu, Estonia
Telephone: +372 7 374 673
e-mail: raulr@ut.ee

Education

2005–2011 University of Tartu, PhD studies
2003–2005 University of Tartu, 2005, M.Sc.
1999–2003 University of Tartu, 2003, B.Sc.
1987–1999 Türi Economic Gymnasium

Professional employment

2009–present University of Tartu, Faculty of Science and
Technology, Institute of Physics, researcher.
2007–2009 University of Tartu, Faculty of Science and
Technology, Institute of Physics, extraordinary
researcher.
2006–2007 OÜ Baltronic, product manager.
2004–2006 University of Tartu, Faculty of Science and
Technology, Institute of Physics, engineer.
2002–2003 University of Tartu, Institute of Physics, laboratory
assistant.

Main research areas

Thin film technology, atomic force microscopy, photoelectron spectroscopy,
optical characterization of thin films, structural characterization of thin films.

Language skills

Estonian, mother tongue
English, good
Russian, basic

Awards

Student stipend of the Institute of Physics, University of Tartu, 2005.

ELULOOKIRJELDUS

Üldandmed

Ees- ja perekonnanimi: Raul Rammula
Sünniaeg ja koht: 16.02.1981, Võru, Eesti
Kodakondsus: Eesti
Perekonnaseis: vabaabielus
Kontakt: Füüsika Instituut, Tartu Ülikool, Riia 142, 51014, Tartu, Eesti
Telefon: +372 7 374 673
e-mail: raulr@ut.ee

Haridus

2005–2011 Tartu Ülikool, doktoriõpe
2003–2005 Tartu Ülikool, 2005, M.Sc.
1999–2003 Tartu Ülikool, 2003, B.Sc.
1987–1999 Türi Majandusgümnaasium

Teenistuskäik

2009–k.a. TÜ Loodus- ja tehnoloogiateaduskond, TÜ Füüsika Instituut, teadur.
2007–2009 TÜ, Loodus- ja tehnoloogiateaduskond, TÜ Füüsika Instituut; erakorraline teadur.
2006–2007 OÜ Baltronic, tootejuht.
2004–2006 TÜ Loodus- ja tehnoloogiateaduskond, TÜ Füüsika Instituut; insener.
2002–2003 TÜ Füüsika Instituut, laborant.

Peamised uurimisvaldkonnad

Tahkisekilede aatomkihtsadestamine, tahkisekilede aatomjõumikroskoopia, fotoelektronspektroskoopia, tahkisekilede optiline karakteriseerimine, tahkisekilede struktuur.

Keelteoskus:

eesti keel, emakeel
Inglise, keel hea
vene keel, rahuldav

Auhinnad

TÜ Füüsika Instituudi üliõpilasstipendium, 2005.

DISSERTATIONES PHYSICAE UNIVERSITATIS TARTUENSIS

1. **Andrus Ausmees.** XUV-induced electron emission and electron-phonon interaction in alkali halides. Tartu, 1991.
2. **Heiki Sõnajalg.** Shaping and recalling of light pulses by optical elements based on spectral hole burning. Tartu, 1991.
3. **Sergei Savihhin.** Ultrafast dynamics of F-centers and bound excitons from picosecond spectroscopy data. Tartu, 1991.
4. **Ergo Nõmmiste.** Leelishalogeniidide röntgenelektronemissioon kiiritamisel footonitega energiaga 70–140 eV. Tartu, 1991.
5. **Margus Rätsep.** Spectral gratings and their relaxation in some low-temperature impurity-doped glasses and crystals. Tartu, 1991.
6. **Tõnu Pullerits.** Primary energy transfer in photosynthesis. Model calculations. Tartu, 1991.
7. **Olev Saks.** Attoampri diapsoonis voolude mõõtmise füüsikalised alused. Tartu, 1991.
8. **Andres Virro.** AlGaAsSb/GaSb heterostructure injection lasers. Tartu, 1991.
9. **Hans Korge.** Investigation of negative point discharge in pure nitrogen at atmospheric pressure. Tartu, 1992.
10. **Jüri Maksimov.** Nonlinear generation of laser VUV radiation for high-resolution spectroscopy. Tartu, 1992.
11. **Mark Aizengendler.** Photostimulated transformation of aggregate defects and spectral hole burning in a neutron-irradiated sapphire. Tartu, 1992.
12. **Hele Siimon.** Atomic layer molecular beam epitaxy of A^2B^6 compounds described on the basis of kinetic equations model. Tartu, 1992.
13. **Tõnu Reinot.** The kinetics of polariton luminescence, energy transfer and relaxation in anthracene. Tartu, 1992.
14. **Toomas Rõõm.** Paramagnetic H^{2-} and F^+ centers in CaO crystals: spectra, relaxation and recombination luminescence. Tallinn, 1993.
15. **Erko Jalviste.** Laser spectroscopy of some jet-cooled organic molecules. Tartu, 1993.
16. **Alvo Aabloo.** Studies of crystalline celluloses using potential energy calculations. Tartu, 1994.
17. **Peeter Paris.** Initiation of corona pulses. Tartu, 1994.
18. **Павел Рубин.** Локальные дефектные состояния в CuO_2 плоскостях высокотемпературных сверхпроводников. Tartu, 1994.
19. **Olavi Ollikainen.** Applications of persistent spectral hole burning in ultrafast optical neural networks, time-resolved spectroscopy and holographic interferometry. Tartu, 1996.
20. **Ülo Mets.** Methodological aspects of fluorescence correlation spectroscopy. Tartu, 1996.
21. **Mikhail Danilkin.** Interaction of intrinsic and impurity defects in CaS:Eu luminophors. Tartu, 1997.

22. **Ирина Кудрявцева.** Создание и стабилизация дефектов в кристаллах KBr, KCl, RbCl при облучении ВУФ-радиацией. Тарту, 1997.
23. **Andres Osvet.** Photochromic properties of radiation-induced defects in diamond. Tartu, 1998.
24. **Jüri Örd.** Classical and quantum aspects of geodesic multiplication. Tartu, 1998.
25. **Priit Sarv.** High resolution solid-state NMR studies of zeolites. Tartu, 1998.
26. **Сергей Долгов.** Электронные возбуждения и дефектообразование в некоторых оксидах металлов. Тарту, 1998.
27. **Кауро Кукли.** Atomic layer deposition of artificially structured dielectric materials. Tartu, 1999.
28. **Ivo Heinmaa.** Nuclear resonance studies of local structure in $\text{RBa}_2\text{Cu}_3\text{O}_{6+x}$ compounds. Tartu, 1999.
29. **Aleksander Shelkan.** Hole states in CuO_2 planes of high temperature superconducting materials. Tartu, 1999.
30. **Dmitri Nevedrov.** Nonlinear effects in quantum lattices. Tartu, 1999.
31. **Rein Ruus.** Collapse of 3d (4f) orbitals in 2p (3d) excited configurations and its effect on the x-ray and electron spectra. Tartu, 1999.
32. **Valter Zazubovich.** Local relaxation in incommensurate and glassy solids studied by Spectral Hole Burning. Tartu, 1999.
33. **Indrek Reimand.** Picosecond dynamics of optical excitations in GaAs and other excitonic systems. Tartu, 2000.
34. **Vladimir Babin.** Spectroscopy of exciton states in some halide macro- and nanocrystals. Tartu, 2001.
35. **Toomas Plank.** Positive corona at combined DC and AC voltage. Tartu, 2001.
36. **Kristjan Leiger.** Pressure-induced effects in inhomogeneous spectra of doped solids. Tartu, 2002.
37. **Helle Kaasik.** Nonperturbative theory of multiphonon vibrational relaxation and nonradiative transitions. Tartu, 2002.
38. **Tõnu Laas.** Propagation of waves in curved spacetimes. Tartu, 2002.
39. **Rünno Lõhmus.** Application of novel hybrid methods in SPM studies of nanostructural materials. Tartu, 2002.
40. **Kaido Reivelt.** Optical implementation of propagation-invariant pulsed free-space wave fields. Tartu, 2003.
41. **Heiki Kasemägi.** The effect of nanoparticle additives on lithium-ion mobility in a polymer electrolyte. Tartu, 2003.
42. **Villu Repän.** Low current mode of negative corona. Tartu, 2004.
43. **Алексей Котлов.** Оксианионные диэлектрические кристаллы: зонная структура и электронные возбуждения. Тарту, 2004.
44. **Jaak Talts.** Continuous non-invasive blood pressure measurement: comparative and methodological studies of the differential servo-oscillometric method. Tartu, 2004.
45. **Margus Saal.** Studies of pre-big bang and braneworld cosmology. Tartu, 2004.

46. **Eduard Gerškevičš.** Dose to bone marrow and leukaemia risk in external beam radiotherapy of prostate cancer. Tartu, 2005.
47. **Sergey Shchemelyov.** Sum-frequency generation and multiphoton ionization in xenon under excitation by conical laser beams. Tartu, 2006.
48. **Valter Kiisk.** Optical investigation of metal-oxide thin films. Tartu, 2006.
49. **Jaan Aarik.** Atomic layer deposition of titanium, zirconium and hafnium dioxides: growth mechanisms and properties of thin films. Tartu, 2007.
50. **Astrid Rekker.** Colored-noise-controlled anomalous transport and phase transitions in complex systems. Tartu, 2007.
51. **Andres Punning.** Electromechanical characterization of ionic polymer-metal composite sensing actuators. Tartu, 2007.
52. **Indrek Jõgi.** Conduction mechanisms in thin atomic layer deposited films containing TiO₂. Tartu, 2007.
53. **Aleksei Krasnikov.** Luminescence and defects creation processes in lead tungstate crystals. Tartu, 2007.
54. **Küllike Rägo.** Superconducting properties of MgB₂ in a scenario with intra- and interband pairing channels. Tartu, 2008.
55. **Els Heinsalu.** Normal and anomalously slow diffusion under external fields. Tartu, 2008.
56. **Kuno Kooser.** Soft x-ray induced radiative and nonradiative core-hole decay processes in thin films and solids. Tartu, 2008.
57. **Vadim Boltrushko.** Theory of vibronic transitions with strong nonlinear vibronic interaction in solids. Tartu, 2008.
58. **Andi Hektor.** Neutrino Physics beyond the Standard Model. Tartu, 2008.
59. **Raavo Josepson.** Photoinduced field-assisted electron emission into gases. Tartu, 2008.
60. **Martti Pärs.** Study of spontaneous and photoinduced processes in molecular solids using high-resolution optical spectroscopy. Tartu, 2008.
61. **Kristjan Kannike.** Implications of neutrino masses. Tartu, 2008.
62. **Vigen Issahhanjan.** Hole and interstitial centres in radiation-resistant MgO single crystals. Tartu, 2008.
63. **Veera Krasnenko.** Computational modeling of fluorescent proteins. Tartu, 2008.
64. **Mait Müntel.** Detection of doubly charged higgs boson in the CMS detector. Tartu, 2008.
65. **Kalle Kepler.** Optimisation of patient doses and image quality in diagnostic radiology. Tartu, 2009.
66. **Jüri Raud.** Study of negative glow and positive column regions of capillary HF discharge. Tartu, 2009.
67. **Sven Lange.** Spectroscopic and phase-stabilisation properties of pure and rare-earth ions activated ZrO₂ and HfO₂. Tartu, 2010.
68. **Aarne Kasikov.** Optical characterization of inhomogeneous thin films. Tartu, 2010.

69. **Heli Valtna-Lukner.** Superluminally propagating localized optical pulses. Tartu, 2010.
70. **Artjom Vargunin.** Stochastic and deterministic features of ordering in the systems with a phase transition. Tartu, 2010.
71. **Hannes Liivat.** Probing new physics in e^+e^- annihilations into heavy particles via spin orientation effects. Tartu, 2010.
72. **Tanel Mullari.** On the second order relativistic deviation equation and its applications. Tartu, 2010.
73. **Aleksandr Lissovski.** Pulsed high-pressure discharge in argon: spectroscopic diagnostics, modeling and development. Tartu, 2010.
74. **Aile Tamm.** Atomic layer deposition of high-permittivity insulators from cyclopentadienyl-based precursors. Tartu, 2010.
75. **Janek Uin.** Electrical separation for generating standard aerosols in a wide particle size range. Tartu, 2011.
76. **Svetlana Ganina.** Hajusandmetega ülesanded kui üks võimalus füüsika-õppe efektiivsuse tõstmiseks. Tartu, 2011
77. **Joel Kuusk.** Measurement of top-of-canopy spectral reflectance of forests for developing vegetation radiative transfer models. Tartu, 2011.